Chemical Hydrogen Storage using Ultra-High Surface Area Main Group Materials & The Development of Efficient Amine-Borane Regeneration Cycles

Final Report

Susan M. Kauzlarich, Phillip P. Power, Doinita Neiner, Alex Pickering, Eric Rivard, Bobby Ellis, T. M. Atkins, A. Merrill, R. Wolf and Julia Wang

09/05/2010

Prepared for
Department of Energy
Office of Energy Efficiency and Renewable Energy
Hydrogen Program, Hydrogen Storage
Under Contract DE-FC36-05GO15055
DOE Technology Development Manager: Grace Ordaz
DOE Project Officer: Jim Alkire

TABLE OF CONTENTS

Overview

Project Objectives

Phase 1

- To identify light element nanomaterials and molecular compounds as storage materials enabling DOE targets
- To design and test simple routes to such materials and compounds using mild conditions
- Optimize the synthesis and hydrogen capacity of these materials, while providing detailed physical characterization.
- Demonstrate the viability of the synthesized materials for commercial application by studying their weight and volume as well as the reversibility of hydrogen uptake.
- The synthesis and testing of molecular derivatives of the lighter main group elements, e.g. boron, aluminum, silicon or phosphorus, for reversible reactivity with hydrogen.

Phase 2

Regeneration

- Provide new materials, compounds and support for chemical regeneration of amine-boranes or boron amides from B-X (X= halide or oxide) compounds.
- To develop a method of regenerating amine-boranes or other chemical hydrides from spent fuel with use of a metal formate/hydride cyclable system.

- To develop light element hydride nanomaterials
    - Test light element hydride nanomaterials ability to transfer hydrogen using different spent fuel forms.
    - Test light element hydride nanomaterials for spent chemical hydride regeneration such as “AB” regeneration.

Release

- Enhancement of hydrogen release for chemical hydrides such as ammonia-borane “AB” with light element hydride nanoparticles (NPs).
    - Produce light element hydride NPs in a low cost, high yield method.

- The synthesis and testing of molecular derivatives of the lighter main group elements, e.g. boron, aluminum, silicon or phosphorus, for reversible reactivity with hydrogen. The initial focus of our work was on boron-phosphorus molecular species.

1. The Fabrication of Light Element Nanoparticles and Their Use as Hydrogen Storage Materials

Objectives

- To identify light element nanomaterials and molecular compounds as storage materials enabling DOE targets
- To design and test simple routes to such materials and compounds using mild conditions
- Optimize the synthesis and hydrogen capacity of these materials, while providing detailed physical characterization.
- Demonstrate the viability of the synthesized materials for commercial application by studying their weight and volume as well as the reversibility of hydrogen uptake.
- The synthesis and testing of molecular derivatives of the lighter main group elements, e.g. boron, aluminum, silicon or phosphorus, for reversible reactivity with hydrogen. The initial focus of our work was on boron-phosphorus molecular species.

Accomplishments

- Low temperature synthetic route to amine terminated silicon nanoparticles. Preliminary measurements indicate generation of ammonia via thermolysis.
- Low temperature solution synthetic route to boron nanoparticles. Preliminary synthetic demonstration of hydrogen on the surface.
- Low temperature solution synthetic route for macroscopic amounts of silicon nanoparticles with hydrogen terminated surface. Preliminary measurements indicate H_2 generation via hydrolysis and thermolysis
- Explore lighter Si alloy nanoparticles with hydrogen on the surface, Si_xE_{1-x})-H, where E = B, C.

Introduction and Background

The focus of the project was to design and synthesize light element compounds and nanomaterials that will reversibly store molecular hydrogen for hydrogen storage materials. The primary targets investigated during the last year were amine and hydrogen terminated silicon (Si) nanoparticles, Si alloyed with lighter elements (carbon (C) and boron (B)) and boron nanoparticles. The large surface area of nanoparticles should facilitate a favorable weight to volume ratio, while the low molecular weight elements such as B, nitrogen (N), and Si exist in a variety of inexpensive and readily available precursors. Furthermore, small NPs of Si are non-toxic and non-corrosive. Insights gained from these studies will be applied toward the design and synthesis of hydrogen storage materials that meet the DOE 2010 hydrogen storage targets: cost, hydrogen capacity and reversibility.

Approach

Two primary routes were explored for the production of nanoparticles smaller than 10 nm in diameter. The first was the reduction of the elemental halides to achieve nanomaterials with chloride surface termination that could subsequently be replaced with amine or hydrogen. The second was the reaction of alkali metal Si or Si alloys with ammonium halides to produce hydrogen capped nanomaterials. These materials were characterized via X-ray powder diffraction, TEM, FTIR, TG/DSC, and NMR spectroscopy.

I. Light Element Nanoparticles

I.1. Amine Terminated Silicon Nanoparticles

The room temperature solution synthesis for producing Si nanoparticles (NPs) (previously developed in the Kauzlarich group) has been applied to the synthesis of amine terminated Si NPs. The following synthetic route is successful in producing Si NPs below 10 nm:

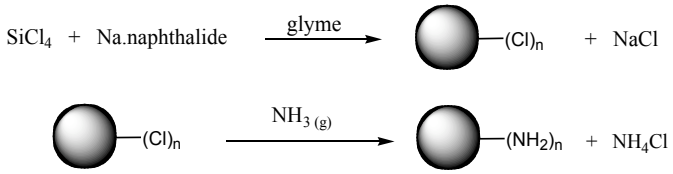

Figure 1 shows the X-ray diffraction of the Si NPs prepared as described above compared with a crystalline Si standard. Characterization by powder X-ray diffraction (XRD) shows the material to be amorphous. The ^{29}Si NMR data for the amine terminated silicon nanoparticles is presented in Figure 2. Spectroscopic analysis by solid-state ^{29}Si NMR indicates the nano-structure of the material and compares well with ^{29}Si NMR published by this group. Transmission electron microscopy shows that the Si NPs are 3-4 nm in size (Figure 3). Figure 4 presents the FTIR data for the as prepared particles as well as after exposure to air for 2 weeks. Infrared analysis indicates the existence of Si-N and N-H interactions that are assumed to be located on the surface. Infrared analysis of the material also displays hydrolytic decomposition of the Si-(NH_2) interactions to form Si-O(H) bonds upon exposure to air. The gas that results from the hydrolysis and the remaining solid from the reaction was not characterized. Hydrolysis begins after approximately 12 hours but does not completely decompose after two weeks. This indicates that the material is slightly air sensitive and should be handled under inert conditions, but the material is not so air sensitive as to exclude it from applications. This material also had significant weight loss at temperatures above 100˚C. However, when the resulting gas was qualitatively analyzed with a pH indicator, the gaseous product was found to be basic and is presumed to be ammonia.

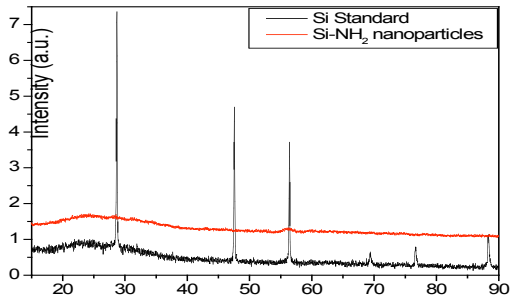

Figure 1. X-ray powder patterns for the amine terminated nanoparticles (red) and for crystalline silicon standard (black).

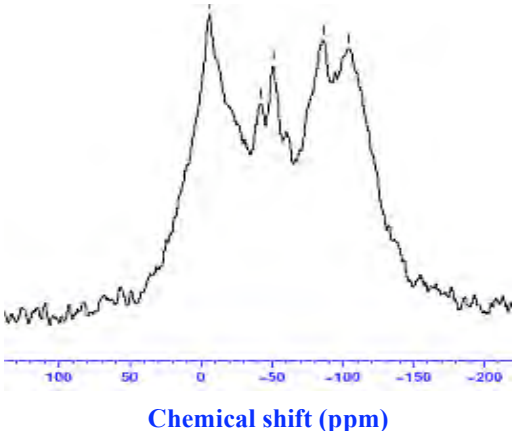

Figure 2. ^{29}Si NMR spectrum for the amine terminated nanoparticles.

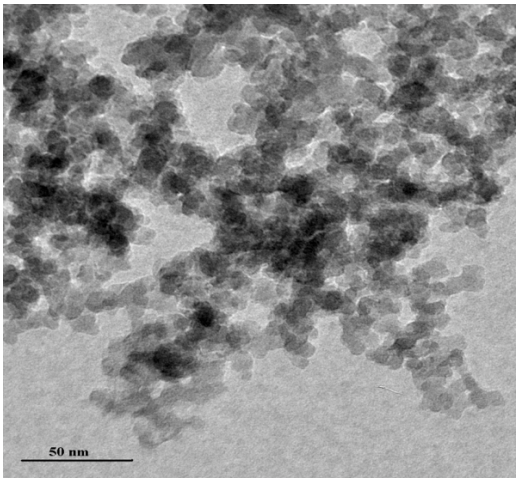

Figure 3. TEM image of the amine terminated Si NPs.

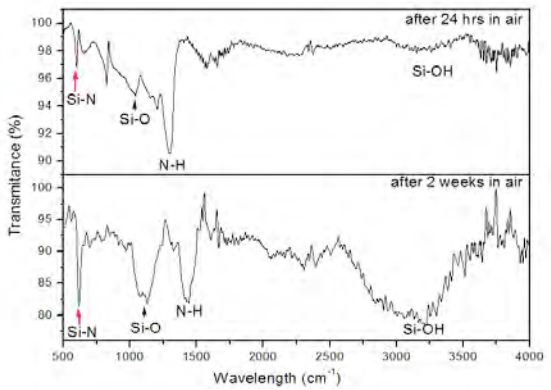

Figure 4. FTIR data for the amine terminated Si NPs as prepared, and exposed to air for 2 weeks. The FTIR data has been collected under nitrogen. The samples have been exposed to air during sample preparation for FTIR.

I.2. Hydrogen Terminated Silicon and Silicon Alloy Nanoparticles

Silicon and silicon alloyed NPs were prepared by reacting sodium silicide with ammonium bromide either a solid state synthesis or in solution synthesis via:

$$NaSi + NH_4Br \rightarrow Si–H\ nanoparticles + NaBr + NH_3 \quad (1)$$

Sodium silicide (NaSi) has been prepared according to literature methods. For the C and B doped alloyed NPs, $NaSi_{1-x}E_x$ was prepared via the reactions shown below:

$$NaH + (1-x)Si + C \rightarrow NaSi_{1-x}C_x \text{ and } NaH + (1-x)Si + B \rightarrow NaSi_{1-x}B_x \quad (2)$$

The synthesis of these NPs as well as the hydrogen storage ability of the obtained materials has led to three publications. Briefly, the synthesis of silicon and silicon alloyed NPs has been achieved via reactions (1) and (2). Ammonium bromide (NH_4Br) and sodium bromide (NaBr) have been dried under dynamic vacuum at 100 ºC for 2 days. The larger size NPs, 60 nm, have been prepared via a solid-state reaction between NaSi and NH_4Br. The smaller size NPs, 10 nm, were obtained through a solid-state reaction of NaSi and NH_4Br with the addition of NaBr as a diluting agent. The reactants have been intimately mixed in an agate mortar (or ball milled) and pressed into pellets. The reaction takes place in 17 hours under dynamic vacuum conditions at 200ºC. It is important that the temperature does not exceed 250ºC due to the formation of a mixture of Si NPs and sodium silicon clathrate phase under these conditions. It is worth noting that this solid state reaction can also be run under the following conditions: from 200ºC to 300ºC (not ramped but preheated furnace) under no flow conditions (it is protected from air by the positive pressure of ammonia – checked with pH paper). The reaction is considered complete when ammonia gas evolution ceases. Under these conditions, amorphous Si is formed. The formation of amorphous Si presumably results from having an ammonia gas pressure above the reaction mixture. The production of amorphous Si under similar conditions has been also observed in the solution particle synthesis under no flow conditions. In order to reduce the particle size, the reaction between NaSi and NH_4Br has also been performed via a solution route. The Si NPs were prepared by a solution reaction according to reaction (1) in dioctyl ether (DOE), dimethoxyethane (DME) and dimethylformamide (DMF). NaSi was stirred and heated at 80ºC overnight in 200 ml solvent and the mixture, solvent and NaSi was canulated over NH_4Br under flowing argon. The reaction can also be performed under no flow conditions case in which there will be an ammonia pressure over the solution, which leads to the formation of amorphous Si NPs regardless of the nature of the solvent or temperature of the reaction. The reaction was considered complete when NH_3 gas stopped coming off as indicated by pH paper. The reaction was also performed in DOE and DME by purging dry NH_3 gas through the reaction vessel for 5 minutes, at room temperature with stirring. It was believed that ammonia increased the solubility of NH_4Br and NaSi in solution. Following the purge, the mixture of NaSi, NH_4Br and solvent were brought to reflux. Upon completion of the reaction, the powder was washed under argon by canulating degassed acidified water (HF ~ 2%) over it to remove the salt byproduct, NaBr. The reaction products were separated from the reaction mixture by either vacuum filtration or solvent evaporation. The Si NPs were separated from the salt by washing with HPLC water and an HF/EtOH mixture. Then Si and Si alloy NPs were dried under dynamic vacuum at 150 ºC overnight. Infrared data indicated the presence of solvent presumably due to binding of the solvent to the surface of these NPs.

Caution has to be taken when washing all of the alkali metal silicide reaction products with water. Traces of alkali metal silicides are very exothermic when reacted with water. They

generate sufficient heat to ignite the hydrogen byproduct of the reaction. This can result in an explosion and fire. It is recommended that water addition should be performed slowly under an inert atmosphere.

Figure 5 presents the XRD data for the Si NPs prepare via reaction (1) in DOE, DME either under a flow of nitrogen or under pressure of ammonia and after high temperature heating up to 1000 ˚C. Figure 6 presents a summary of for reaction (1) products obtained in DMF.

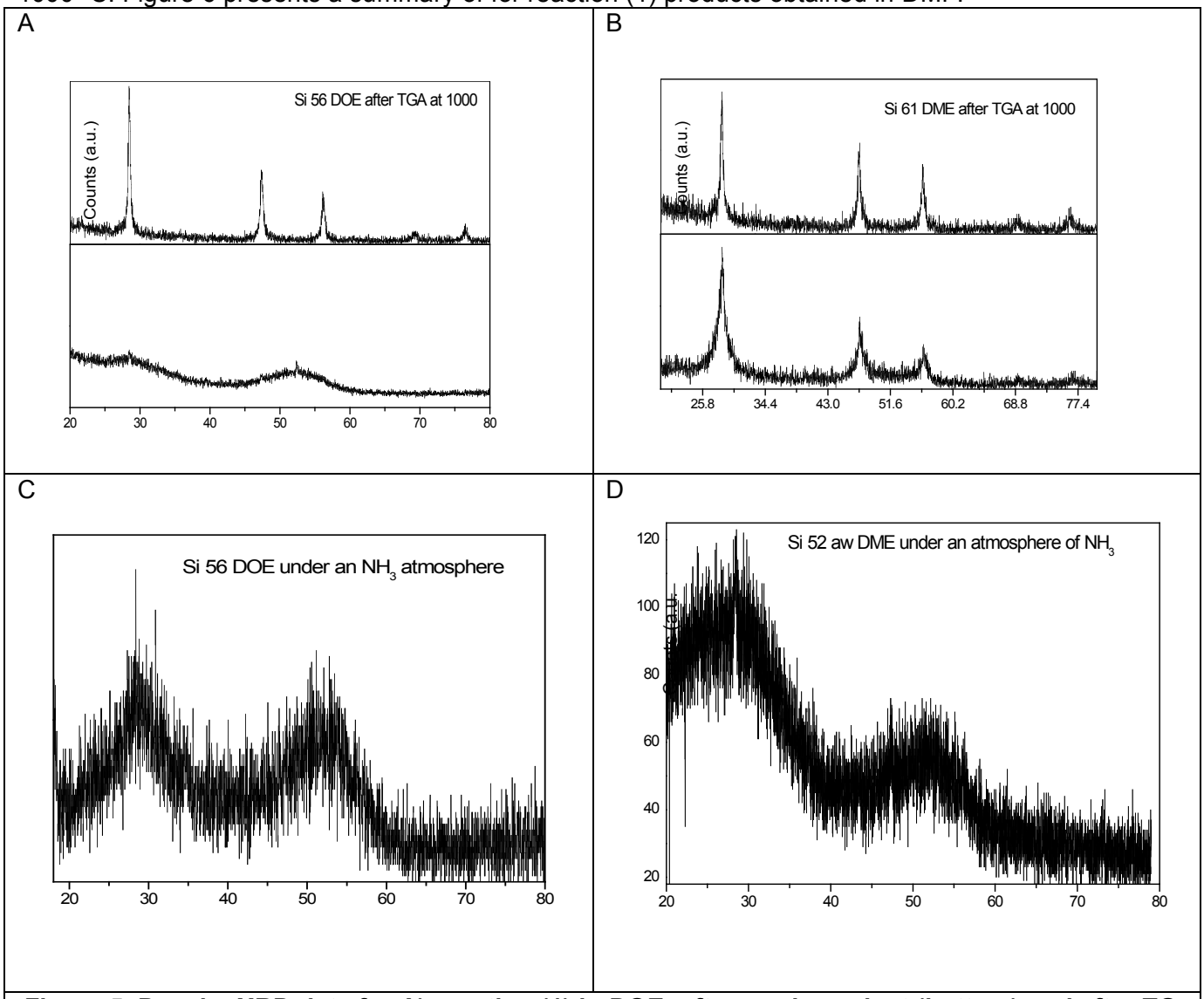

Figure 5. Powder XRD data for A) reaction (1) in DOE; after wash product (bottom) and after TG at 1000 ºC in Ar (top), B) reaction (1) in DME; after wash product (bottom)and after TG at 1000 ºC in Ar (top), C) Si NPs obtained under an ammonia atmosphere by reaction (1) in DOE and D) Si NPs obtained under an ammonia atmosphere by reaction (1) in DME.

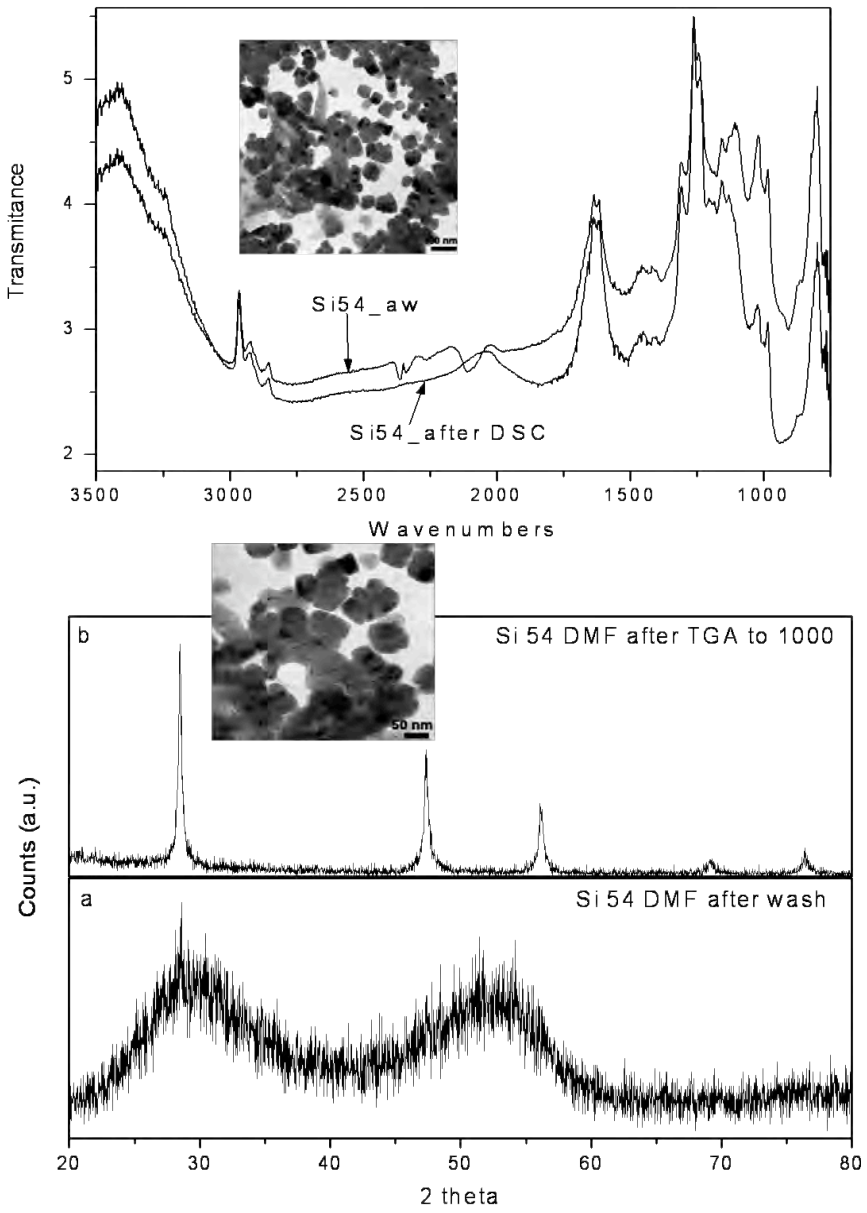

Figure 6. FTIR, XRD, and TEM data for the Si NPs obtained in DMF.

It was found that the reaction conditions, such as temperature, time and composition are important for controlling the size of hydrogen terminated Si NPs. The resulting dark colored Si NP powder obtained in high yield varied from crystalline to amorphous, along with mixtures of both. The nanomaterials selected for further hydrogen storage characterization are presented in Table 1. Powder XRD data of these NPs are presented in Figure 7 a - d. The SEM/TEM data are shown in Figure 8 a-d.

Figure 7a indicated that the particle size (based on the FWHM of the 28.7˚ 2θ peak) is 60 nm. The SEM image, Figure 8a, is consistent with the data from XRD and the particles are spherical. From Figure 1b, the powder XRD data for the sample showed that this material is a mixture of amorphous and crystalline silicon. The amorphous Si peaks are broad and can be seen at 28˚ and 49˚ 2θ, and the crystalline Si diffraction peaks are at 28.7˚, 47.5˚, 56.5˚, 69.3˚ and 76.6˚ corresponding to [111], [220], [311], [400], and [331] Miller indices. No attempts to calculate the

particle size from X-ray data were made in this case. The average diameter of the particles, based on the TEM data, was 11 nm. The powder X-ray patterns and the TEM images for the solution reactions are presented in Figure 7 c and d. The X-ray powder pattern data show that the sample prepared in DME is a mixture of amorphous and crystalline silicon, and the sample prepared in DOE is amorphous. The average particle size of these NPs was measured from TEM data and found to be 8 and 4 nm, respectively.

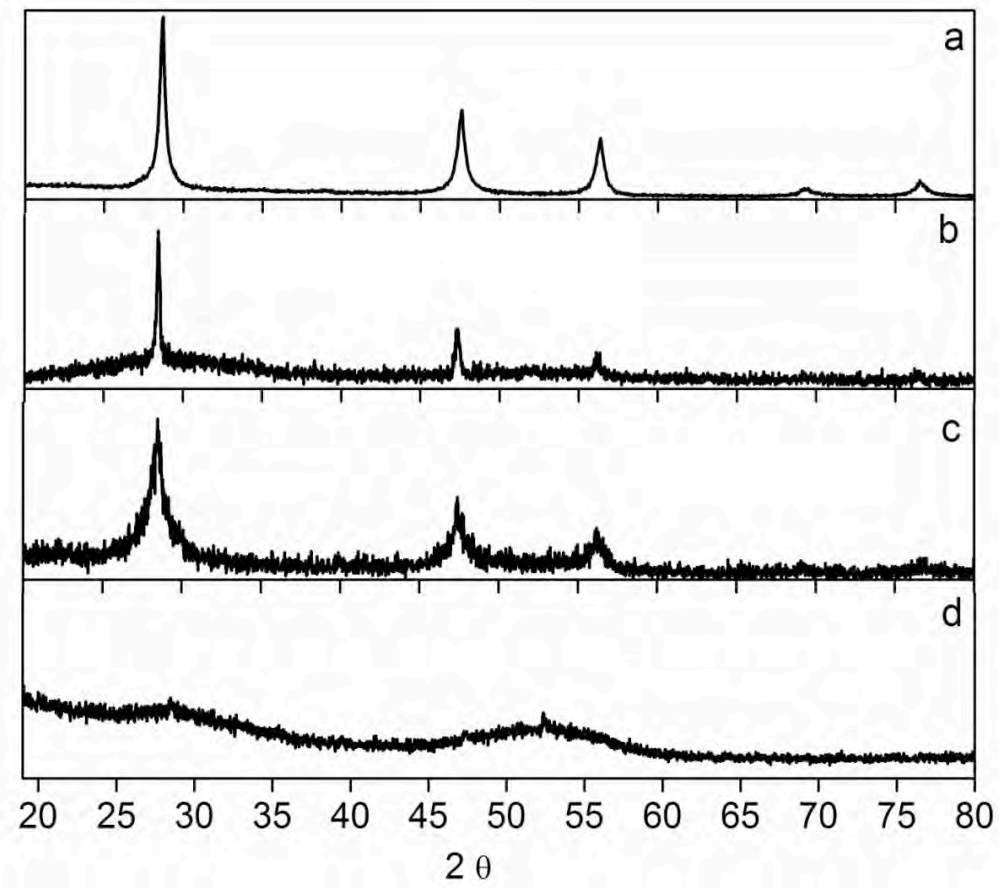

Figure 7. XRD data for the Si NP prepared via reaction (1); a) solid state, b) solid state using NaBr as a dilutant, c) in DME, d) in DOE.

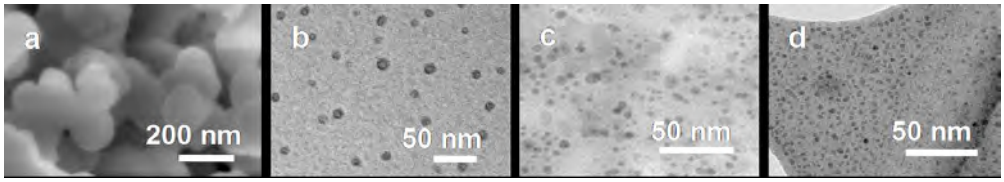

Figure 8. SEM/TEM pictures for the Si NP prepared via reaction (1); a) solid state, b) solid state using NaBr as a diluant, c) in DME, d) in DOE.

The surface of the Si NPs were characterized by both solid state MAS NMR and FTIR. The ^{1}H MAS NMR spectra before and after washing the NPs are presented in Figure 9 A-C for the 60, 11 and 5 nm NPs. Based on the ^{1}H MAS NMR data there are multiple hydrogen sites on the surface of these particles and that some physisorbed species are initially present in the sample,

but disappear upon washing. The sharp resonance is consistent with the presence of mobile hydrogen on the surface. It is possible that when NH_4Br reacts with NaSi, H_2 is produced and is present as a physisorbed species in the final product mixture. From the integrated intensity of the sharp resonance, this represents 22% of the total amount of hydrogen. When the mixture (Si-H NPs and NaBr) is washed with water, the physisorbed hydrogen is removed and the spectrum is consistent with chemically bonded Si–H_x species.

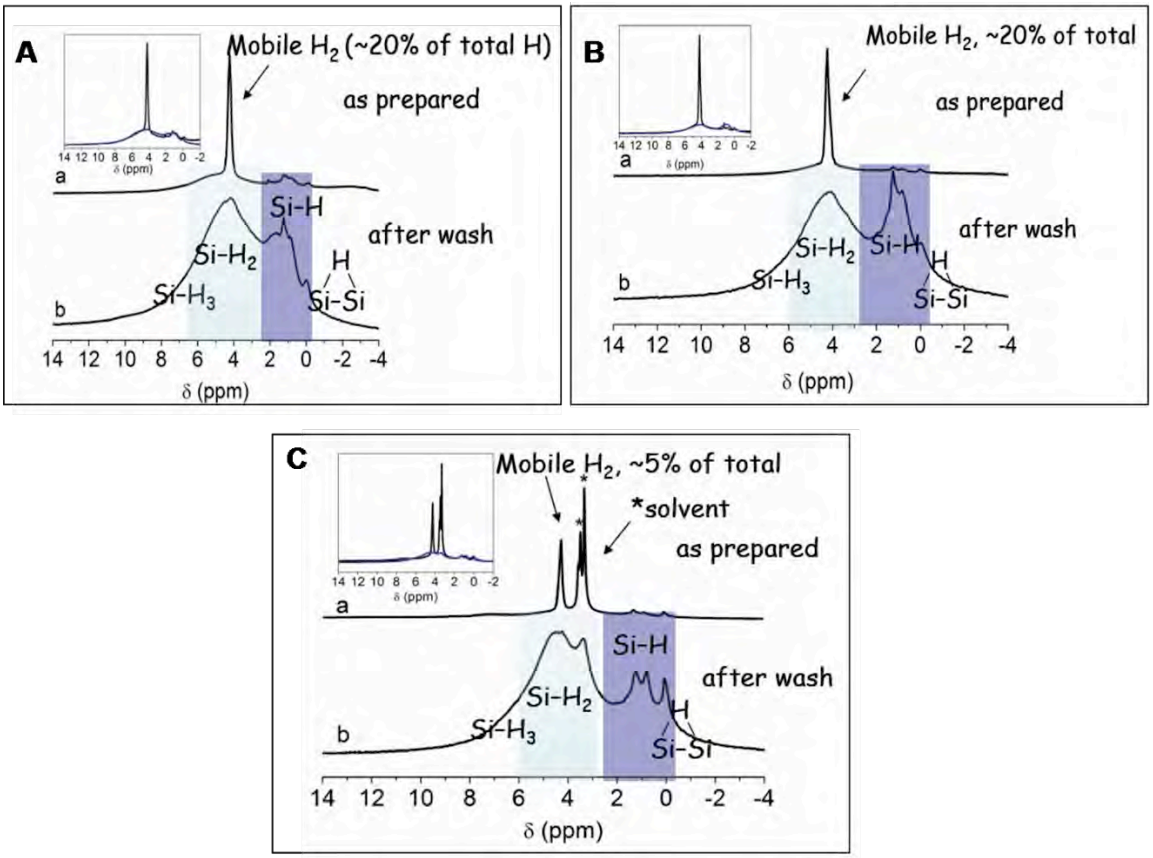

Figure 9. ^{1}H solid state NMR data for Si-H NPs before and after wash; A) 60 nm, B) 11 nm, C) 5 nm.

^{29}Si CP MAS NMR spectroscopy was performed on the same samples and the data were collected for the as-prepared after the washed sample and are presented in Figure 10 A-C. The as-prepared sample had a spectrum that revealed the presence of a broad signal centered about -75 ppm. After washing with acidified water three signals -45, -84 and -101 ppm (assigned by fitting the experimental data with Lorentzian profile functions) can be seen in the ^{29}Si CP MAS NMR. The profile fits are presented in the inset of Figure 10. The peak at -45 ppm corresponds to diluted monohydritic SiH species. The peak at -84 ppm could be attributed to SiH_2 species. The peak at -101 ppm can be assigned to the monohydride SiH cluster. The peak at -101 ppm could also be assigned to a mixture of the OSi-H and SiH groups, as the resonance is in the range assigned to Si-O bonds in amorphous SiO_2. In addition to these peaks, the sample prepared in DME also shows the Si-OR groups of the solvent, which are confirmed by FTIR spectroscopy. The solvent contributes to Si-OR bonds on the surface of these particles and protects the surface from oxidation during washing.

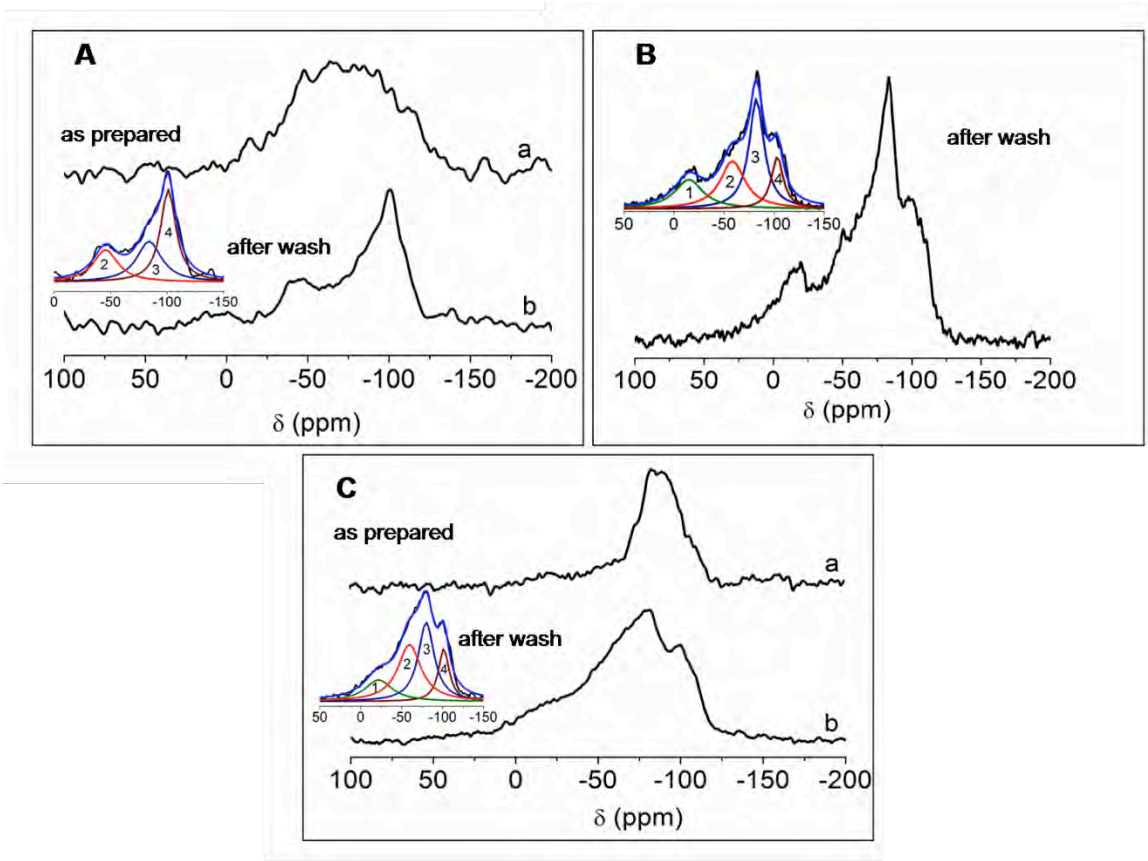

Figure 10. ^{29}Si CP NMR data for Si-H NPs before and after wash; A) 60 nm, B) 11 nm, C) 5 nm. The insets represent the Lorentzian profile function fits to the experimental data.

The FTIR spectra for the Si NPs are presented in Figure 11 a-d. FTIR data confirm the presence of hydrogen on the surface of these particles. The FTIR data are consistent with all the NPs containing Si-H and SiH_2 groups on the surface. All of the FTIR spectra for the prepared NPs show the 900 cm^{-1} and 1900-2100 cm^{-1} region, characteristic for the SiH_2 scissor mode in the fingerprint region, and for the Si-H and SiH_2 stretches in the 2000 cm^{-1} region. These signals can be attributed to Si-H, SiH_2, or SiH_x species present on the surface of the silicon NPs. In the fingerprint region, 600-700 cm^{-1}, Si lattice vibrations are present. In the case of the larger NPs obtained via the solid-state reactions, the 60 and 11 nm diameter particles, the Si-O-Si stretch is present at 1100 cm^{-1}. The Si-O-Si stretch can be removed with HF. The NPs prepared via the solvent systems do not show the same sensitivity to oxygen, presumably because they are protected from further oxidation through Si-OR linkages also seen in the ^{1}H and ^{29}Si CP MAS NMR data. Furthermore, FTIR analyses of the solvent-prepared NPs show the presence of the solvent presumably on the surface of these nanoparticles. As see in Figures 11 c and 11 d, alkyl C-H stretch modes (aliphatic v(C-H) stretching modes at 2800-2900 cm^{-1}), deformation modes at 1300-1400 cm^{-1}, and C-C stretching modes for alkyl chains at 1500-1600 cm^{-1} are also observed.

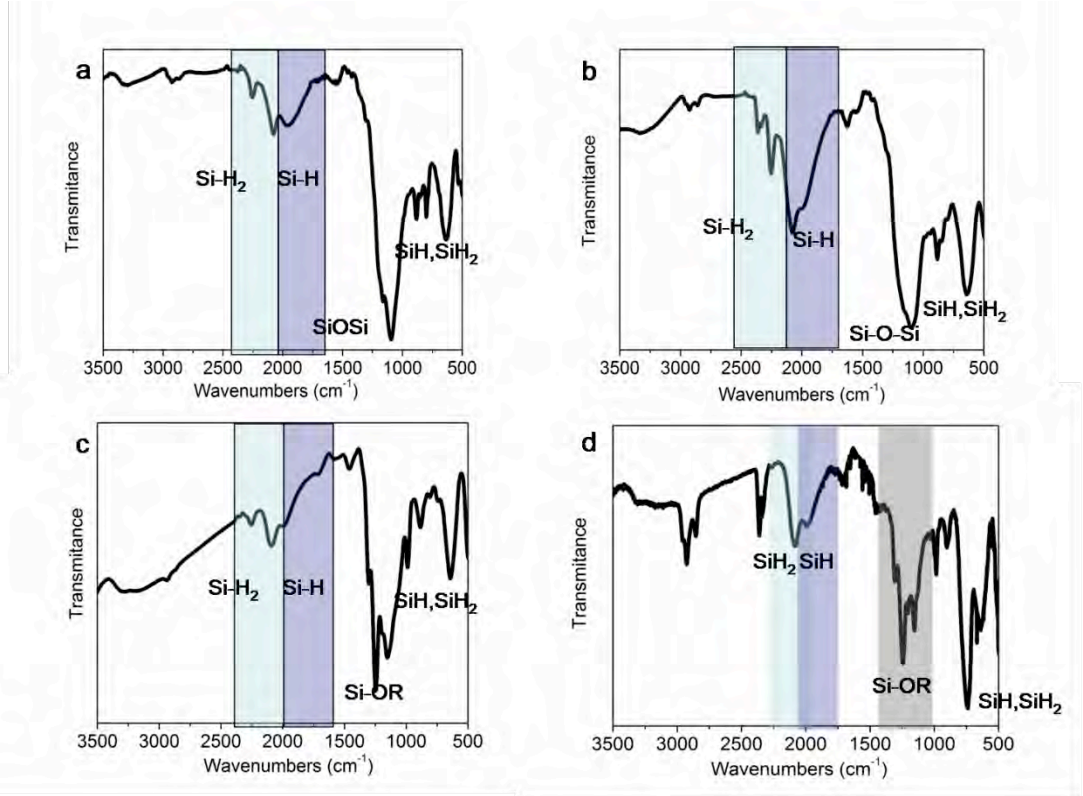

Figure 11. FTIR data for Si-H NPs after wash; a) 60 nm, b) 11 nm, c) 5 nm and d) 4 nm.

TG/MS under flowing argon data is presented in Figure 12, 13 and 14 for the 11 nm, 5 nm and 4 nm diameter particles, respectively. The thermogravimetric (TG) data show an initial weight loss with a rise in the hydrogen MS signal, which supports hydrogen evolution upon heating. The data support our initial hypothesis in that the smaller particles show the greater weight loss. However, the particles made via the solid state method are oxidized, presumably from washing with water, while the particles prepared in solvent have solvent molecules binding to their surface. The particles prepared via the solid state route evolve 3% hydrogen. The weight loss for the 4-nm particles starts at ~300°C with a plateau at ~450°C, with all weight loss completed at 600°C. The weight loss for the 5-nm particles is continuous; it starts at 300°C and finishes at 600°C. The DSC data show two exotherms that are associated with the two weight losses. The first exotherm is observed at ~350°C for both the 5-nm-diameter particles (DME) and ~410°C for the 4-nm NPs prepared in DOE. These exotherms are consistent with previous data showing hydrogen removal from the surface. The second exotherm is observed at 560°C for both the 5-nm and the 4-nm NPs. This exotherm may be attributed to hydrocarbon loss from solvent molecules adsorbed to the surface. There is an additional exotherm observed above 600°C for the 4-nm-diameter NPs, which is consistent with the amorphous-to-crystalline Si phase transition. The TG/MS data for the volatiles (other than hydrogen) evolved from the Si NPs prepared in solvent are presented in Figure 15 and 16. Figure 15 presents the volatiles desorbed by the 4-nm NPs prepared in DOE. The data indicate that above 200°C, masses 18 (H_2O), 44 (CO_2), 15 and 31 (hydrocarbons or silanes) are evolved from the sample. However, the volatiles are three orders of magnitude lower than the hydrogen signal from the MS (necessitating a separate figure to demonstrate their presence). Also, most of these volatiles are desorbed above 350°C. Figure 16 presents the volatiles evolved by the 5-nm NPs prepared in DME. These data show that most of the hydrocarbon and carbon dioxide are evolved above 400°C.

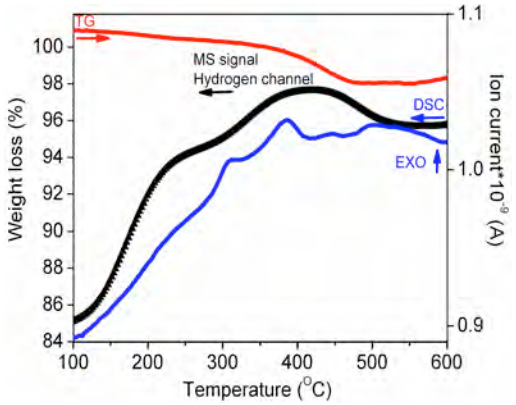

Figure 12. TGA/DSC/MS (hydrogen channel) data for the SiH NPs prepared via solid state (11 nm).

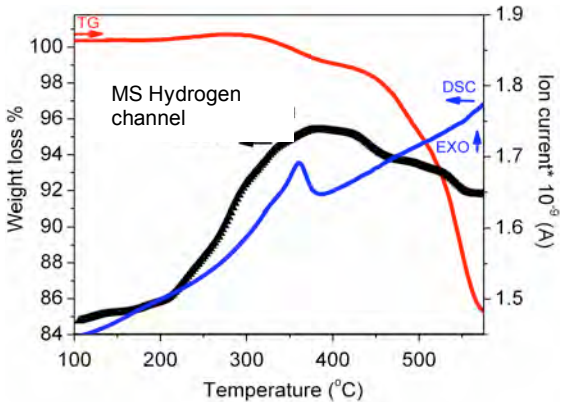

Figure 13. TGA/DSC/MS (hydrogen channel) data for the SiH NPs prepared in DME (5 nm).

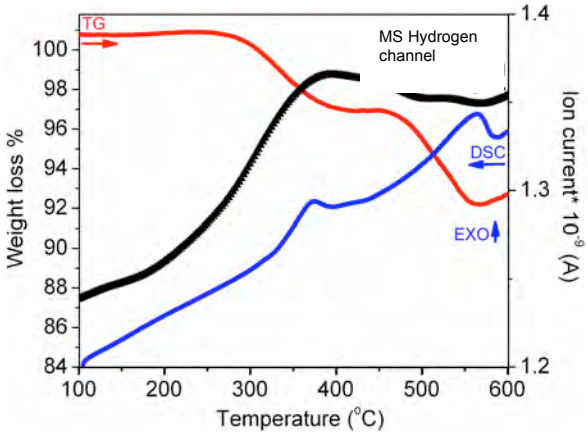

Figure 14. TGA/DSC/MS (hydrogen channel) data for the SiH NPs prepared in DME (5 nm).

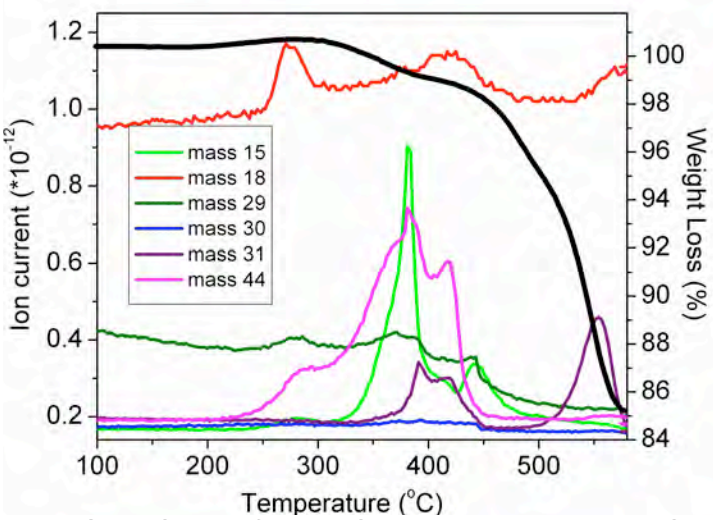

Figure 15. TGA/MS data for the SiH NPs prepared in DOE (4 nm)

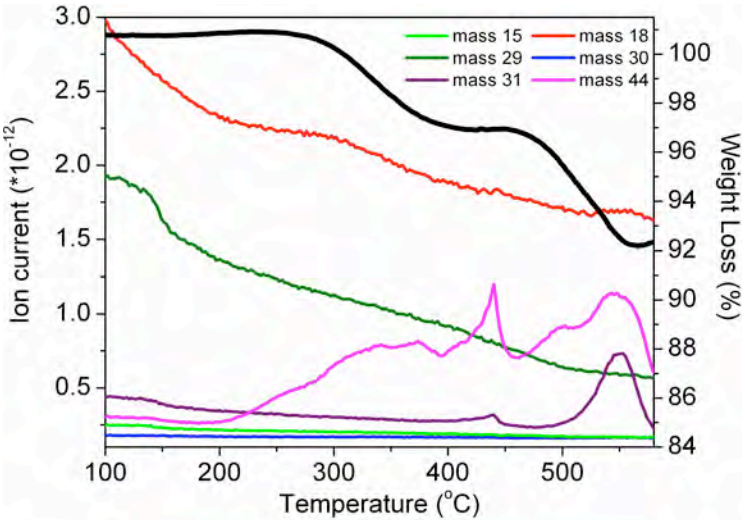

Figure 16. /MS data for the SiH NPs prepared in DME (5 nm)

In order to identify the weight loss associated with hydrogen evolution from the total weight losses observed, the 4 nm SiH NPs were heated to 350°C and held there for 100 minutes. In addition, an FTIR spectrum before and after heating was performed. These data are presented in Figures 17 and 18. From the TGA and FTIR data we can propose that ~ 4.5% hydrogen is evolved from the 4 nm nanoparticles. The FTIR before heating shows the Si-H stretch and the FTIR after heating shows the absence of a Si-H stretch. Our efforts to regenerate the SiH chemically using 2% HF were unsuccessful: upon SiH restoration from HF a Si-H stretch is observed again in the FTIR spectrum; however, upon heating the same amount of hydrogen loss is not seen. This may be due to the fact that once heated at 350°C, the Si NPs are probably sintered and the reduced surface area does not hold as much hydrogen. In addition, a rehydrogenation experiment under a hydrogen pressure of 50 bar was conducted in a PCT instrument (HyEnergy-Setaram). No hydrogen uptake has been observed at room temperature or at 300°C. Most of the results presented above regarding the use of Si NPs as a potential hydrogen storage material have been published in Chemistry of Materials, 2010.

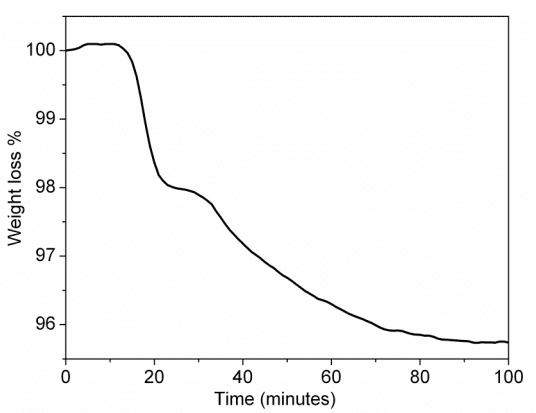

Figure 17. TGA data isothermal at 350°C for the 4 nm Si NPs.

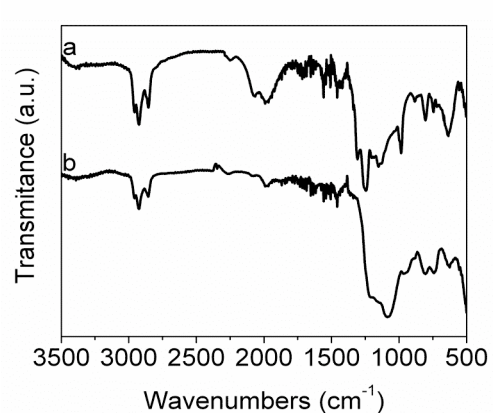

Figure 18. FTIR data for the 4 nm SiH NPs; a) before isothermal heating at 350°C and b) after heating at 350°C for 100 minutes.

Other synthetic conditions have also been investigated, these included changing the ratio of NaSi:NH_4Br. In the reaction of NaSi with NH_4Br (1:1 molar ratio), it was observed that ~20% of the NaSi (from ^{23}Na NMR) was consistently unreacted. Therefore a 1:2 and 1:3 molar ratio was used in order to optimize the reaction conditions for the B and C doped NaSi systems. It was found that increasing the amount of NH_4Br had a beneficial effect on the coverage of silicon nanoparticles with hydrogen, and reduced the oxidation of the silicon nanoparticles. It is known that if a silicon surface is covered by hydrogen via Si-H_x bonds, these particles will be hydrophobic and will not react with water. It is believed that water (our reaction involves removal of the NaBr byproduct with water) attacks the dangling bonds and not Si-H_x or Si-OH, or Si-O-Si bonds. Figure 19 presents the XRD/FTIR data for the 1:2 and 1:3 molar ratio NaSi:NH_4Br. It also can be noted based on the XRD data presented that the Si NPs become more amorphous with increasing the amount of NH_4Br. This is presumably due to the fact that more NH_3 is released from a 1:3 as compared to a 1:3 NaSi:NH_4Br reaction mixture and this result is consistent with our previous observations under NH_3 (i.e. that amorphous Si is observed).

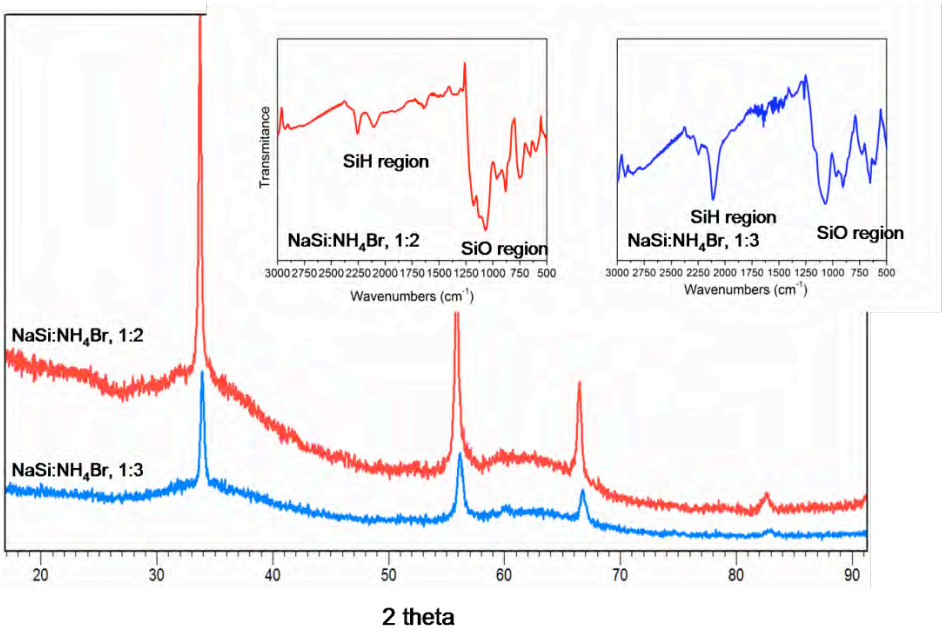

Figure 19. XRD/FTIR data for Si NPs prepared from 1:2 and 1:3 molar ratios of NaSi:NH_4Br.

The reaction with the molar ratio 1:3, NaSi:NH_4Br was performed in DME. An XRD pattern of the product of reaction before washing with water is presented in Figure 20. As one can see from Figure 20, beside the NaBr product, there is unreacted NH_4Br. NH_4Br can be removed under dynamic vacuum or argon flow with high temperatures. It is known that NH_4Br sublimes at temperatures above 220°C. As can be seen from Figure 21 after heating under argon for 12 hrs at 220 °C, there is an absence of NH_4Br in the product. Also, the Si-H bonds break due to prolonged exposure of the sample to elevated temperatures, 220 °C for 12 hrs. The sample was heated under the TG/DSC (Ar) to 600 °C (Figure 22). After heating under argon to 600 °C, and exposing the sample to air, both XRD and FTIR show the presence of water: the product observed in powder XRD is NaBr•2 H_2O and OH stretches in the FTIR at 1500 and 3300 cm^{-1}. After washing the salt byproduct out of reaction (1), the XRD corresponds to Si NP of ~ 8 nm in size. In order to monitor NH_4Br and the Si-H stretch disappearance, the sample was heated for various amounts of time under flowing Ar and dynamic vacuum and the results monitored by FTIR/XRD. The results are presented in Figure 23. After heating for 1 hr and 45 minutes under argon, NH_4Br is still present in the sample as indicated by both the FTIR and the XRD data in Figure 23 (top). After heating for 1 hr and 45 minutes under argon and 2 hrs under dynamic vacuum, neither NH_4Br and SiH are observed in the FTIR. After heating for 1 hr and 45 minutes under argon NH_4Br is still present in the sample as emphasized by both the FTIR and the XRD data in Figure 23 (top). The time and conditions of heating have been optimized to 1 hr and 45 minutes under argon and 1 hr and 15 minutes under dynamic vacuum at 220 °C.

Another systematic study was to increase the reaction (1) temperature to 300 °C and maintain a 1:1 molar ratio of reactants. Also, as mentioned above, the reaction can be performed without the use of dynamic vacuum or argon flow. Figures 24 and 25 present the XRD and FTIR data for reaction (1) under static vacuum, ambient or vacuum conditions by using the fact that reaction (1) releases gaseous products: hydrogen and ammonia and a bubbler plugged with a pH paper to indicate the cessation of ammonia evolution. The cessation of ammonia evolution, as indicated by the color change of the pH paper, was interpreted to be the end of reaction.

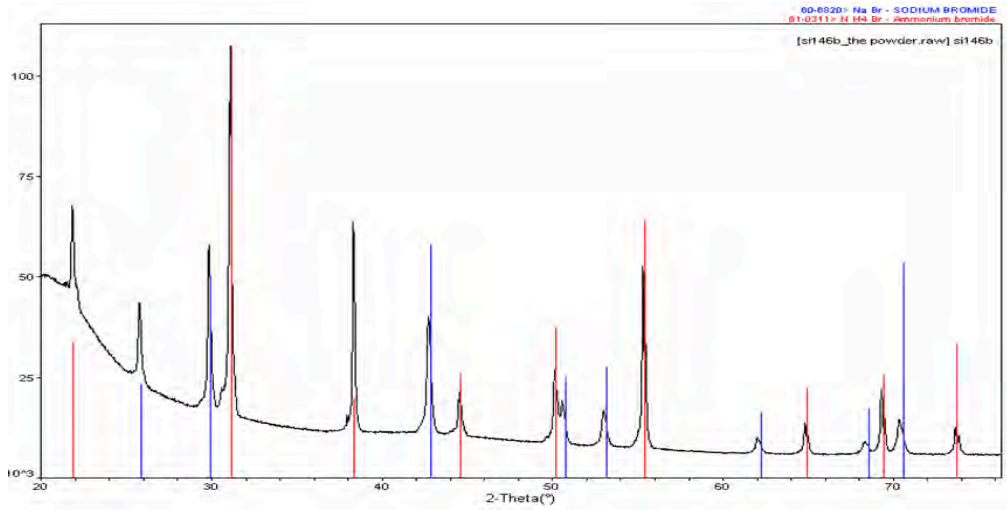

Figure 20. XRD data for the 1:3 NaSi:NH_4Br before washing with water. Blue lines indicate NaBr, red lines indicate NH_4Br.

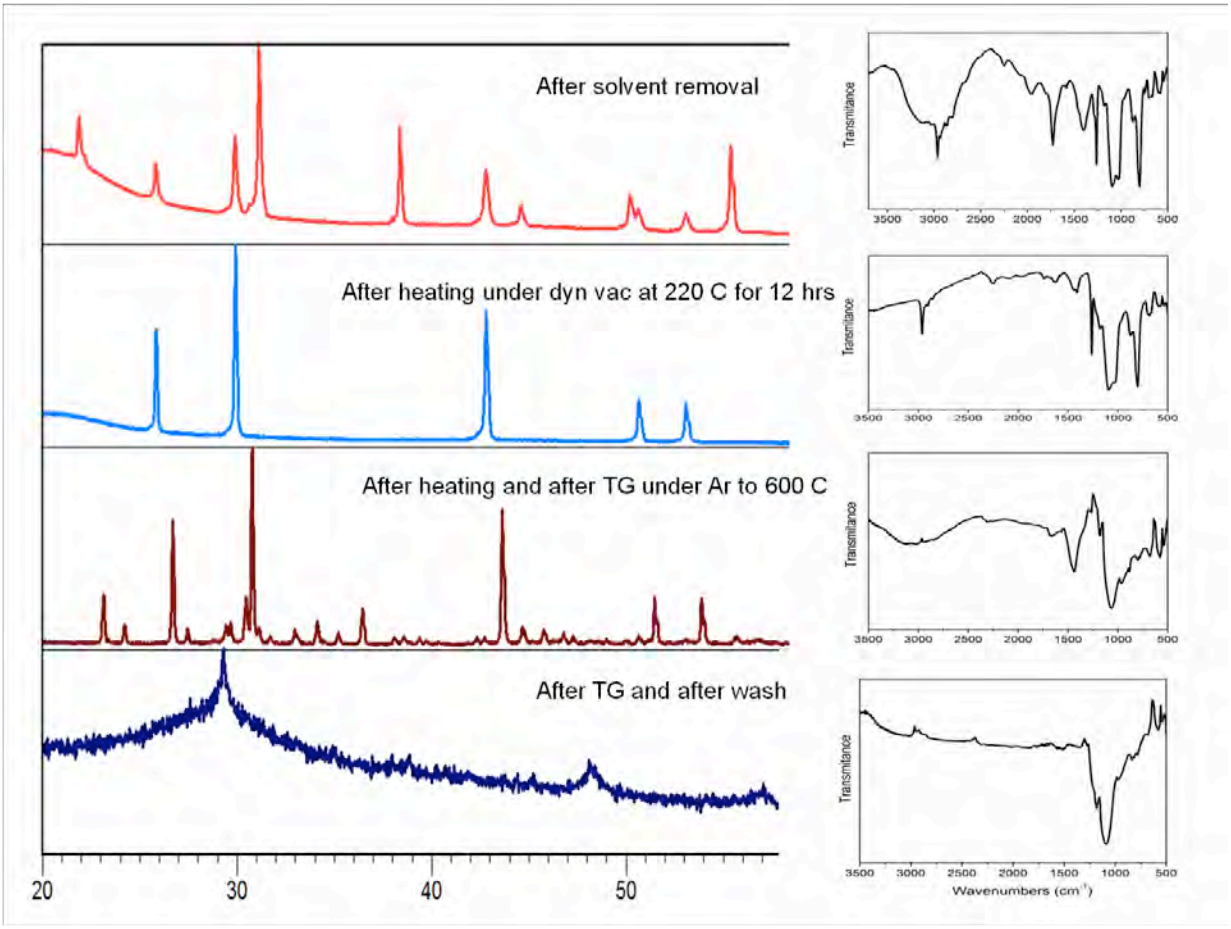

Figure 21. XRD and FTIR data for the 1:3 NaSi:NH_4Br before washing with water.

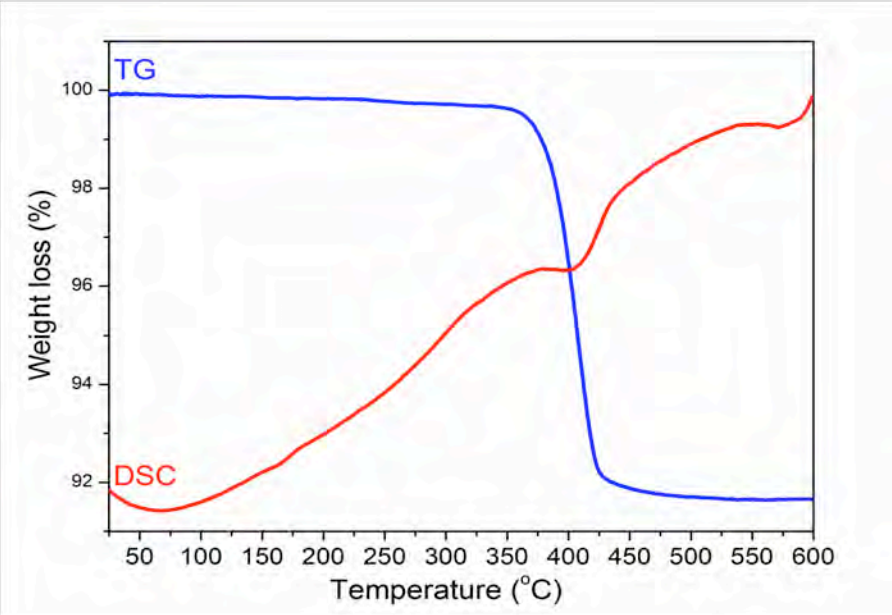

Figure 22. TG/DSC data for NaSi:NH_4Br 1:3.

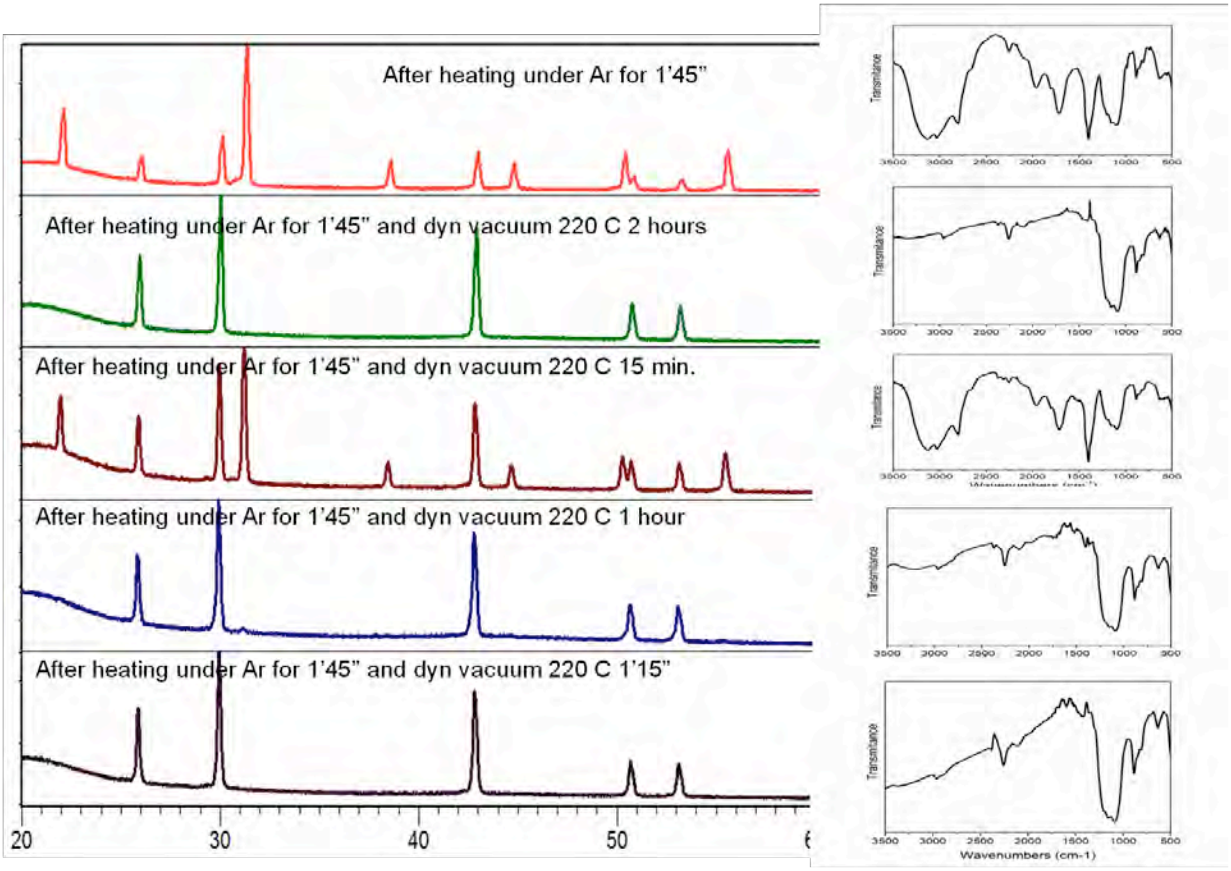

Figure 23. XRD and FTIR data used to monitor the reaction of NaSi with NH_4Br 1:3.

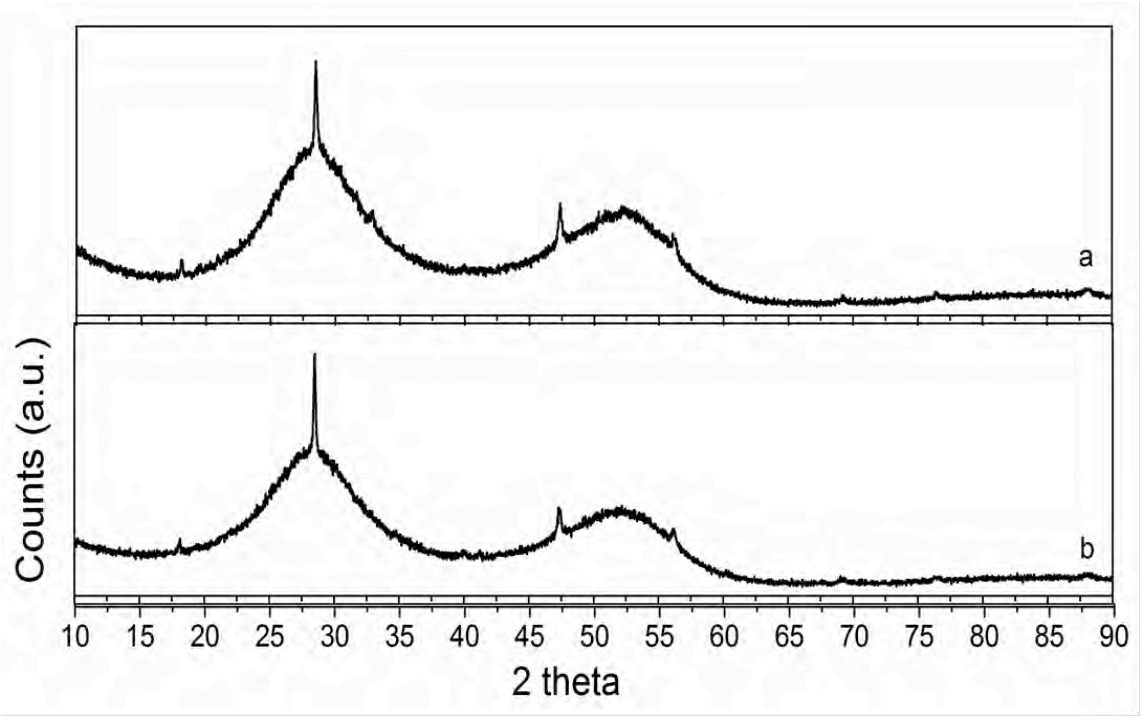

Figure 24. XRD data for 1:1 molar ratio of NaSi:NH_4Br, at 300 ºC for 14 hours, a) static vacuum, b) ambient pressure (bubbler).

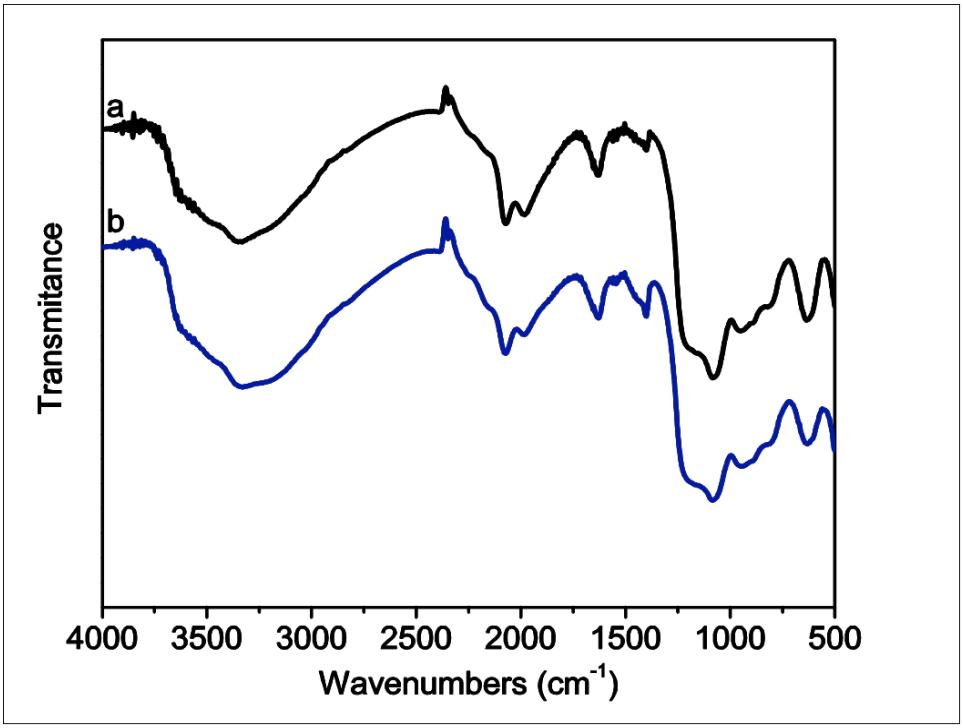

Figure 25. XRD data for 1:1 NaSi:NH_4Br molar ratio, at 300 ºC for 14 hours, a) static vacuum, b) ambient pressure (bubbler).

.

The Si NPs alloyed with B and C were prepared by a reaction route similar to the preparation of Si NPs. The first step was to synthesize a Zintl salt, $NaSi_{1-x}E_x$ (E = B, C, x = 0.1, 0.2, 0.3, 0.3, 0.4). Our research was motivated by a theoretical study that has predicted C doped Si NPs to be able to release hydrogen at lower temperatures as compared to Si NPs. We anticipated that higher loading of the dopant may lead to the collapse of the Zintl structure and phase segregation will occur. For the preparation of the Zintl salt, $NaSi_{1-x}E_x$ (E = B, C, x = 0.1, 0.2, 0.3, 0.3, 0.4), two methods have been used. One method was following the solid state traditional approach, whereas the second method utilized solid components that are welded in a niobium or tantalum tubes, that is to encapsulate in a quartz jacket and the whole ensemble is heated at 650 °C for a few days. The other approach was developed in our laboratory, and it is a much lower temperature reaction, shorter time and is a self cleaning reaction in which Si and B oxide layers on the individual particles are removed by reaction with H_2 resulting from the decomposition of NaH. This second approach has also been optimized for the production of NaSi via a low temperature route in our laboratory and a paper was published in Dalton Transactions in 2009. The three components are ball milled in a Spex mill for 10-20 minutes to ensure intimate grinding. Figures 26 and 27 show a schematic view of the reaction conditions and experimental setups used. Although only B doped materials are shown here, the same strategy was adopted for the C doped NaSi. The doped C and B NaSi materials have been characterized by XRD. An image of the NaSi crystal structure is shown in Figure 28. It was assumed that the monoclinic unit cell of NaSi, presented in which Si is arranged in $[Si_4]^{4-}$ tetrahedra surrounded by 4 Na^+ cations will be preserved, and some of the Si in these tetrahedra will simply be replaced by B and C. In the case of C, the doping was straight forward as both C and Si are group 14 and favor a tetrahedral arrangement. In the case of boron however, problems were anticipated, as B is known to favor icosahedral arrangements and hence low levels of doping with the NaSi structure preservation were expected. Attempts were made to solve the crystal structure by identifying where B replaces Si. The atomic positions for Na and Si in NaSi are presented in Table 1. The XRD was interpreted based on the decrease of peak intensities due to the replacement of Si with lighter elements. Based on our observed and simulated XRD powder patterns, comparisons presented in Figures 30 to 33 concluded that B is very likely located in position 2 (8f presented in Table 1). There is a very sharp reflection that increases with increasing the B content, ~ 32 2 theta, shown in Figure 30. Doing a similar analysis, e.g. simulating an XRD powder pattern with moving B on the two available Si positions in the crystal structure, such a strong reflection should not be there. NaSi has a low symmetry unit cell, e.g. monoclinic, and a reflection is expected at that position. Peak intensities in a diffraction pattern are known to be subject to preferred orientation, in which case a certain atomic plane appears more intense in the powder pattern. Preferred orientation is due to the nature of the sample and preparation for the XRD analysis. Unit cell evolution with increasing B content in NaSi was also tested via performing a series of refinements to determine the unit cell. The results are presented in Table 2. The following formula was used to determine the unit cell volume.

A typical refinement used to determine the unit cell using NaSi cell as a starting point is presented in Figure 34. As can be seen from Table 2 there is a unit cell contraction consistent with the replacement of a Si atom with a smaller B atom in the unit cell.

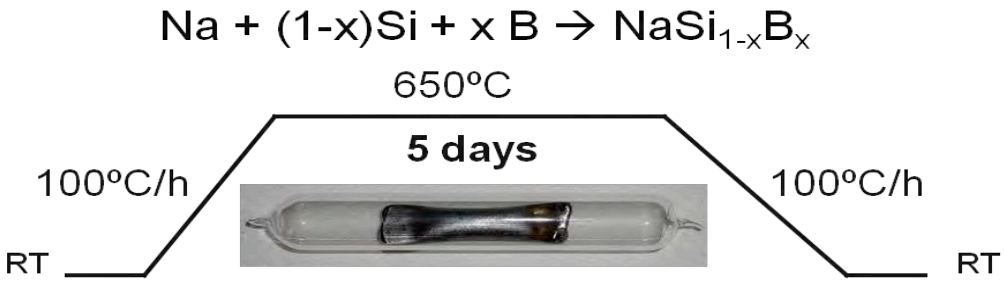

Figure 26. Traditional synthesis for $NaSi_{1-x}B_x$.

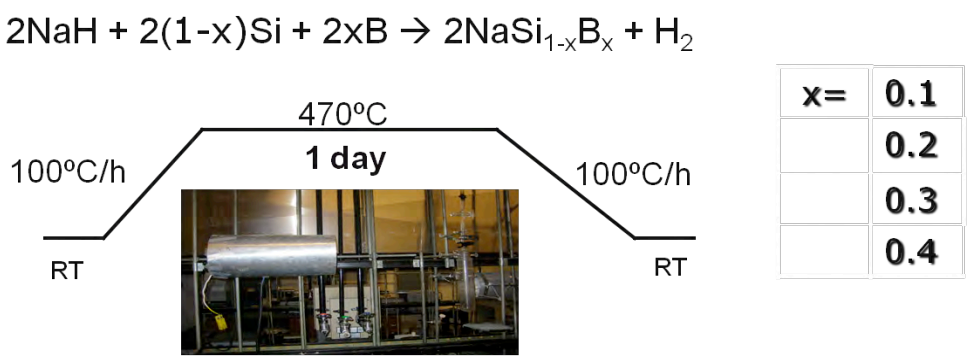

Figure 27. New synthesis for $NaSi_{1-x}B_x$.

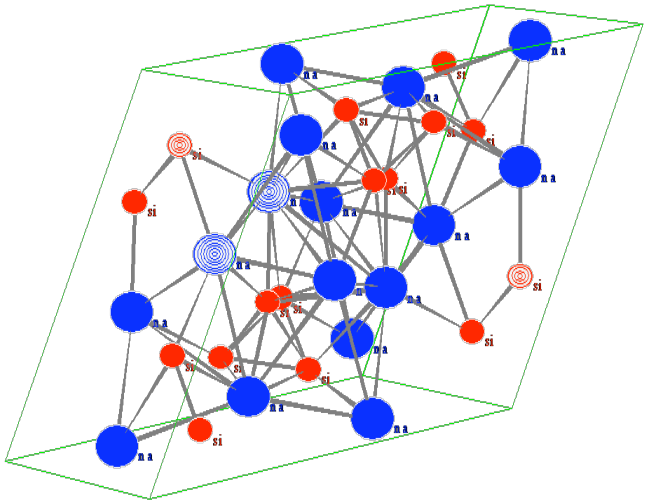

Figure 28. Picture of NaSi crystal structure. Na is represented with blue and Si with red spheres.

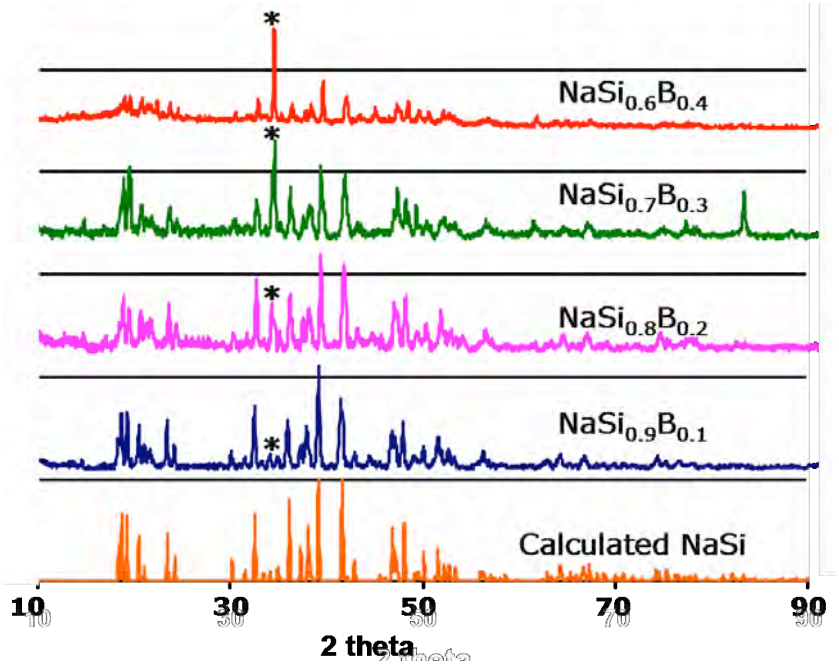

Figure 29. XRD data for NaSi Zintl phase doped with B.

Table 1. Atomic positions for Na and Si in NaSi (C2/c space group).

atom	Occupancy	Site	X	y	z	
Na(1)	1	8f	0.351	0.662	0.358	
Na(2)	1	8f	0.632	0.900	0.455	
Si(1)	1	8f	0.440	0.210	0.314	← Position 1
Si(2)	1	8f	0.597	0.463	0.357	← Position 2

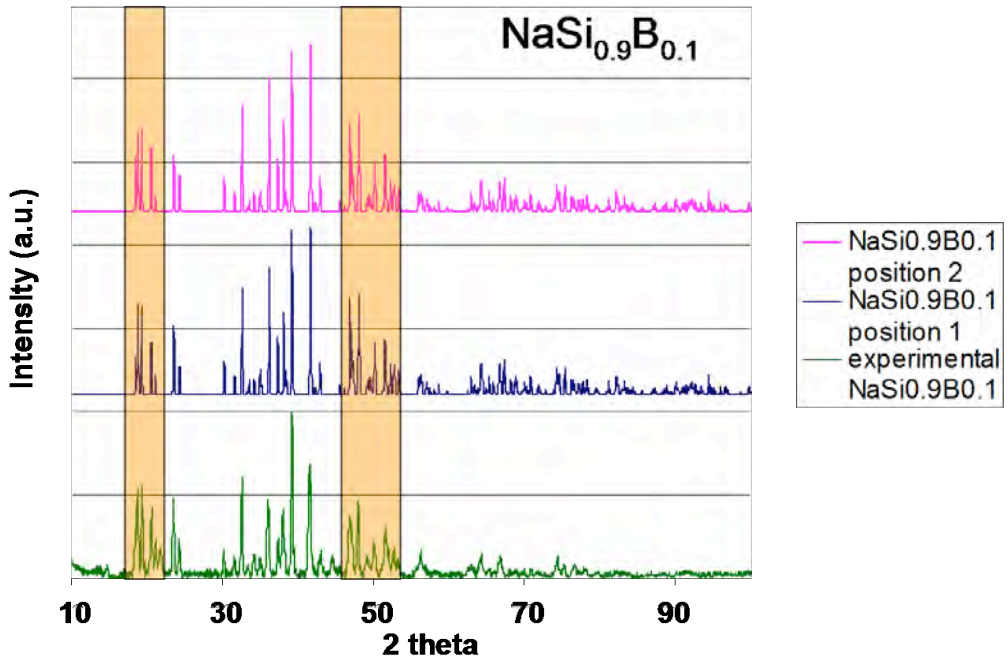

Figure 30. XRD data for $NaSi_{0.9}B_{0.1}$, bottom (green) experimental XRD data, blue simulated placing B in 8f position 1, see Table 1, magenta and top is the simulated XRD data placing B in position 2. the highlighted regions of these XRDs represent the regions most affected by changing Si and B positions in the crystal structure.

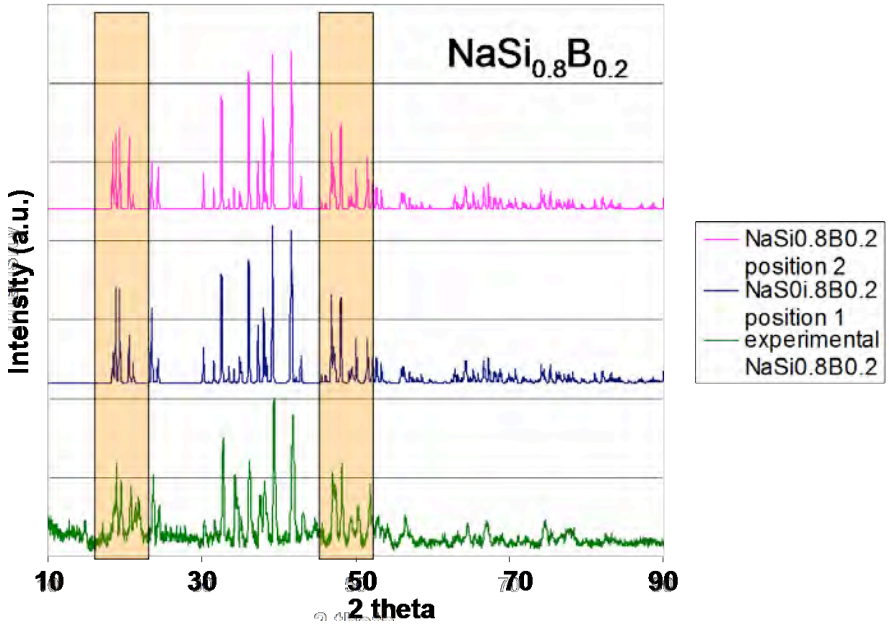

Figure 31. XRD data for $NaSi_{0.8}B_{0.2}$, bottom (green) experimental XRD data, blue simulated placing B in 8f position 1, see Table 1, magenta and top is the simulated XRD data placing B in position 2. the highlighted regions of these XRDs represent the regions most affected by changing Si and B positions in the crystal structure.

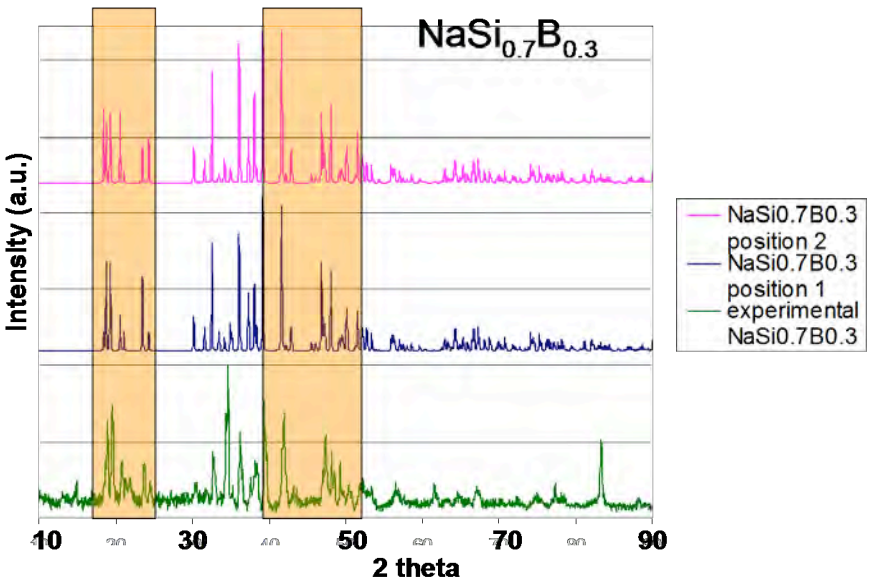

Figure 32. XRD data for $NaSi_{0.7}B_{0.3}$, bottom (green) experimental XRD data, blue simulated placing B in 8f position 1, see Table 1, magenta and top is the simulated XRD data placing B in position 2. the highlighted regions of these XRDs represent the regions most affected by changing Si and B positions in the crystal structure.

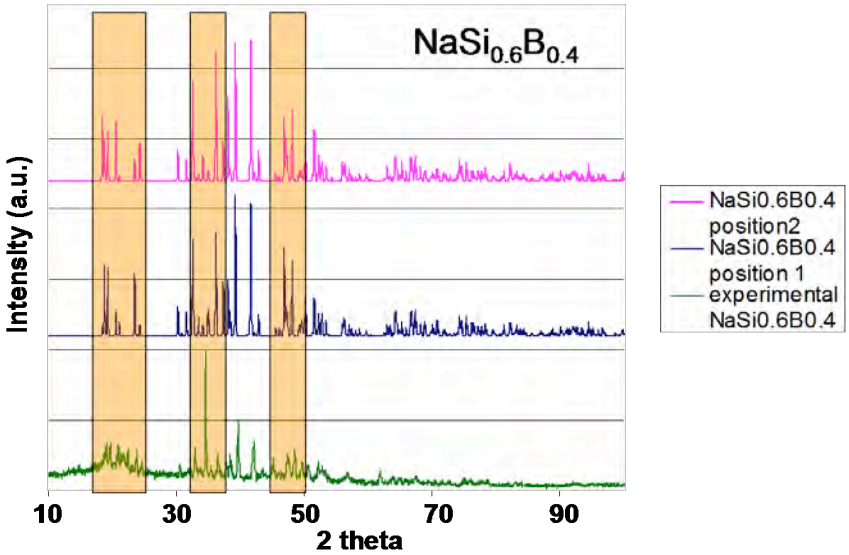

Figure 33. XRD data for $NaSi_{0.6}B_{0.4}$, bottom (green) experimental XRD data, blue simulated placing B in 8f position 1, see Table 1, magenta and top is the simulated XRD data placing B in position 2. the highlighted regions of these XRDs represent the regions most affected by changing Si and B positions in the crystal structure.

Table 2. Monoclinic unit cell evolution with increasing B content in NaSi

	a (Å)	b (Å)	c (Å)	β°	Volume (Å ^{3})	STD (Å^3)
NaSi	12.19	6.55	11.18	119	**780.739**	----
$NaSi_{0.9}B_{0.1}$	12.17306	6.52898	11.12661	118.9073	**774.1337**	4.45E-09
$NaSi_{0.8}B_{0.2}$	12.09318	6.52674	11.07325	118.9495	**764.7917**	4.04E-09
$NaSi_{0.7}B_{0.3}$	12.10962	6.53249	11.09627	118.9482	**768.1092**	5.03E-09
$NaSi_{0.6}B_{0.4}$	12.14812	6.53928	11.11578	119.3037	**770.0416**	3.11E-08

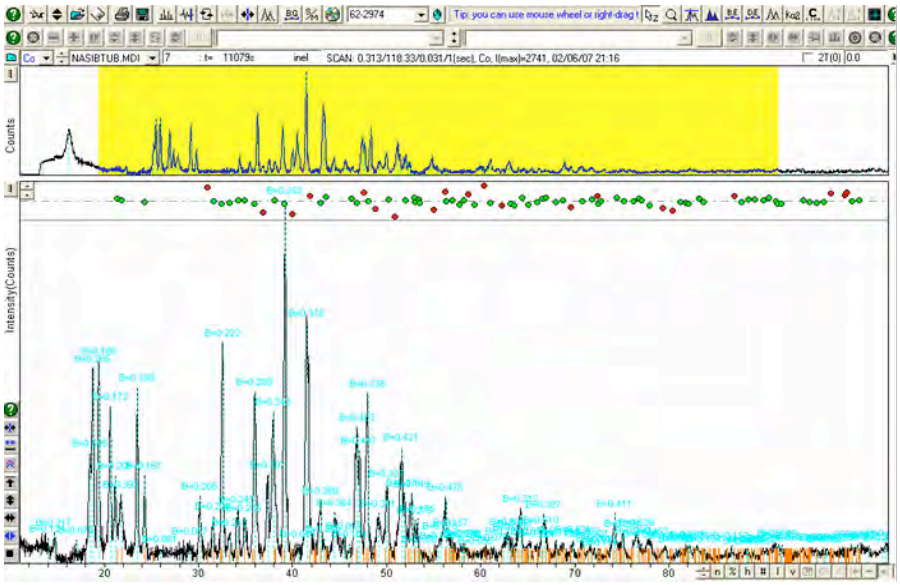

Figure 34. XRD refinement for NaSi doped with boron.

A powder pattern for the 20% doped C NaSi material is presented in Figure 35.

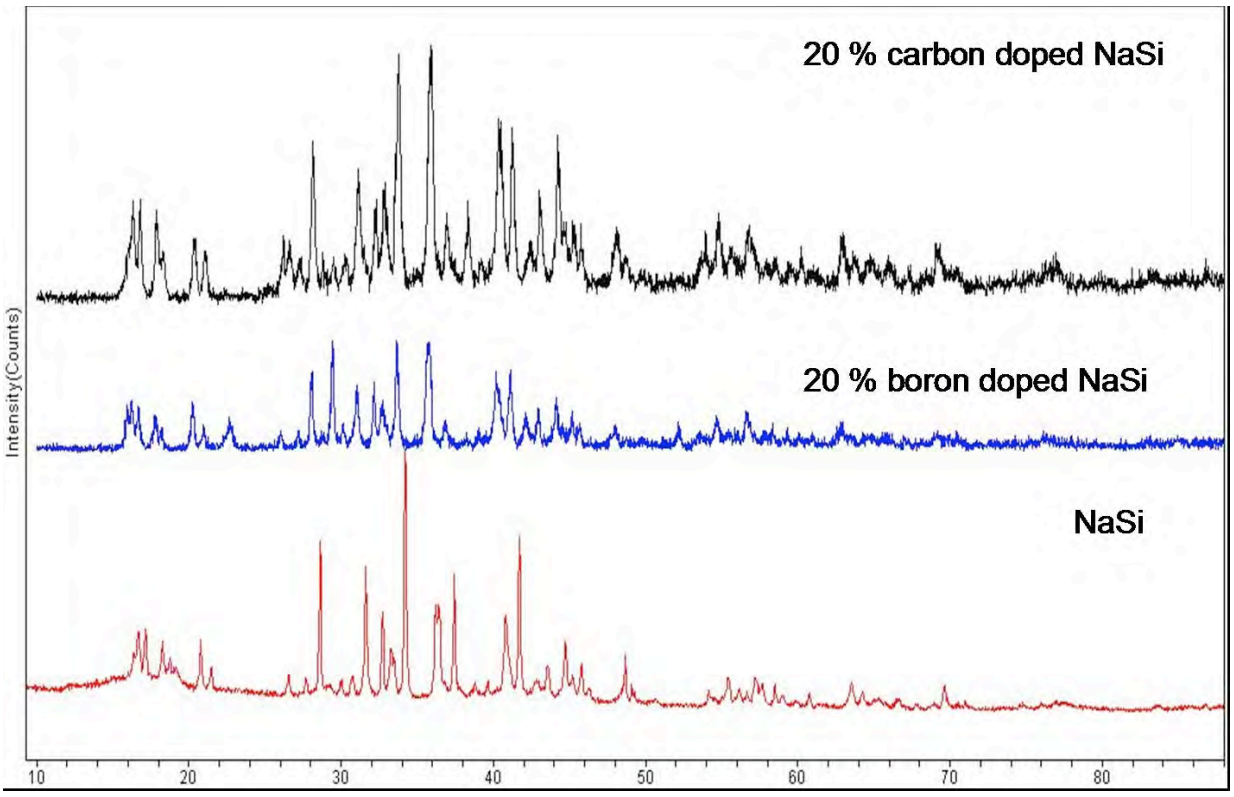

Figure 35.XRD data for NaSi, $NaSi_{0.8}B_{0.2}$ and $NaSi_{0.8}C_{0.2}$.

The doped Zintl salts prepared as outlined above were used with the optimized synthesis to produce the C and B doped Si NPs. The synthesis was performed in DME, using a 1:3 molar ratio $NaSi_{1-x}E_x$: NH_4Br. At the end of reaction the powder was separated from the solvent and heated at 220 °C under argon for 1 hr and 45 minutes for $NaSi_{0.8}B_{0.2}$ and for 30 minutes for the $NaSi_{0.8}C_{0.2}$. The FTIR and XRD data obtained after heat treatment of these samples are presented in Figure 36. The TG/MS data, only the hydrogen channel is shown in Figure 37. As one can see from this figure, the C doped Si NPs lowers the dehydrogenation temperature as compared to Si NPs, while the B doped Si NPs increase the dehydrogenation temperature. In the C doped Si NPs the dehydrogenation is consistent with a step-by-step process with only 4% H_2 being released just above 200 °C. Another 4% is released above 300 °C, and the remainder is evolved above 500 °C.

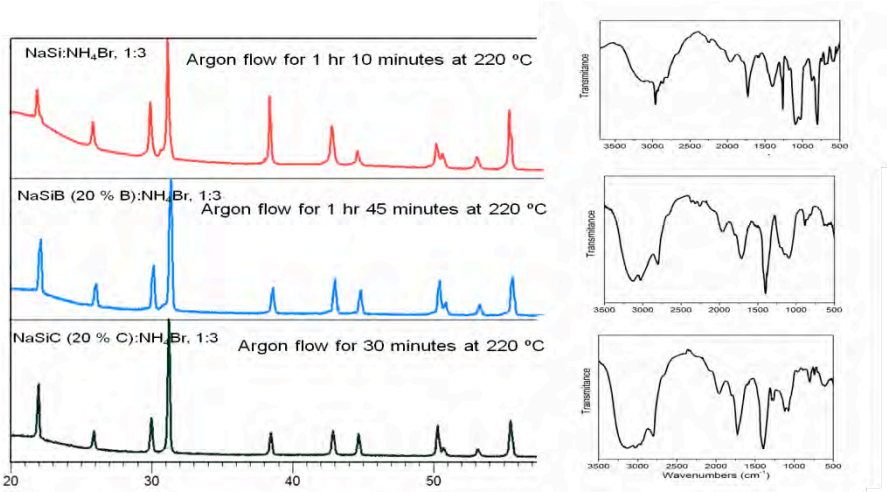

Figure 36. XRD and FTIR data for heat treated NaSi, $NaSi_{0.8}B_{0.2}$ and $NaSi_{0.8}C_{0.2}$ NPs.

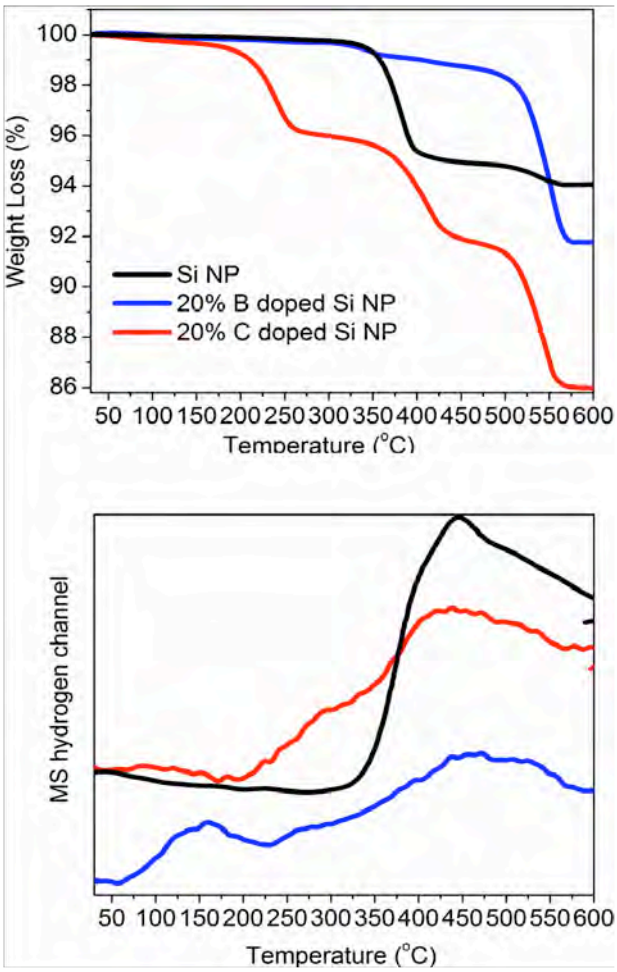

Figure 37. TG/MS data for the B and C doped Si NPs.

I.3. Boron Nanoparticles

The synthesis of amorphous, surface-functionalized boron NPs has been achieved *via* the reduction of boron tribromide with sodium naphthalenide and subsequent reaction with octanol.

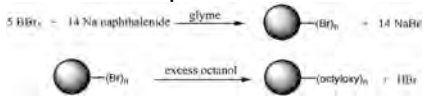

This was the subject of a published communication in Chem. Commun. 2007. Solution ^{1}H NMR ($CDCl_3$) indicates the presence of the octyloxy-capping groups on the surface of the nanoparticles, which is further supported by FTIR analysis with absorbances corresponding to alkyl C–H groups between 2800 and 3000 cm^{-1} and B-OR groups at ca. 800 cm^{-1}. The solution ^{11}B NMR ($CDCl_3$) spectrum shows a resonance at 18.5 ppm with respect to BF_3.OEt (0 ppm), which is consistent with results obtained for molecular B-OR compounds and provides further evidence of B-O bonding on the surface of the particles. Figure 1 shows TEM micrographs of a number of the octyloxy-capped boron nanoparticles. The size distribution of the particles was determined by measuring 937 nanoparticles from different regions of the grid. Analysis of the particle size distribution indicates that the particles lie in the range 1 to 45 nm (with 1.8 % lying in the range 30 to 45 nm). The majority of particles are 1-3 nm (54 %), with the remaining particles quite evenly distributed between 4 to 20 nm.

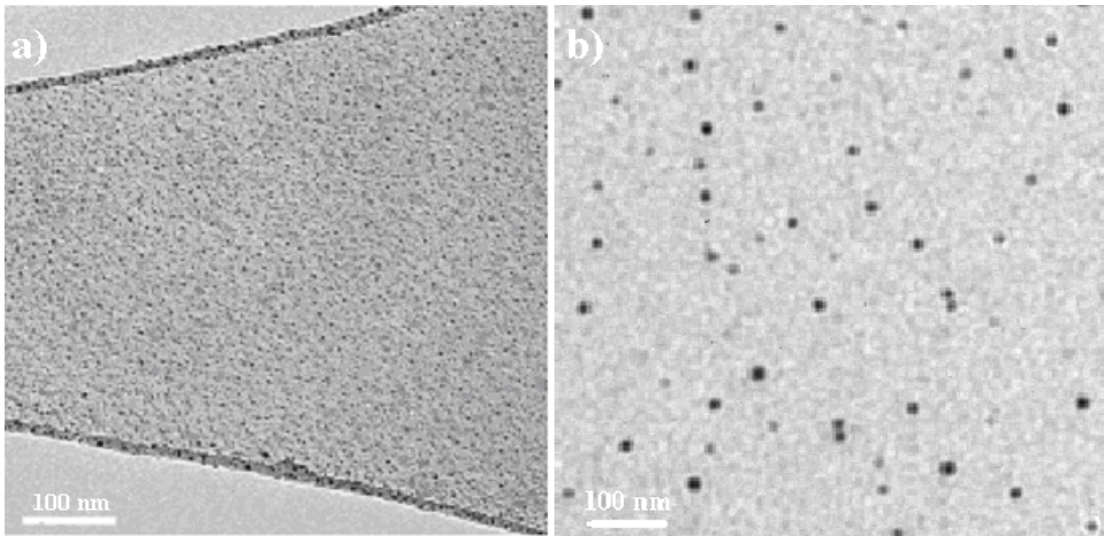

Figure 38. Low magnification, bright field TEM images showing examples of a) 2-4 nm boron particles and b) 18-20 nm boron particles.

Elemental analysis via EDS (electron dispersive X-ray spectroscopy) is not possible on elements lighter than carbon, so a combination of STEM and EELS has been used to confirm the presence of boron in the particles. Figure 2a shows a STEM dark field image of the octyloxy-capped amorphous boron nanoparticle, with a diameter of approximately 37 nm. Measurements were also performed on particles of each size range (20 and 3 nm), and concluded the presence of boron in each. The low loss spectra in Figure 2b are normalized to the height of the zero loss peak and trace the increased intensity of the plasmon peak (~ 24 eV) on the particle (points 3-6). The low loss region in EELS provides a quantitative measure of the specimen thickness. In the case of the measured boron NP the specimen thickness varies from

0.09 (points 1 + 7; on the carbon foil) to a maximum thickness of 0.20 t/λ inelastic (point 5). The core loss spectra (Figure 6c) were background subtracted using a power low fit and corrected for multiple scattering using a Fourier-log deconvolution algorithm. As expected, the intensity of the boron K edge increased to a larger extent towards the centre of the particle with respect to the oxygen K edge.

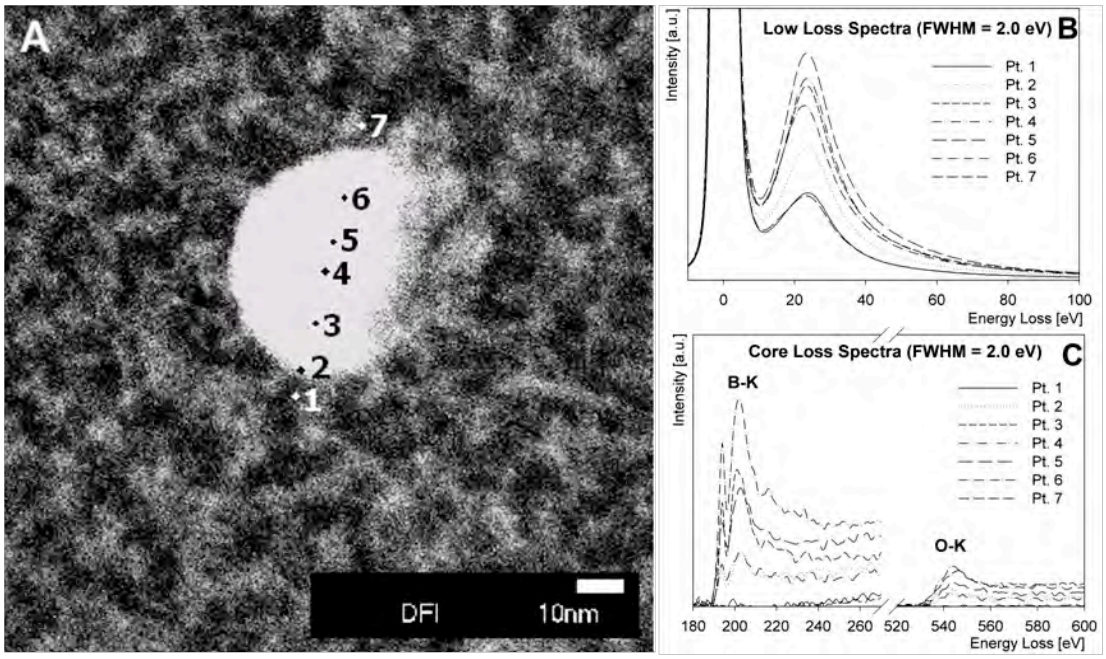

Figure 39. A) High-resolution Z-contrast image in STEM mode of an octyloxy-capped amorphous boron nanoparticle showing the position and the actual probe size (1 nm) of the EELS line scan across the particle, B) low loss and C) core loss spectra of the different positions (Point 1-7). All core loss spectra are background subtracted and Fourier-log deconvoluted.

Publications on light element nanoparticles:

1. “Low-Temperature Solution Route to Macroscopic Amounts of Hydrogen Terminated Silicon Nanoparticles”, D. Neiner, H. W. Chiu, and S. M. Kauzlarich, J.A.C.S., 2006; 128(34); 11016-11017.

2. "Room Temperature Synthesis of Surface-Functionalised Boron Nanoparticles", Pickering, Alexandra L., Mitterbauer, Christoph, Browning, Nigel D., Kauzlarich, Susan M., Philip, Philip P., Chemical Communications, 2007, 580.

3. A new solution route to hydrogen-terminated silicon nanoparticles: synthesis, functionalization and water stability”, X. Zhang, D. Neiner, S. Wang, A. Y. Louie, S. M. Kauzlarich, *Nanotechnology* , 2007, 18(9), 095601/1-095601/6

4. A Versatile Low Temperature Synthetic Route to the Zintl Phase Precursors: Na_4Si_4, Na_4Ge_4 and K_4Ge_4 as Examples”, M. Xuchu, X. Fen, T. Atkins, A. Goforth, D. Neiner, A. Navrotsky, and S. M. Kauzlarich, *Dalton. Trans*., 46, 10250, 2009.

5. “Hydrogen-Capped Silicon Nanoparticles as a Potential Hydrogen Storage Material: Synthesis, Characterization, and Hydrogen Release", D. Neiner, S. M. Kauzlarich, *Chem. Mater*., 22(2), 487-493, 2010.

II. **Hydrogen Storage in Silicon Clathrates**

II.1. Sodium and Potassium Silicon Clathrates

Two silicon clathrates that encapsulated hydrogen have been prepared, $Na_{5.5}(H_{2.15})_2Si_{46}$ and a potassium analogue, $K_{8-x}(H_2)_ySi_{46}$. In these materials the silicon framework cages contain both the alkali metal and molecular hydrogen. These materials have been prepared via the solid state reaction of ammonium bromide with the Zintl salt ASi (A = Na, K) under dynamic vacuum at 300˚C. X-ray diffraction data are consistent with clathrate type I structure. Type I clathrate phases have two types of cages where the guest species, in this case Na or K and H_2, can reside: a large cage composed of 24 Si, in which the guest resides in the 6d position, and a smaller one composed of 20 Si, in which the guest occupies the 2a position. A picture of the crystal structure of a type I silicon clathrate is shown in Figure 40. ^{23}Na, ^{1}H, ^{29}Si MAS NMR show that hydrogen and sodium are distributed among the 2a and 6d sites. However, there is a preference for Na to occupy the 2a sites (smaller Si cages), and hydrogen has a greater affinity for the 6d site. The ^{1}H NMR spectrum shows several peaks, the peak shapes are consistent with mobile hydrogens in the large cage. Elemental analysis confirms the presence of hydrogen in these materials. Sodium and potassium occupancy was examined using spherical aberration (Cs) corrected scanning transmission electron microscopy (STEM). The high-angle annular dark-field (HAADF) STEM indicate that the Na occupancy of the large cage, 6d sites, is less than 2/3, consistent with the NMR and elemental analysis. Interestingly the (HAADF) STEM experimental and simulated images indicated that the K is deficient in both the 2a and the 6d sites. Figure 41 shows a HRTEM and SAED image of the sodium silicon clathrate. Figure 42 shows a HRTEM along different crystal axes for the sodium silicon clathrate, along with an SAED image that confirms the clathrate type I structure. Figure 42 presents a STEM-HAADF data that along with elemental analysis; ^{1}H MAS NMR and ^{23}Na NMR data confirms the sodium deficiency and hydrogen presence in this material. Figure 43 presents a STEM-HAADF data for the potassium clathrate that confirms potassium deficiency in this material and shows that potassium is deficient in both 6d and 2a sites. That makes the hydrogen present in this material randomly distributed among the 2 guest positions in the crystal structure. Figure 44 presents a Rietveld refinement of the X-ray diffraction data for the sodium silicon clathrate. Figure 45 and 46 present the MAS NMR ^{1}H and ^{29}Si data. The TGA/DSC/MS data for both of these materials show that the dehydrogenation occurs above 100°C. Above 500°C,the silicon clathrate structure collapses into the thermodynamically more stable diamond silicon structure. Figure 47 shows a typical TG/MS trace for the sodium silicon clathrate, showing that ~1.5% H_2 evolves above 100°C from this material.

This research has been published in three papers and the references are cited at the end of this chapter.

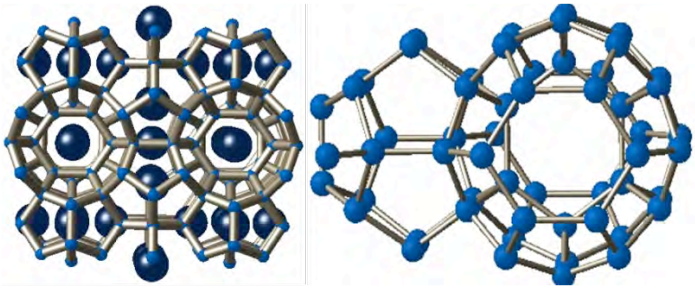

Figure 40. Crystal structure for a type I silicon clathrate (left), picture of the Si_{20} and Si_{28} cages (right).

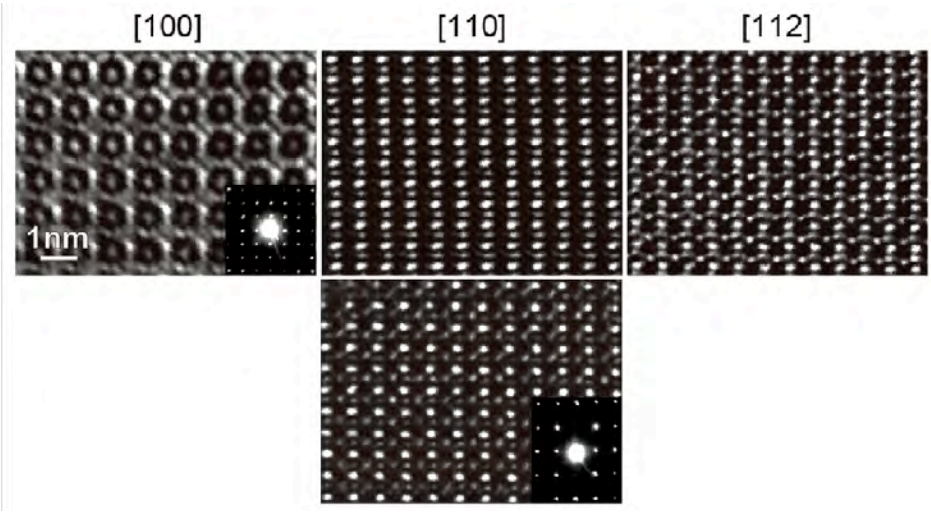

Figure 41. HRTEM and SAED for the sodium silicon clathrate

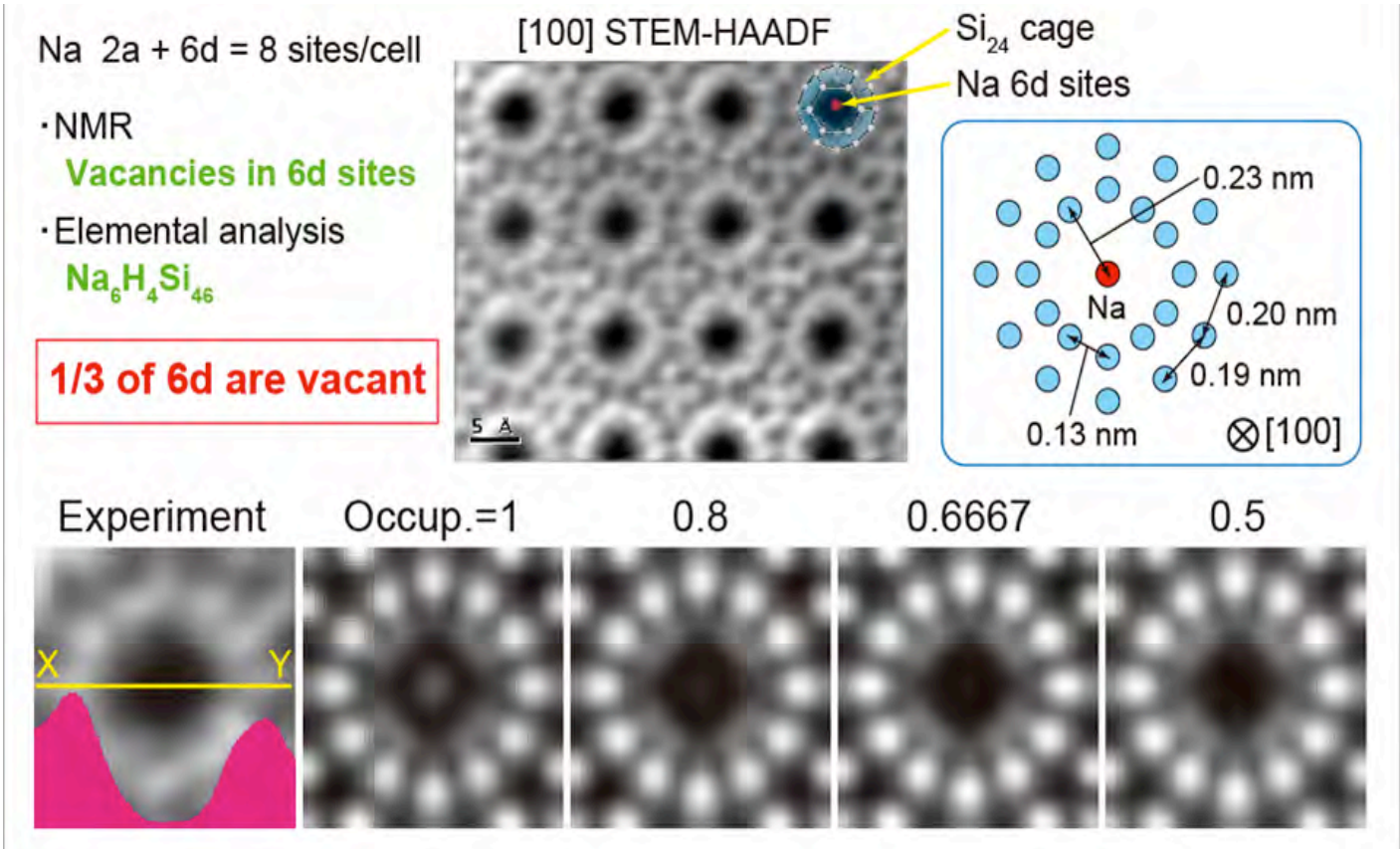

Figure 42. STEM-HAADF for the sodium silicon clathrate

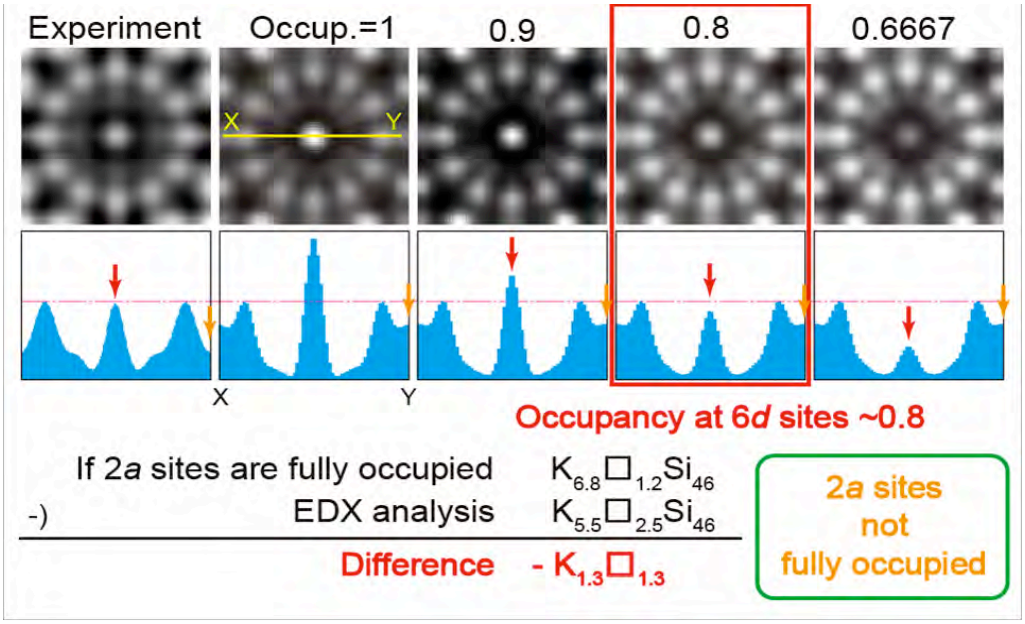

Figure 43. STEM-HAADF for the potassium silicon clathrate.

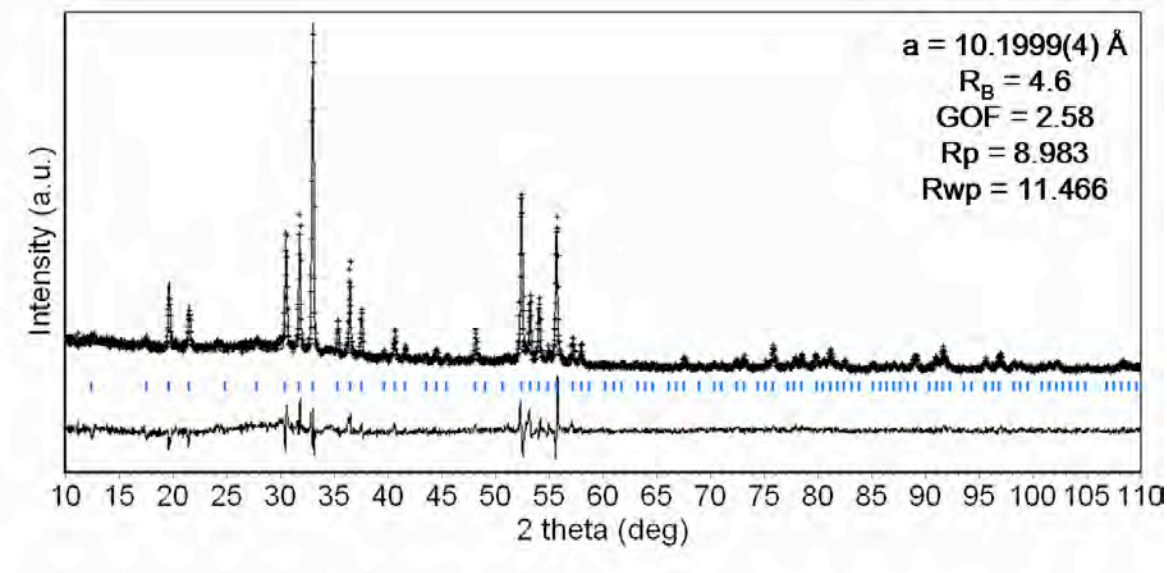

Figure 44. Rietveld refinement of the X-ray diffraction data for the sodium silicon clathrate.

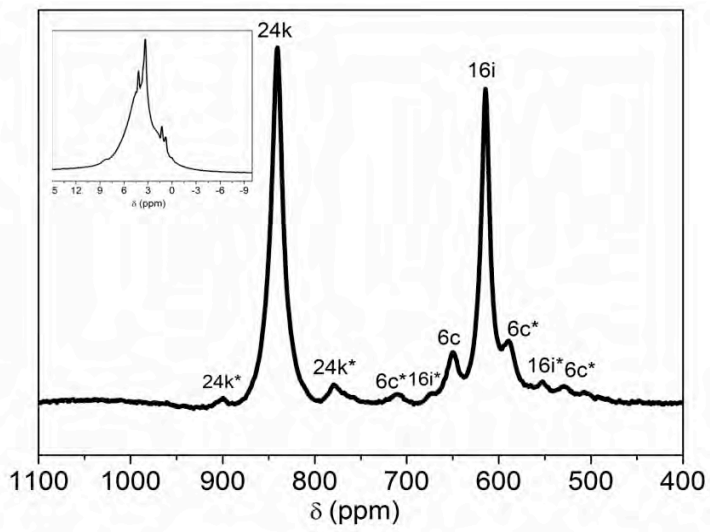

Figure 45. ^{1}H NMR and ^{29}Si NMR for the sodium silicon clathrate.

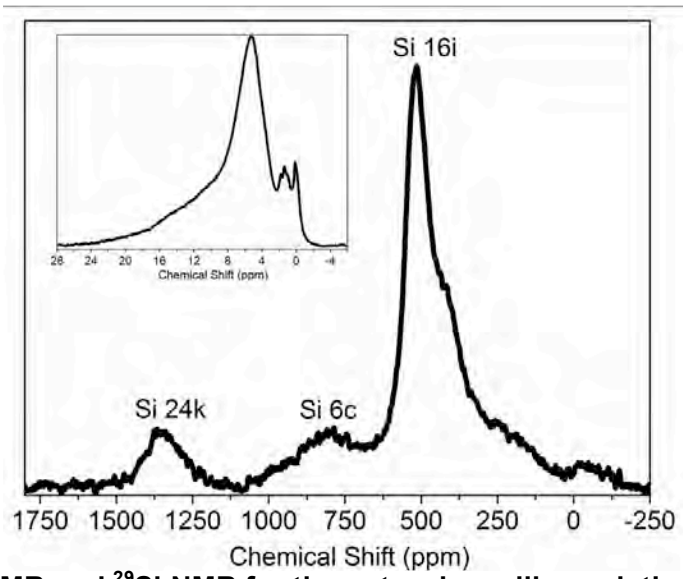

Figure 46. MAS ^{1}H NMR and ^{29}Si NMR for the potassium silicon clathrate.

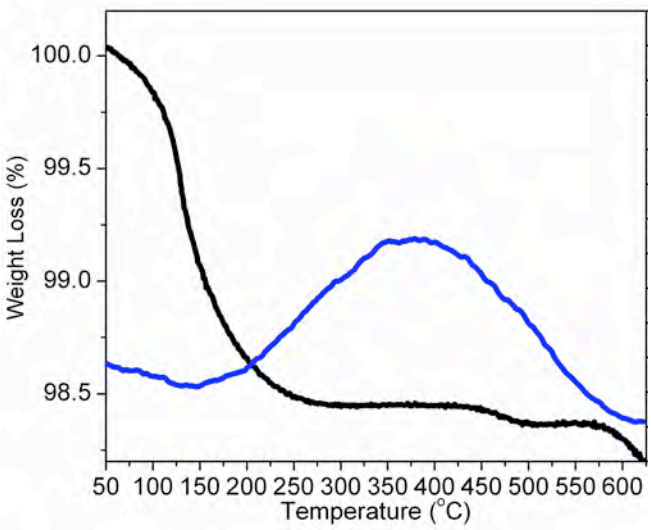

Figure 47. TG- black line, MS hydrogen channel- blue line for the sodium hydrogen silicon clathrate.

1. References

1. "Synthesis and Characterization of $K_{8-x}(H_2)ySi_{46}$" D. Neiner, N. L. Okamoto, P. Yu, et al., Inorg. Chem., 49 (3), 815-822, 2010.

2. “Characterization of hydrogen encapsulated type I silicon clathrate”, N. L. Okamoto, D. Neiner, C. L. Condron, Q. M. Ramasse, P. Yu, N. D. Browning and S. M. Kauzlarich, Microsc. Microanal. 13 (Suppl. 2), 2007.

3. “Hydrogen Encapsulation in a Silicon Clathrate Type-I Structure: $Na_{5.5}(H_{2.})_{2.15}Si_{46}$: Synthesis and Characterization”, D. Neiner, N. L. Okamoto, C. L. Condron, Q. M. Ramasse, P. Yu, N. D. Browning and S. M. Kauzlarich, J. Am. Chem. Soc., 129 (45), 13857 -13862, 2007.

III. Regeneration and Hydrogen Release of AB using Si NPs

III.1. Si-H nanoparticle used for the regeneration of B-O and B-Cl to B-H

We explored the regeneration of B–H bonds from B–O and B-Cl model systems, by reacting nanoparticles of hydrogen terminated Si with $B(OPh)_3$, $B(OBu)$ and BCl_3 in solution. Several approaches were taken to react the NPs directly and a solution of NPs with $B(OPh)_3$: large sized (≥ 10 nm) and small sized (≤10 nm) NPs were employed. Both solid phase and solution synthetic procedures were employed. Both of these synthetic approaches provided positive evidence for the replacement of B–O with B–H. These approaches are outlined by the following reactions:

$NaSi + NH_4Br + B(OR)_3 \rightarrow Si_y(OR)_xH_{1-x} + BH_x(OR)_{3-x} + H_2 + NH_3 + NaBr$ (THF, 60˚C), R=Ph, tBu

$Si)H + NH_4Br + B(OR)_3 \rightarrow Si_y(OR)_xH_{1-x} + BH_x(OR)_{3-x} + H_2 + NH_3 + HBr$ (THF, 60˚C), R=Ph, tBu

$SF + NaSi + NH_4Br \rightarrow H_3NBH_3 + NaBr + H_2 + NH_3 + Si_y(OR)_x$ (THF, 60˚C), SF = BNH_x (x=1-2)

$SF + Si)H + NH_4Br \rightarrow H_3NBH_3 + HBr + H_2 + NH_3 + Si_y(OR)_x$ (THF, 60˚C), SF = BNH_x (x=1-2)

$CTB + NaSi + NH_4Br \rightarrow H_3NBH_3 + NaBr + H_2 + NH_3 + Si_y(OR)_x$ (THF, 60˚C), CTB = $N_3B_3H_{12}$

$CTB + NaSi + NH_4Br \rightarrow H_3NBH_3 + NaBr + H_2 + NH_3 + Si_y(OR)_x$ (THF, 60˚C), CTB = $N_3B_3H_{12}$

$BCl_3 + NaSi + NH_4Br \rightarrow H_3NBH_3 + NaBr + H_2 + NH_3 + Si_yCl_x$

These reactions have been monitored by FTIR and ^{11}B solution NMR. The general strategy was to optimize the time, temperature of reaction, substrate and the regenerator source, e.g. the silicon hydride particles of different sizes synthesized in situ or pre-prepared and added to the B substrate.

A few substrates have been used: two borates to test reactivity: triphenyl borate and tert butyl borate, cyclotriborazine, polyborazilene, boron trichloride and spent fuel. Two general types of Si)-H NPs have been used: Si NPs prepared as described via reaction (1) and those prepared in situ from the same reaction. Time and temperature have also been monitored and optimized; however, due to the low stability of AB in solution at elevated temperatures for prolonged time periods, it was expected that low temperatures and short reaction times would provide better performance. The time and temperature have been optimized as shown in Figures 48 and 49. Control reactions have been performed between the different substrates and NaSi, or NH_4Br, however the reaction moved forward only when both NH_4Br and NaSi were present. These results suggested at least two hypotheses that we can put forth:

1) the reaction proceeds in the presence of both a hydride from the Si NPs and a proton from the NH_4Br,

2) the NPs are formed in situ and then the hydride transfer to the substrate takes place.

It was found that in terms of substrates, triphenyl borate and the spent fuel performed the best. The tert butyl borate substrate was found to be unreactive under our reaction conditions. This is shown in Figure 52. The reaction between the silicon hydride NPs and boron trichloride was found to be effective in transferring a hydride from Si-H to B-H. However, due to the complications of solvent splitting by the very reactive BCl_3 with DME, this route has been abandoned. These latter results are summarized in Figure 51. It should be emphasized that the spent fuel reaction with NH_4Br and NaSi can be optimized to be a one pot synthesis for ammonia borane.

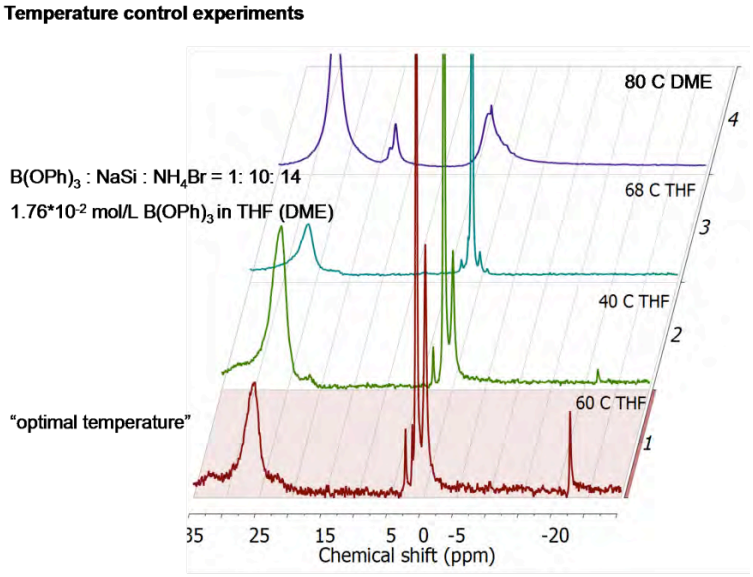

Figure 48. ^{11}B NMR data for the reaction of triphenyl borate with ammonium bromide and sodium silicide as a function of temperature.

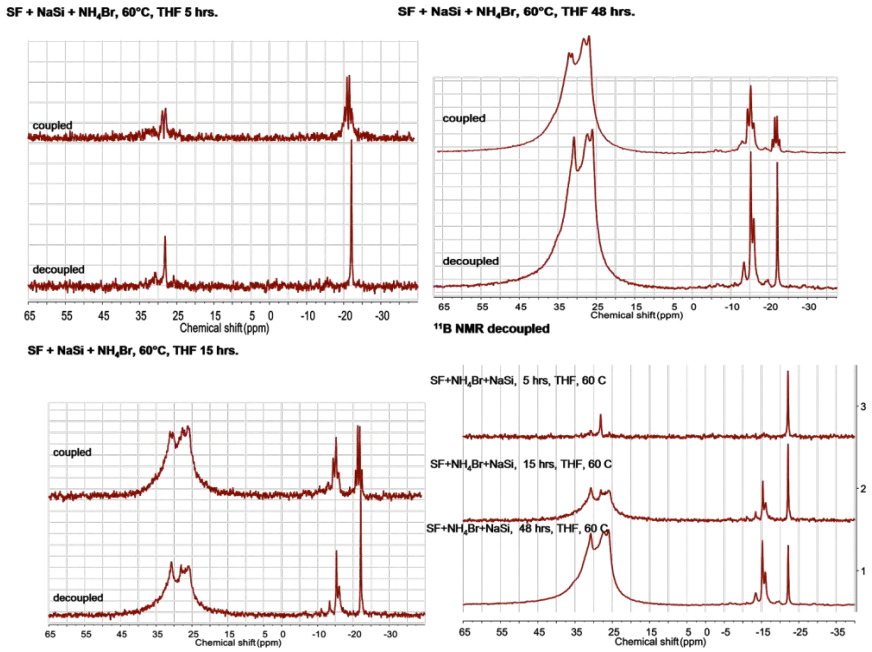

Figure 49. ^{11}B NMR data for the reaction of spent fuel (NBH_x) with ammonium bromide and sodium silicide as a function of time at 60ºC.

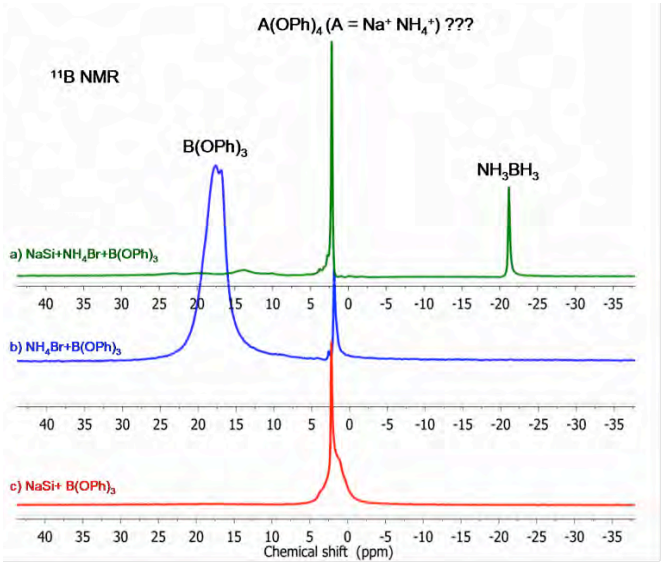

Figure 50.[11]B NMR data for the reaction of triphenyl borate with ammonium bromide and sodium silicide and the control reactions of sodium silicide with trophenyl borate and ammonuim bromide with triphenyl borate in glyme at 60ºC.

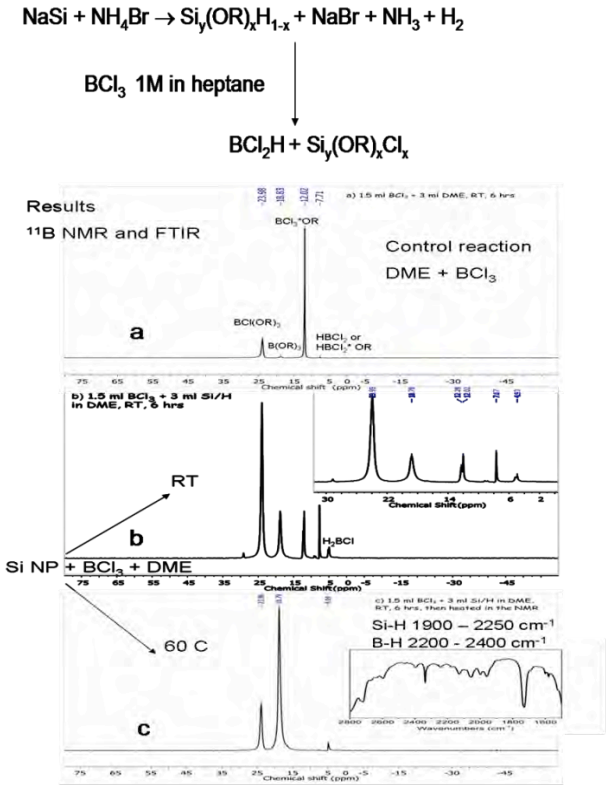

Figure 51. [11]B NMR data for the reaction of boron trichloride with ammonium bromide and sodium silicide in DME.

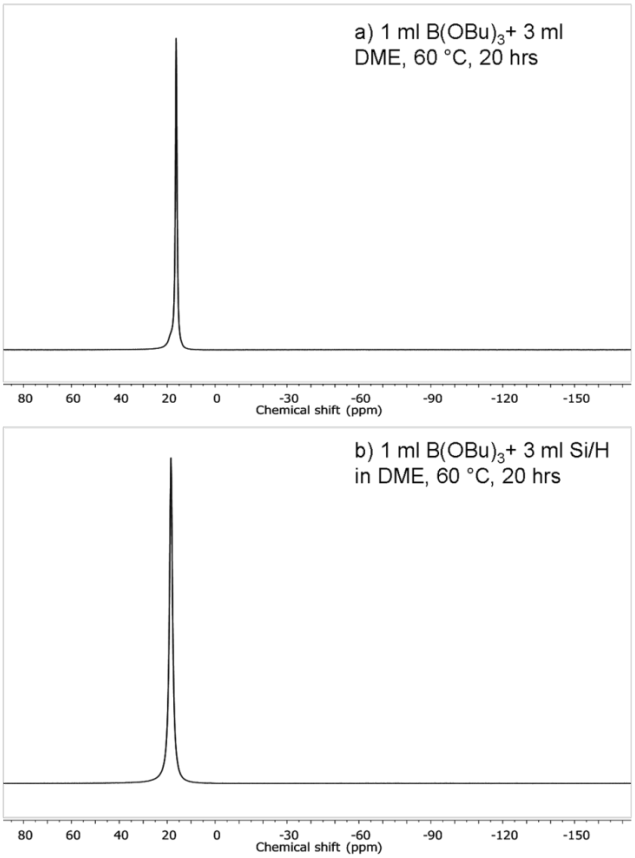

Figure 52. ^{11}B NMR data for the reaction of t-butyl borate with the silicon hydride NPs in glyme.

III.2. Light Element NPs to Aid Hydrogen Release from AB

Nano-boron nitride (nano-BN) aids in the dehydrogenation properties of AB. Several beneficial effects that pertain to the dehydrogenation properties of the mixtures of AB:nano-BN are notable, such as the decrease of the dehydrogenation temperature, the decrease in NH_3 formation as well as the decrease of the exothermicity of hydrogen release with increasing the nano-BN concentration.

Nano-BN was prepared by ball milling commercial hexagonal-BN (h-BN) powder for 1 hour. The samples studied were 4:1, 1:1 and 1:4 AB:nano-BN. The XRD data show that the samples prepared by ball milling nano-BN in the presence of AB are physical mixtures of the two solids. The XRD peaks index as h-BN, and they are broad indicating the formation of nanosized crystallite domains. AB is present as crystalline AB. The XRD data is presented in Figure 48. Figure 49 presents the SEM data showing that AB covers the nano-BN surface. This is consistent with the nano-BN surface area decreasing from 251 m^2/g to 24 m^2/g when AB is on the surface of nano-BN in a 1:1 by weight ratio. The TG/DSC/MS data for all of the prepared samples is shown in Figure 50. This data show that the dehydrogenation occurs at lower temperatures for AB:nano-BN as compared to AB neat, also the heat associated with the dehydrogenation is smaller than that of neat AB, and the sample does not foam for the higher nano-BN loadings. Another advantage is that ammonia evolution from the AB:nano-BN mixtures is lower than the one observed for AB neat, 20 ppm from AB:nano-BN 1:1 as compared to 200 ppm from neat AB. As a drawback, the amount of borazine seems to be increasing with increasing the amount of nano-BN.

Volumetric gas burette measurements at 90°C and 150°C were performed, and the results are presented in Figure 51. In addition, for comparison purposes, a neat AB sample has also been measured under the same conditions, e.g., 90°C and 150°C. Approximately 0.96 equivalents of hydrogen evolve at 90°C from the 1:1 sample, and 1 mole equivalent when neat AB decomposes at 90°C. Also at 150°C, AB neat evolves 2.5 equivalents of H_2 in 2 hrs while AB:nano-BN evolves 1.9 equivalents.

^{15}N labeled samples have been prepared using labeled ^{15}N AB and unlabelled nano-BN. These data are presented in Figure 52. The MS spectra are normalized to the amount of AB in each sample; the experiments were run under Ar with a heating ramp of 1 K/min from RT to 200°C. Only AB was ^{15}N labeled, the highest signal in the BZ (borazine) MS was always Mass 83. The BZ signal is always 2 orders of magnitude smaller than that of H_2. These data show that the BZ comes from the AB dehydrogenation and not from the nano-BN.

To elucidate the mechanism of dehydrogenation of AB on the surface of nano-BN ^{11}B MAS NMR data has been collected as a function of time at 80°C for the 1:1 AB-nano-BN and at 60°C for the 1:4 AB:nano-BN samples. The ^{11}B and ^{1}H MAS NMR data for the 1:1 AB:nano-BN is shown in Figure 53. The data are consistent with a small amount of diammonium diborane (DADB) present in the sample leading to removal of the usual induction period that AB needs. The presence of DADB in the sample is attributed to ball milling AB with nano-BN for 30 minutes.

The NMR spectrum obtained after 2 minutes at 80°C show that the amount of DADB increases and the signal for AB sharpens indicating a more rapid rotation of the AB molecules. After 5-8 mins, DADB and the AB peaks are the major peaks, similar to the dehydrogenation of neat AB. New peaks between -5 and -15 ppm corresponding to BH and BH_2 groups from polyaminoboranes (PAB, $(H_2NBH_2)_x$) begin to grow.

$$H_3NBH_3 \rightarrow (H_2NBH_2)_x + H_2,\ 90\text{-}120°C$$

After 30 minutes at 80°C in the NMR, the intensity of peaks associated with DADB and AB decreases, and the PAB resonances broaden. The NMR resonance for nano-BN at 30 ppm, remains unchanged during the dehydrogenation of AB, which suggest that nano-BN is only assisting the dehydrogenation of AB. However, that does not explain why there is more borazine or why the heat associated with hydrogen release from AB should be smaller when AB is present on the surface of nano-BN. To quantify the amount of borazine evolved from all of these materials, a trap system has been developed at PNNL that uses a circulation stainless steel vessel and a round bottom flask filled with an ether (typically 20 ml of THF or glyme were used). This is presented in Figure 54. The samples were heated under an Ar gas purged system and any volatile material is trapped by bubbling through an ether (glyme or tetrahydrofuran). An inert gas flow (3-30 ml/min) was passed through the AB samples loaded into a stainless steel vessel fitted with a gas inlet and outlet. The outlet was connected to a flask with a frit that contains an ether (glyme, tetrahydrofurane) cooled with dry ice. The vessel containing AB was heated in a tube furnace at various ramp rates or inserted into a pre-heated furnace at 150°C. In later experiments the setup was modified to include a stainless steel transfer line to replace the tygon tubing. This line was heated at ~60°C to ensure that all of the borazine is collected in the ether trap. The borazine was identified and quantified by ^{11}B NMR, using a standard solution of AB and in the later experiments borazine. The data obtained from these trapping experiments is summarized in Table 3. As can be seen from Table 3, the borazine yield increases with increasing the ramp rate and also increases with increasing the concentration of nano-BN. Interestingly, the amount of borazine while heating isothermally at 150°C seems to be relatively low for neat AB. At this temperature it is known from Figure 51 and burette data, that neat AB evolves 2.5 equivalents of hydrogen.

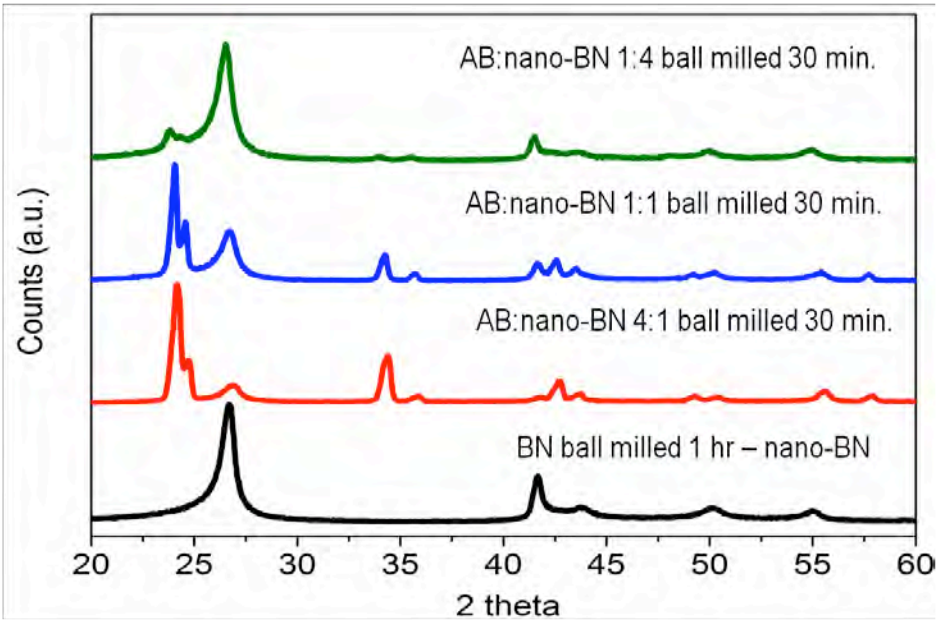

Figure 53. XRD data for nano-BN - black, AB:nano-BN 4:1 -red, AB:nano-BN 1:1 - blue, and AB:nano-BN 1:4 - green.

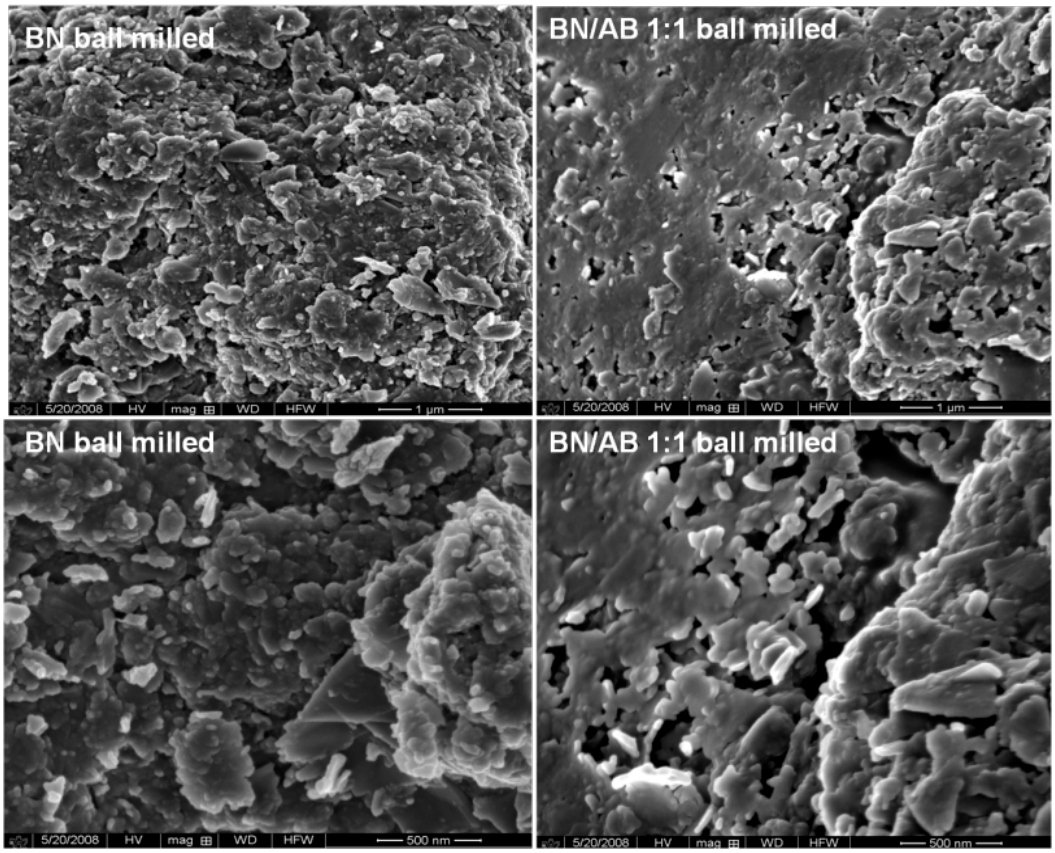

Figure 54. SEM data for nano-BN and AB:nano-BN 1:1.

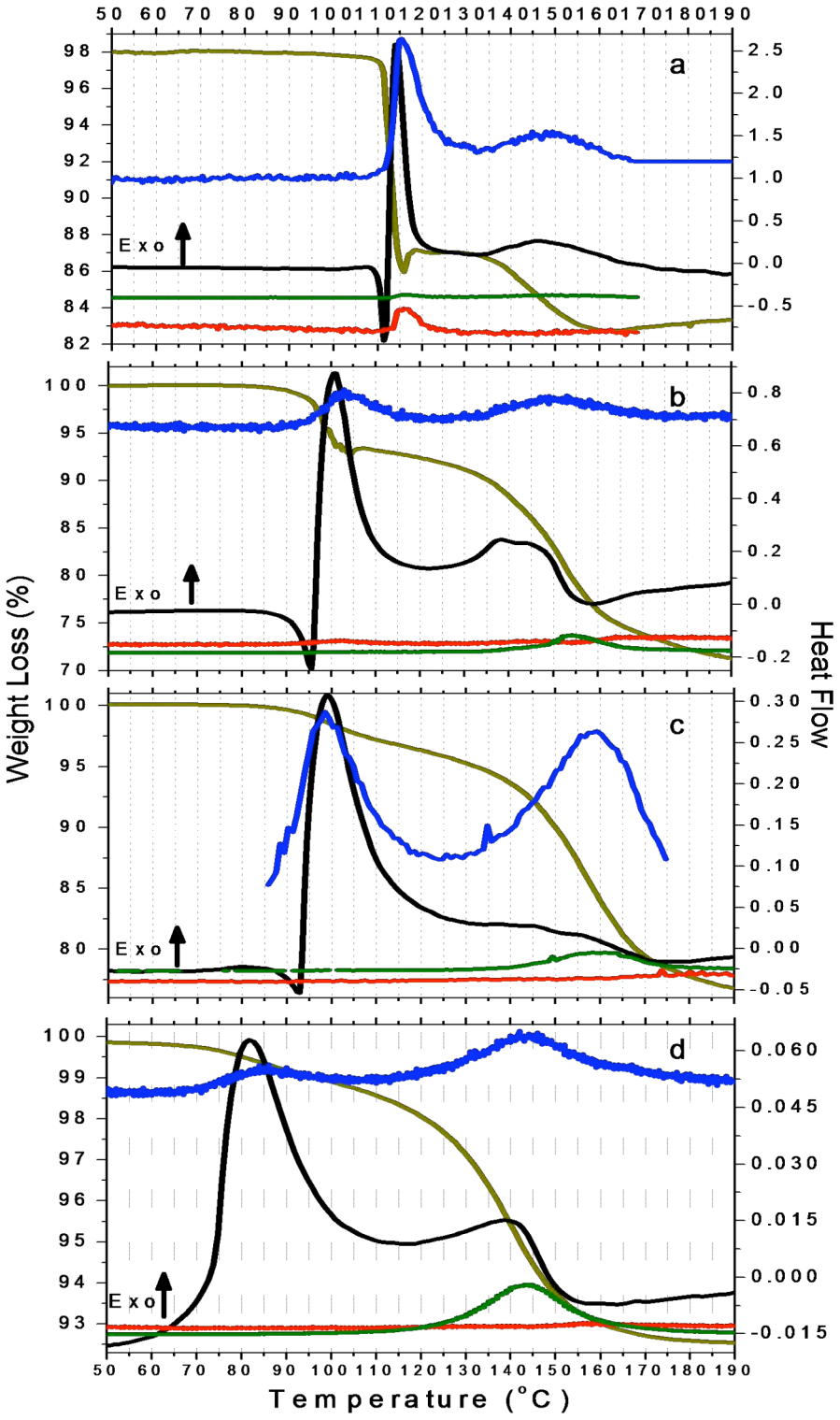

Figure 55. TGA/DSC/MS DATA for a) AB, b) AB:nano-BN 4:1, c) AB:nano-BN 1:1, d) AB:nano-BN 1:4. Olive (TGA), black (DSC), blue (MS hydrogen channel), green (MS borazine channel), red (MS ammonia channel).

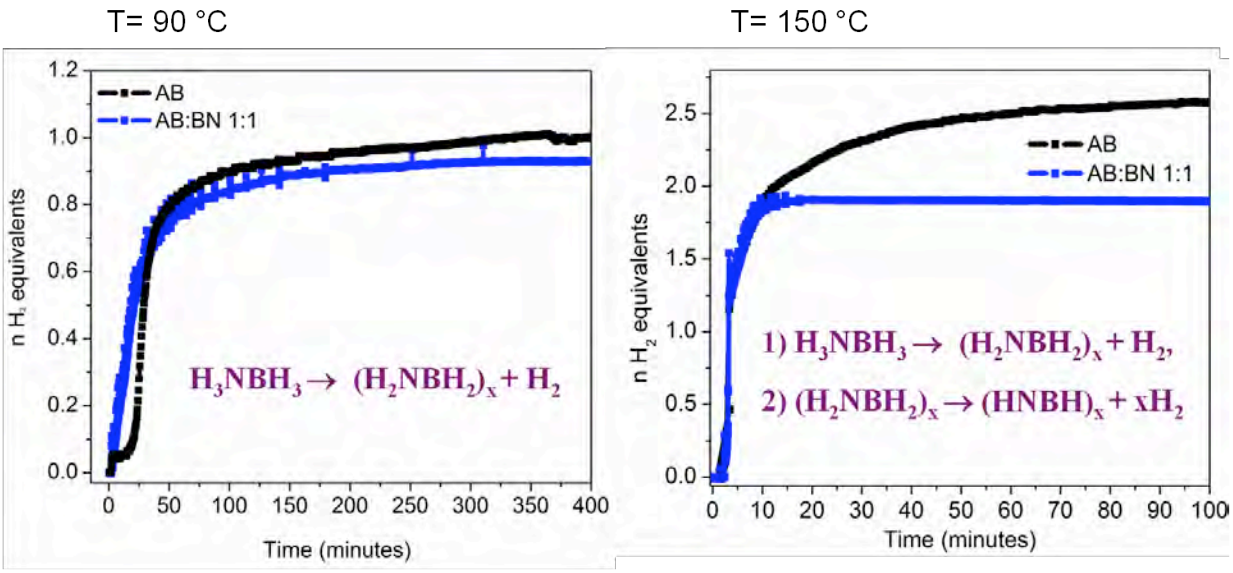

Figure 56. Volumetric gas burette data for AB and AB:nano-BN 1:1 at 90ºC and 150ºC.

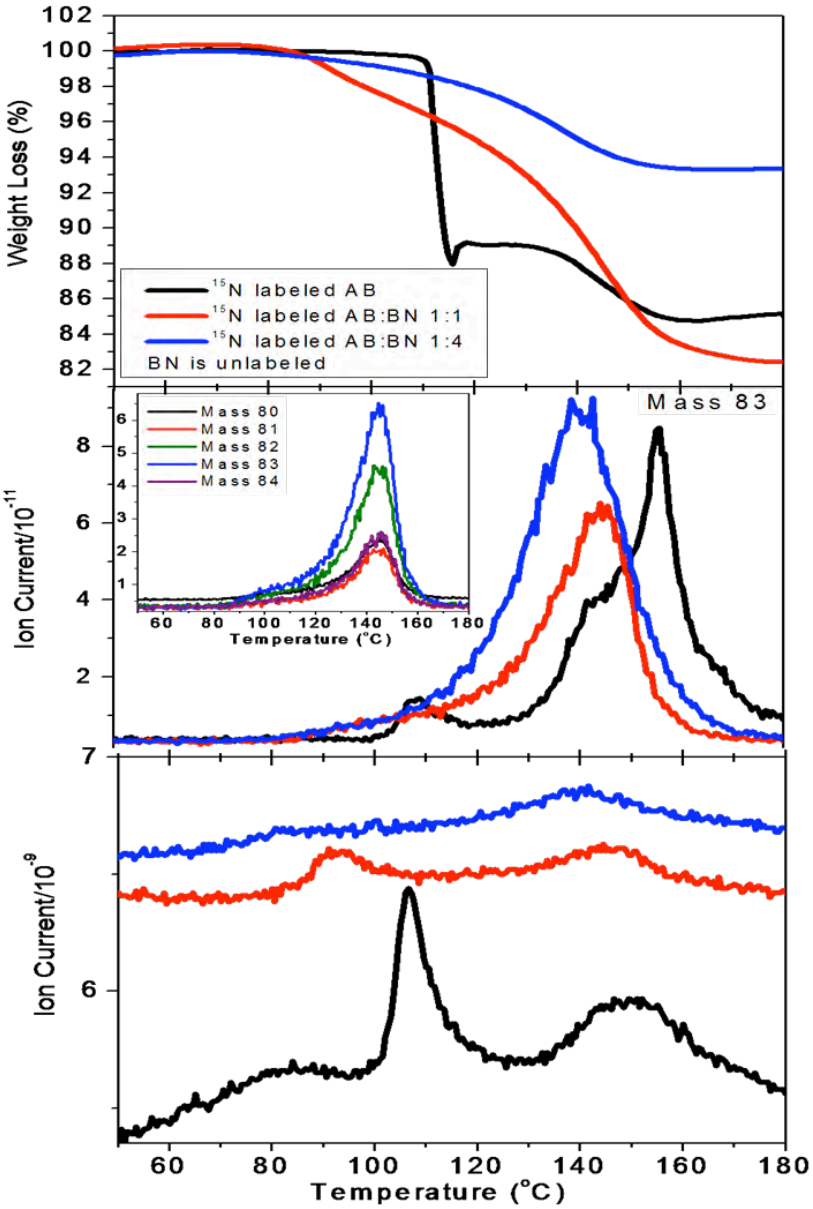

Figure 57. TGA/MS data for ^{15}N labeled AB (black), AB:nano-BN 1:1 (red), AB:nano-BN 1:4 (blue). Top - TGA data, middle - MS BZ channel, and bottom - MS hydrogen channel.

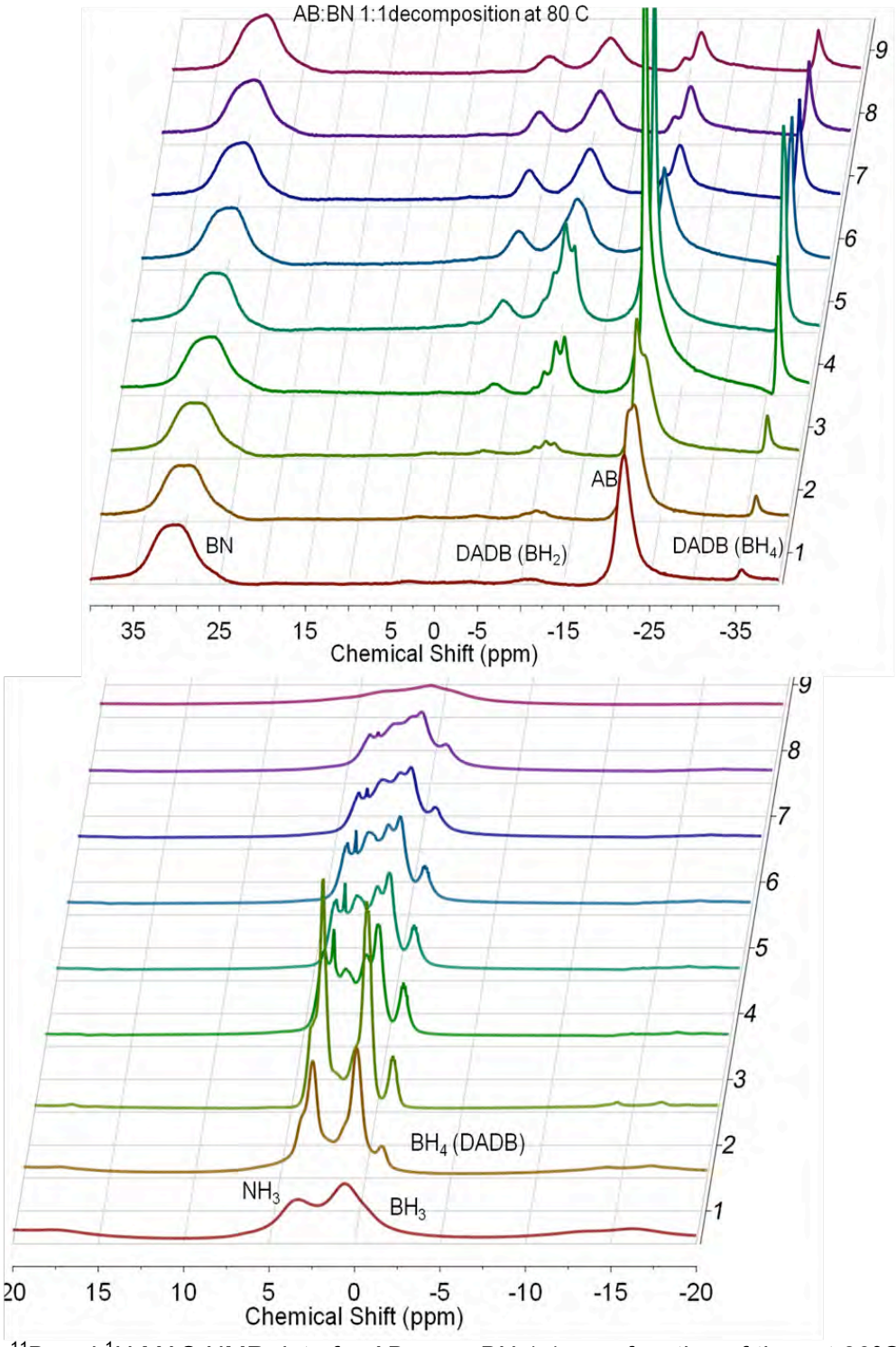

Figure 58. ^{11}B and ^{1}H MAS NMR data for AB:nano-BN 1:1 as a function of time at 80ºC. the first spectra in both cases is recorded at RT.

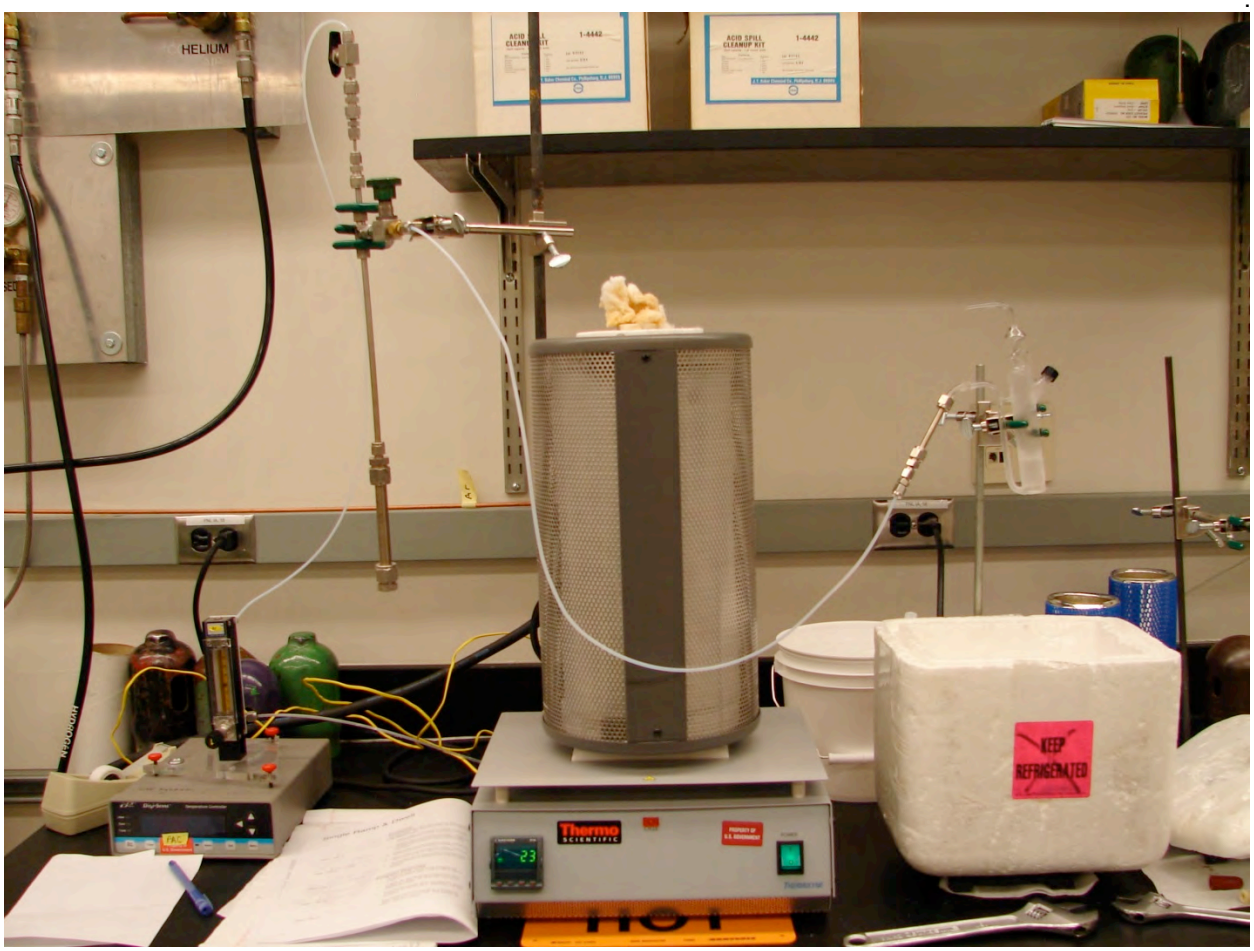

Figure 59. Experimental setup used for the trapping borazine measurements.

Table 3. Borazine trap - experimental results obtained under different heating conditions.

	Heating scheme	Wt. % BZ
AB	0.5°C/min 200°C	2.9±1.4
AB	1°C/min 200°C	4.7±1.9
AB	1°C/min 200°C	5.8
AB	150°C isothermal	1.2±0.7
AB:BN 1:1	0.5°C/min 200°C	7.5±1.8
AB/nano-BN 1:1	1°C/min 200°C	6.4±0.07
AB/nano-BN 1:4	1°C/min 200°C	12.7±1.2
AB/nano-BN 1:1	150°C isothermal	4.1±1.1
AB:graphite 1:4	1°C/min 200°C	0.4

References:

1. "Promotion of Hydrogen Release from Ammonia Borane with Mechanically Activated Hexagonal Boron Nitride", D. Neiner, A. Karkamkar, J. C. Linehan, B. Arey, T. Autrey, and S. M. Kauzlarich, *J. Phys. Chem. C*, *113* (3), 1098–1103, **2009.**

2. "Decomposition Pathway of Ammonia Borane on the Surface of Nano-BN", Doinita Neiner, Avery Luedtke, Abhijeet Karkamkar, Wendy Shaw, Jialing Wang, Nigel D. Browning, Tom Autrey and Susan M. Kauzlarich, *J. Phys. Chem. C*, **2010**, *114* (32), pp 13935–13941.

Other additives have also been used, such as mesoporous C, Si and Si alloyed with C nanoparticles as well as silica, MCM-41. Some of them are summarized in figures 60, 61 and 62.

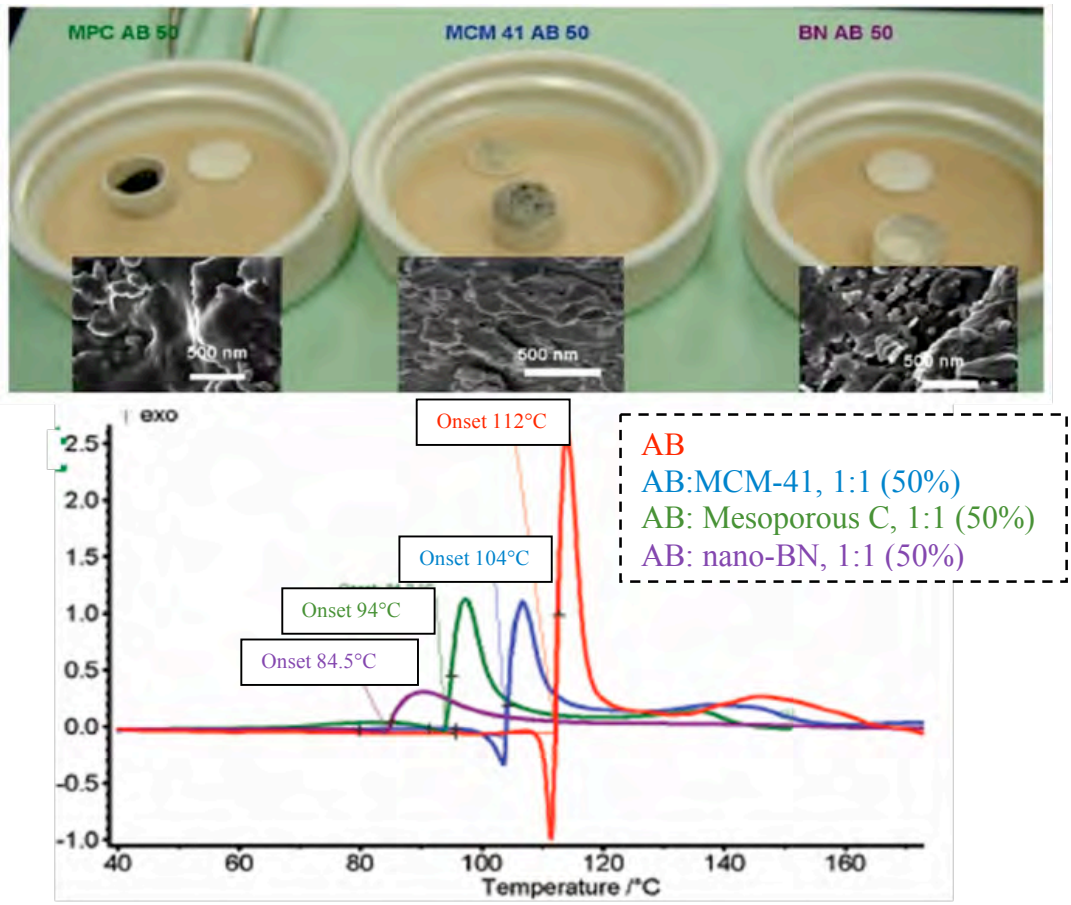

Figure 60. DSC/SEM and images for the AB mixed with mesoporous C, MCM 41 and BN in a 1:1 by weight ratio. For comparison AB neat DSC trace is also shown.

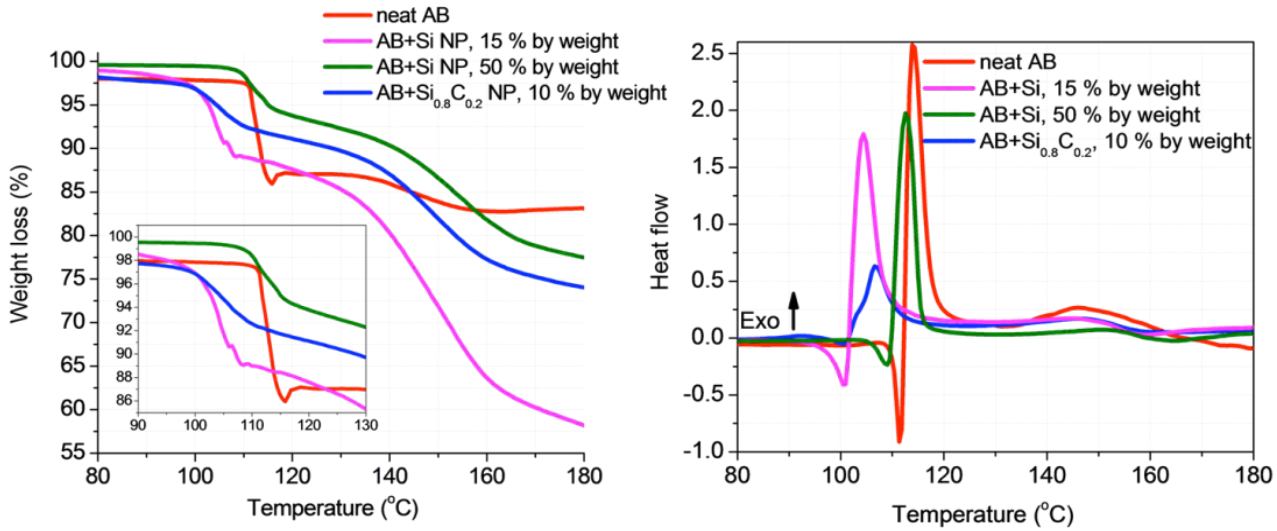

Figure 61. TG/DSC data for AB, AB mixed with Si NP, Si doped with C nanoparticles.

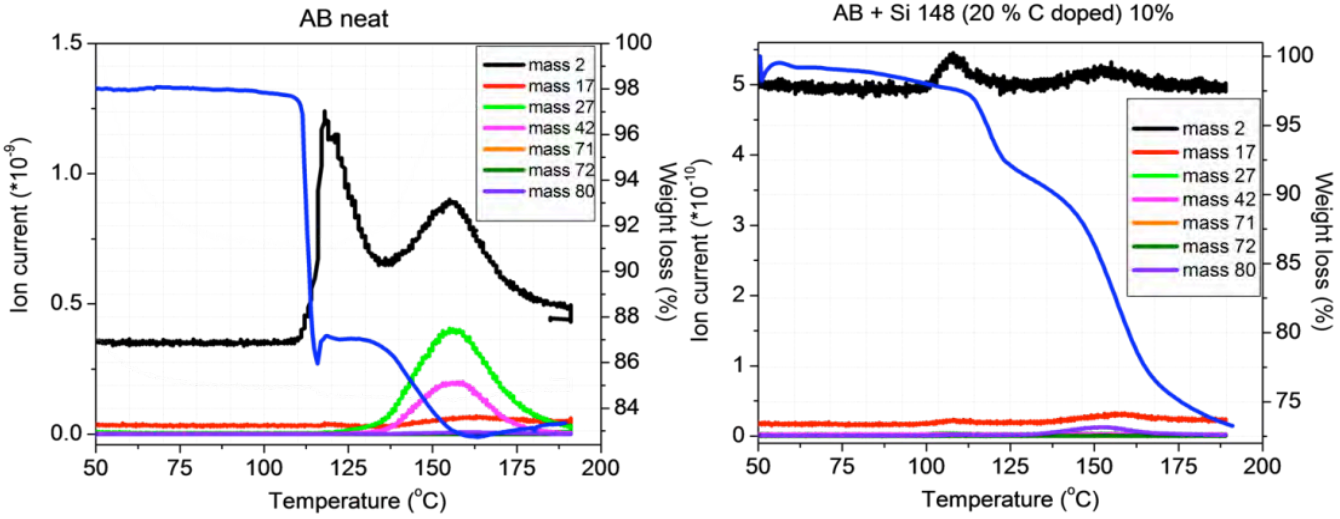

Figure 62. TG/DSC/MS data for AB neat and AB mixed with 10% $Si_{0.8}C_{0.2}$)H nanoparticles.

IV. MOLECULAR COMPOUNDS AS HYDROGEN STORAGE MATERIALS

Objectives

The major objectives of work in this area concerned the synthesis and testing of molecular derivatives of the lighter main group elements, e.g. boron, aluminum, silicon or phosphorus, for reversible reactivity with hydrogen. The initial focus of our work was on boron-phosphorus molecular species.

Approach

We synthesized a number of unsaturated boron-phosphorus molecules (i.e. the boron and phosphorus atoms are two or three coordinate) and tested the reactivity of hydrogen with these compounds and with other unsaturated boron phosphorus molecules that were known from previous work in our laboratory. Initially we synthesized monomeric phosphino-boranes of the general formula Ar(H)PB(Br)(tmp) (Ar = $Ar^{\#}$, C_6H_3-2,6(C_6H_2-2,4,6-Me_3)$_2$; C_6H_3-2,6(C_6H_3-2,6-Pr^i_2)$_2$ or $Ar^{\#}C_6H_3$-2,6(C_6H_2-2,4,6-Pr^i_3)$_2$; tmp = 2,2,6,6-tetramethylpiperidinyl) via the reaction of LiP(H)Ar with BBr_2(tmp). An example of a structurally characterized compound is given in Figure 55.

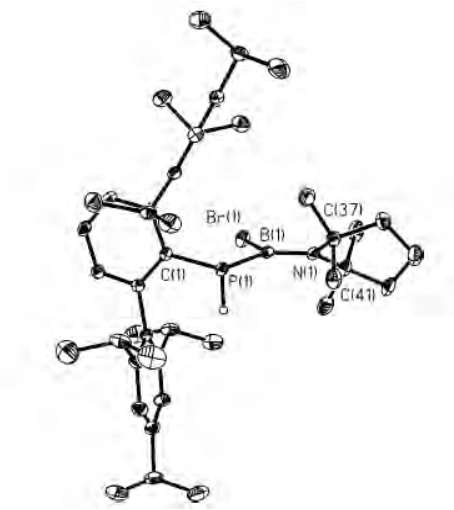

Figure 63. Molecular structure of an Ar(H)PB(Br)(tmp) molecule with thermal ellipsoids at the 30% probability level. All carbon-bound hydrogen atoms are not shown for clarity. Selected bond lengths (Å) and angles (deg) bracketed values belonging to a second molecule in the asymmetric unit: P(1)-B(1) 1.958(3) [1.950(3)], P(1)-C(1) 1.839(2) [1.839(2)], P(1)H(1) 1.29(2) [1.30(2)], B(1)-N(1) 1.390(3) [1.389(3)]; C(1)-P(1)-B(1) 106.93(11) [107.52(11)], C(1)-P(1)-H(1) 98.2(9) [98.6(11)], P(1)-B(1)N(1) 122.31(18) [122.78(18)], P(1)-B(1)-Br(1) 115.17(14) [114.79(14)], Br(1)-B(1)-N(1) 122.23(18) 122.26(19)], B(1)-N(1)-C(37) 119.6(2) [119.80(19)], B(1)-N(1)-C(41) 122.8(2) [122.7(2)].

In this molecule both the boron and phosphorus atoms are three coordinate and have the potential to react with H_2 to form a phosphine borane donor-acceptor complex of the type $Ar(H)_2PB(H)(Br)(tmp)$. However, testing of these molecules and several other unsaturated boron-phosphorus species including Mes_2BPPh_2, $Mes_2BP(H)$(1-Ad) (1-Ad = 1-adamantanyl), $PhP(BMes_2)_2$ and $MesB(PPh_2)_2$ (Mes = C_6H_2-2,4,6-Me_3), which had been earlier synthesized by

our group in the 1980s and 1990s, disclosed no reactions with hydrogen at 25°C and 1 atmosphere pressure.

The next phase of our investigation involved the synthesis of a more unsaturated boron-phosphorus molecule and investigate its reactivity toward hydrogen. The obvious choice was to synthesize and test the reactivity of boranylidenephosphanes, i.e. compounds of the general formula RB= PR′ (R and R′ = alkyl or aryl group) in which the boron phosphorus atoms are two coordinate. Unfortunately, stable compounds of this formula could not be synthesized and this class of species remain unknown currently. This is more than likely due to the fact that, owing to the availability of weakly bonding electron density, and hence Lewis base character at phosphorus, the dimerization of the parent species to give compounds of formula $(RBPR')_2$ is facile and has been estimated to be exothermic by over 50 kcal mol^{-1}. To deal with this issue we approached the synthesis of a monomeric species with B=P multiple bond character by binding a Lewis base donor molecule to the empty p-orbital at boron within the RB= PR′ unit. With this method dimerization is prevented but two-coordination at phosphorus is maintained. Accordingly treatment of Ar*(H)PnB(BR)(tmp) (Pn = P or As) with p-dimethylaminopyridine (dmap) in accordance with Scheme 1.

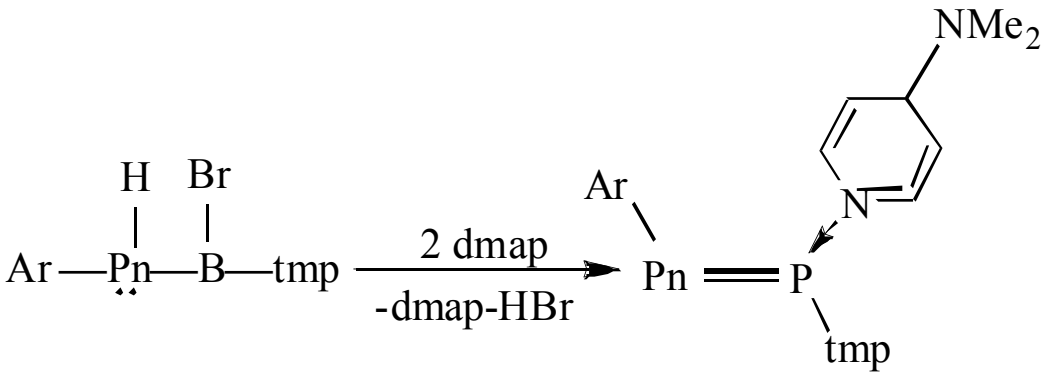

Scheme 1. Reaction of Ar(H)PnB(Br)(tmp) (Pn = P or As) with dmap to afford ArPnB(tmp)(dmap).

The products were characterized by multinuclear NMR spectroscopy and single crystal X-ray crystallography. The structure of the phosphorus derivative is shown in Figure 56. The B-P bond length (1.809(2) Å) showed that it was a double bond. However, treatment of this compound with hydrogen at room temperature and 1 atmosphere pressure revealed that there was no reaction under these conditions.

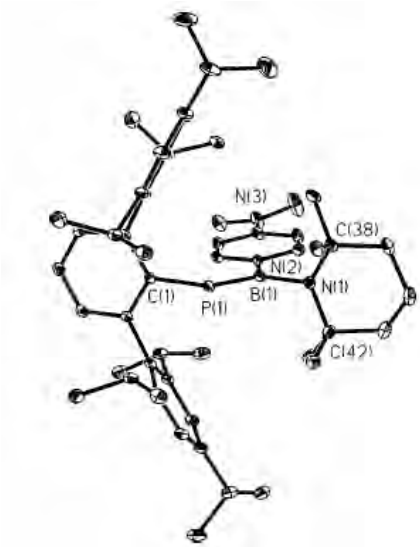

Figure 64. Molecular structure of Ar*PB(tmp)(dmap) with thermal ellipsoids at the 30% probability level. Selected bond lengths (Å) and angles (deg) with values corresponding to the disordered dmap are in brackets: P(1)-B(1) 1.8092(17), P(1)-C(1) 1.8509(14), B(1)-N(1) 1.4837(19), B(1)-N(2) 1.593(2) [1.548(2)]; C(1)-P(1)-B(1) 114.36(7), P(1)-B(1)-N(1) 119.48(11), P(1)-B(1)-N(2) 127.41(13) [132.7(4)], N(1)-B(1)-N(2) 113.09 (14) [107.8(4)], B(1)-N(1)-C(38) 117.98(12), B(1)-N(3)-C(42) 117.84(12), C(38)-N(1)-C(42) 119.16(11).

A similar reaction sequence involving the treatment of the boron amido species Ar$^{\#}$(H)NB(Br)tmp with dmap resulted in dehydrobromination but a dmap complex was not formed. Instead the uncomplexed iminoborane Ar$^{\#}$-N≡B-tmp was obtained. Its structure is shown in Figure 57.

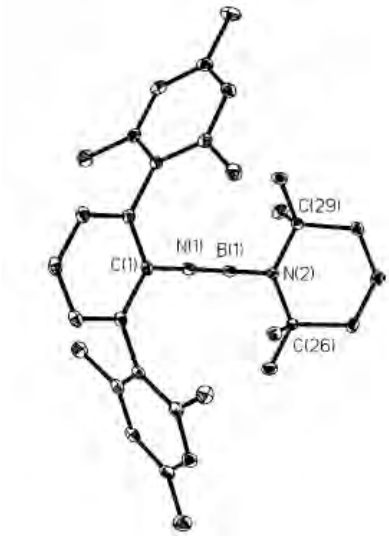

Figure 65. Molecular structures of Ar$^{\#}$-N≡B-tmp with thermal ellipsoids are presented at the 30% probability level. Hydrogen atoms are not shown for clarity. Selected bond lengths (Å) and angles (deg): N(1)-B(1) 1.254(3). C(1)N(1) 1.366(2), B(1)-N(2) 1.374(3), N(2)-C(26) 1.491(2), N(2)-C(29) 1.496(2); C(1)-N(1)-B(1) 171.7(2), N(1)-B(1)-N(2) 179.4(2), B(1)N(2)-C(26) 119.99(16), B(1)-N(2)-C(29) 119.42(17), C(26)-N(2)C(29) 120.59(14).

This compound features a very short B-N length of 1.254(3) Å indicating that a B-N triple bond had formed. Both the nitrogen (N(1)) and boron atoms are two coordinate. However, the compound was unreactive toward hydrogen under ambient conditions.
In addition to the molecules discussed above we attempted reactions with hydrogen with disilene $Mes_2SiSiMes_2$ (Mes = C_6H_2-2,4,6-Me_3) and the diphosphene (Mes*PPMes* (Mes* = C_6H_2-2,4,6-Bu^t_3) but no reactions were observed. In related work in the laboratory we demonstrated that hydrogen reacts directly at 25°C/1 atmosphere with a variety of unsaturated gallium, germanium and tin compounds but that these reactions were irreversible. Furthermore, the use of these heavier element compounds for hydrogen storage was deemed unsuitable because of their high molecular weight, expense and possible toxicity. Parallel work elsewhere in the center, mainly at LANL, PNNL, Universities of Alabama, Pennsylvania and Washington had indicated that amine borane ($H_3N{\cdot}BH_3$, AB) was likely to have the best prospect for success as a hydrogen carrier and we turned our attention to this topic in the second phase of our work.

V. REGENERATION OF AB USING MOLECULAR COMPUNDS

Efficient Amine-Borane Regeneration Cycles using metal formates

Objective

The development of a route to regenerate spent fuel from aminoborane dehydration by the use of formate derivatives.

Introduction

The second phase of the project began in March 2007. It was focused on the development of efficient routes for the regeneration of amine borane (AB, $H_3N{\cdot}BH_3$) which had been identified by other groups within the center as the fuel/H_2 carrier most likely to meet the goals set by DOE. This species offered the advantages of a high hydrogen content (19.6%) and the relative ease of synthesis and the prospect of catalytic release of hydrogen at low temperature at a rate sufficient for practical use. Arguably the major difficulty in the use of AB was the regeneration of the spent fuel - a polymeric BN species - which remained after the hydrogen from AB was released. The original proposal for the regeneration scheme studied at UC Davis was by D. Thorn of LANL. This regeneration scheme involved the use of metal formates, some of which could be thermally decomposed under mild conditions to eliminate CO_2 and form a metal hydride. The latter could then be used as a reductant for the BX_3 (obtained from the digestion of the spent "BN" fuel) to afford BH_3 together with an M-X moiety. The M-X species would then be reconverted to the metal formates by treatment with formic acid obtained industrially either as a byproduct of acetic acid synthesis or by hydrogenation of carbon dioxide. This regeneration pathway is summarized on the right-hand side of Scheme 2 the position of the regeneration route in the AB fuel cycle is illustrated on the left-hand side of the same scheme.

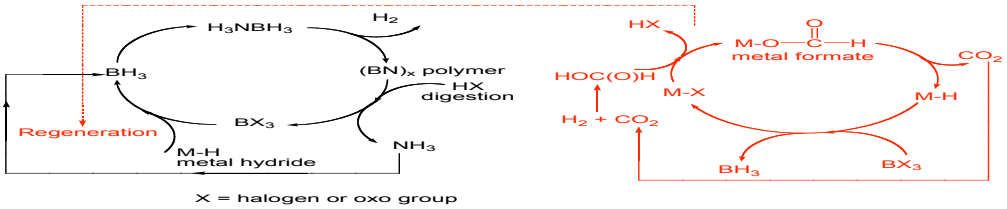

Simplified LANL Cycle for H_2 Storage Formate/

Simplified UC Davis Hydride Regeneration Cycle

Scheme 2. Schematic illustration of the AB regeneration cycle (left) and the metal formate route to regenerate the metal hydride reductant (right). The reductant converts the BX_3 from digested "BN" to BH_3.

Our main objective was to develop efficient synthetic routes to these metal formates and investigate their thermolysis to produce the metal hydride. Thermolysis of metal formates can proceed by two pathways as shown in Scheme 3.

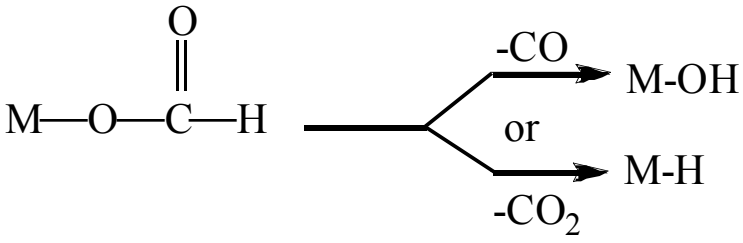

Scheme 3. Thermolysis of a metal formate to give either CO or CO_2 elimination to generate either M-OH or M-H moieties.

The majority of metal formates thermally decompose with CO elimination and formation of an M-OH moiety. Our objective was to discover metal formates that decomposed to the metal hydride with CO_2 elimination under relatively mild heating (<200°C), i.e. the lower pathway in Scheme 3. This pathway has the further advantage that the released CO_2 could be used to regenerate formate. Our immediate objective therefore was to investigate the synthesis of several element derivatives of formates and subsequently study their thermolysis behavior. The first reactions examined are summarized in Scheme 4.

$$R_nEH_m + m\,HCOOH \longrightarrow R_nE\text{-}(O\text{-}C(O)H)_m + m\,H_2$$

$$R_nE(NR'_2)_m + m\,HCOOH \longrightarrow R_nE\text{-}(O\text{-}C(O)H)_m + M\,NHR'_2$$

(E = B, Al, Ga or Sn; R = Ph, Mes, C_6H_3-2,6-Pr^i_2 (Dipp), C_6H_2-2,4,6-Pr^i_3 (Tripp); R' = H, Me)

Scheme 4. Synthesis of formate derivatives by treatment of hydrides or amides with formic acid.

We began our investigations by attempting the synthesis of boron formates. Calculations by D. Camaioni of PNNL indicated that some boron formates could eliminate CO to afford the corresponding hydride but the elimination of CO_2 was only slightly less favorable. We tested synthetic approaches that involve the reaction of boron hydrides or amides with formic acid. To our surprise the borylamide afforded very poor yields of the formate upon treatment with formic acid (Scheme 5). In addition the reaction of formic acid with the borane Mes_2BH (Mes = C_6H_2-2,4,6-Me_3) did not yield $Mes_2BOC(O)H$. Instead the oxo-bridged dimer $Mes_2B\text{-}O\text{-}BMes_2$ was isolated. One explanation for the observation is that the formate is generated initially but this readily eliminates CO_2 to form the B-OH unit which can then react with and equivalents of the boron hydride to give the oxo-bridged dimer (Scheme 5).

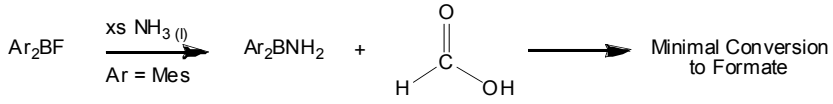

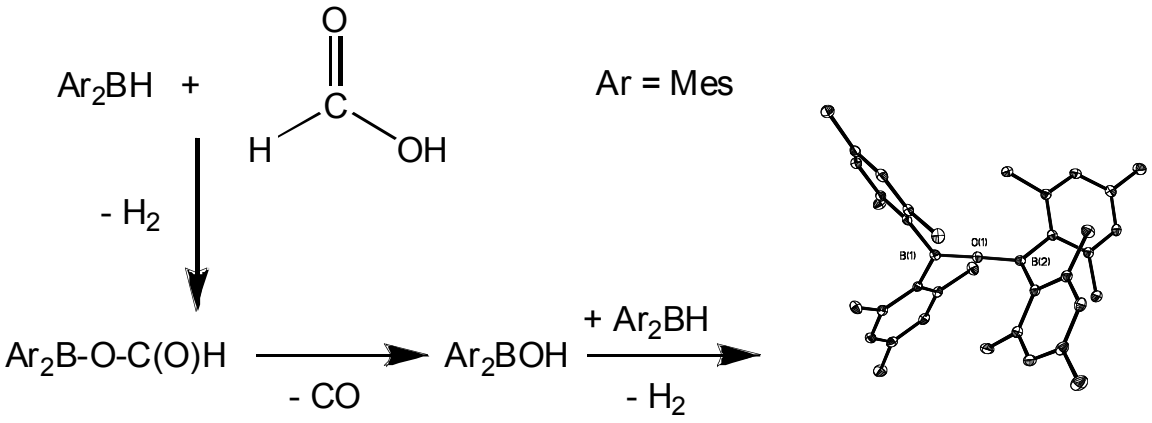

Scheme 5. Reaction of Ar_2BNH_2 (Ar = mesityl) or Ar_2BH with formic acid.

Parallel work in the laboratory on the synthesis of tin formates was more successful. We focused on tin formates because earlier work by Rathke and coworkers (*Organometallics*, **1985**, *4*, 1893) had shown that $Bu^n_3SnOC(O)H$ eliminated CO_2 under mild conditions to give Bu^n_3SnH. In addition computational work at LANL (J. C. Gordon, B. L. Davis, A. D. Sutton, K. X. Bhattacharyya) Had indicated that CO_2 elimination was also favored in tin diformates as shown in Scheme 6.

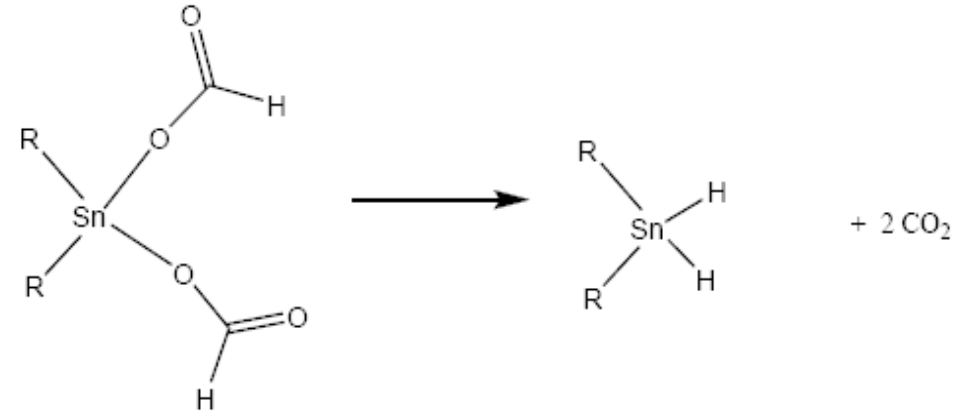

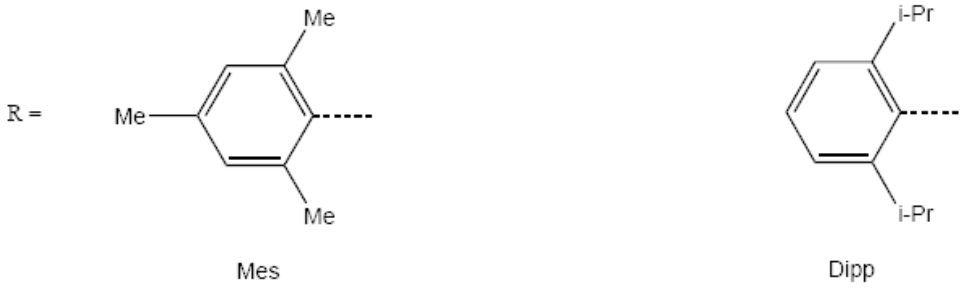

R	Δ*H* (0 K)	Δ*H* (298 K)	Δ*G* (298 K)
Mes	17.9	18.2	-2.4

Dipp	16.8	17.2	-5.7

B3LYP/DZVP2 and cc-pVDZ-PP (ECP) for Sn

Scheme 6. Calculations on tin diformates showed that CO_2 release was energetically favored with hydride regeneration.

We found that the treatment of $Bu^n_2SnH_2$ with two equivalents of formic acid at room temperature in diethyl ether afforded the diformate $Bu^n_2Sn(OC(O)H)_2$ in 72% yield.

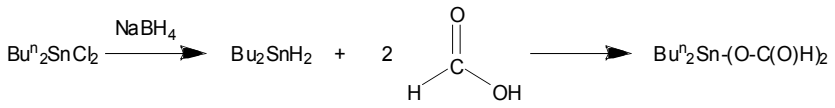

Scheme 7. Synthesis of $Bu^n_2Sn\{OC(O)H\}_2$.

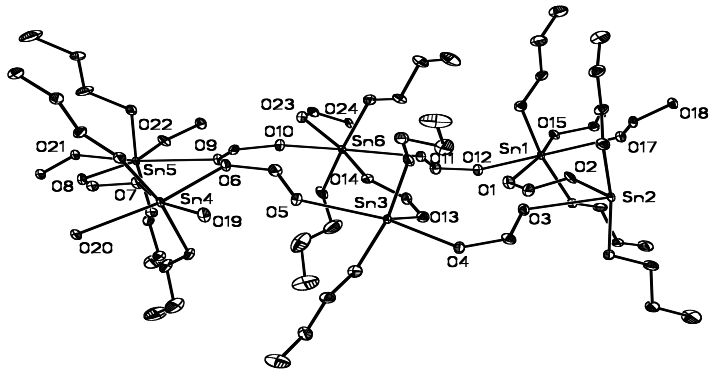

Figure 66. Illustration of the sheet strcuture of $Bu^n_2Sn\{OC(O)H\}_2$ in the solid state. Hydrogen atoms are not shown.

However, thermolysis of this diformate in high boiling solvents such as diglyme or mesitylene did not result in CO_2 elimination and unreacted $Bu^n_2Sn\{OC(O)H\}_2$ could be recovered quantitatively. Heating the solid to higher temperatures, *ca* 200°C, resulted in sublimation without decomposition.

We reasoned that the lack of CO_2 elimination might be due to the associated structure of $Bu^n_2Sn\{OC(O)H\}_2$ in which the six-coordination of the tin atoms could interfere with an intra molecular elimination pathway. To reduce the coordination number at tin the more sterically crowded bulkier benzyl or cyclohexyl derivatives $Bz_3SnOC(O)H$ or $Cy_3SnOC(O)H$ were synthesized by treatment of their respective hydroxides with formic acid. The structures of these compounds are illustrated in Figure 59 which shows that they have a one-dimensional polymeric structure with five (rather than six) coordinate tins.

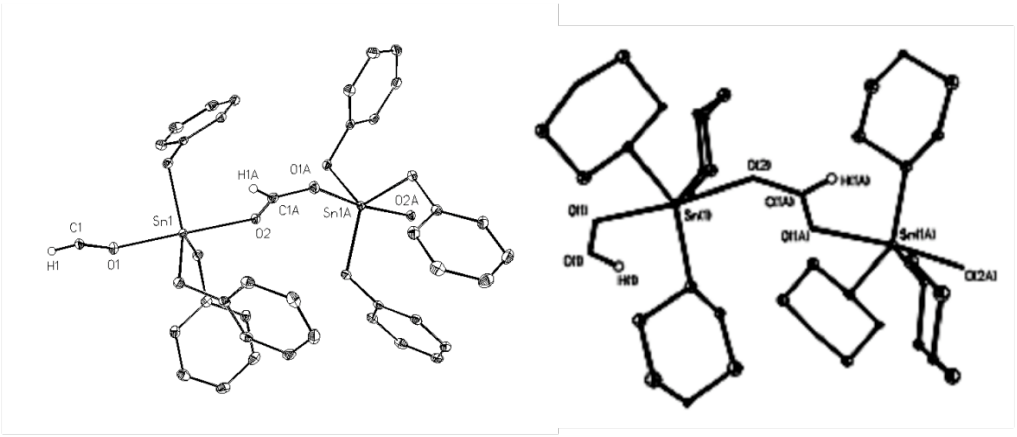

Figure 67. . Illustrations of the structure of $\{(PhCH_2)_3SnOC(O)H\}_n$ (left) and $\{Cy_3SnOC(O)H\}_n$ (right). Hydrogen atoms (except formate hydrogen) are not shown.

The attempted conversion of these compounds to the corresponding hydrides showed that the benzyl derivative was unchanged upon refluxing in mesitylene for 24h whereas the tri-cyclohexyl formate decomposed to an insoluble orange solid upon refluxing in diglyme or decalin for 8h.

Use of the bulkier substituents C_6H_3-2,6-Me_2(Dmp) or C_6H_2-2,4,6-Me_3(Mes) led to the first examples of monomeric structures for molecular tin formates as illustrated in Figure 60.

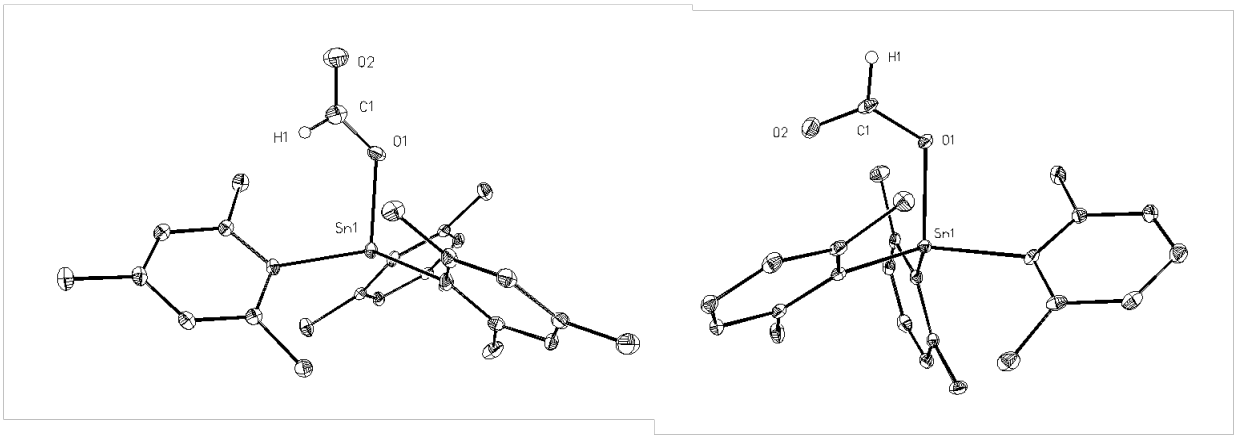

Figure 68. Structures of $Mes_3SnOC(O)H$ (left) and of $Dmp_3SnOC(O)H$) (right). Hydrogen atoms (except formate hydrogen) are not shown.

Refluxing $Mes_3SnOC(O)H$ in mesitylene for 24h did not result in CO or CO_2 elimination. However, refluxing $Mes_3SnOC(O)H$ in decalin for 8h resulted in a mixture of $Mes_3SnOC(O)H$ and Mes_3SnOH indicating that CO rather than CO_2 was eliminated. Analogous experiments with $Dmp_3SnOC(O)H$ also afforded a mixture to $Dmp_3SnOC(O)H$ and DmpSnOH indicating CO elimination.

The investigation was switched to the use of $Bu^n{}_3SnOC(O)H$ as a regeneration agent which had already been shown to decompose with CO_2 elimination to give $Bu^n{}_3SnH$. We

developed a high-yielding synthetic route beginning with commercially available Bu^n_3SnCl as shown in Scheme 8.

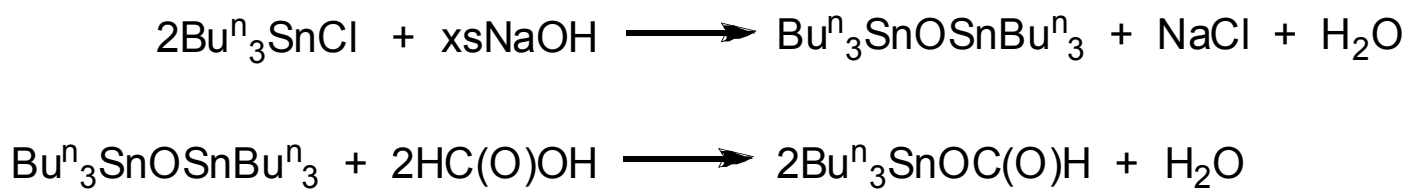

Scheme 8. Synthesis of $Bu^n_3SnOC(O)H$ from commercially available Bu^n_3SnCl.

Unfortunately the first step - the conversion of Bu^n_3SnCl to $Bu^n_3SnOSnBu^n_3$ - proceeds only in moderate yield. However, we could show that it was possible to generate $Bu^n_3SnOC(O)H$ in almost quantitative yield in just one step by treatment with ammonium or triethylammonium formate as shown in Scheme 9.

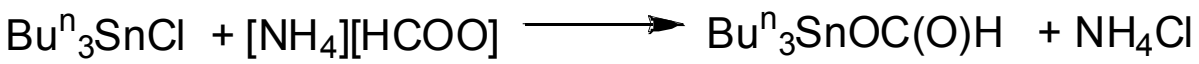

Scheme 9. One step conversion of Bu^n_3SnCl to $Bu^n_3SnOC(O)H$.

Extensive investigations of the conversion of $Bu^n_3SnOC(O)H$ to Bu^n_3SnH showed that this is best accomplished via distillation of the $Bu^n_3OC(O)H$ through a Vigreux column >12" long under reduced pressure. Yields of *ca* 70% of Bu^n_3SnH were obtained by this method. In a collaborative effort with J. Gordon, A. Sutton and coworkers at LANL it was shown that when polyborazylene (the spent fuel from the dehydrogenation of AB) is digested with ortho-benzenedithiol to give $[NH_4][BC_6H_4S_2\}$ (**1**) or $(C_6H_4S_2)BH{\cdot}NH_3$ (**2**), which **1** can be converted to tin thiolate derivatives **3** and **4** Bu^n_3SnH Bu^n_2SnCl and $C_6H_4(SH)_2$ can be released upon reaction with HCl (Scheme 9). The Bu^n_2SnCl can then be converted to $Bu^n_3SnOC(O)H$ and hence Bu^n_3SnH by the methods discussed above.

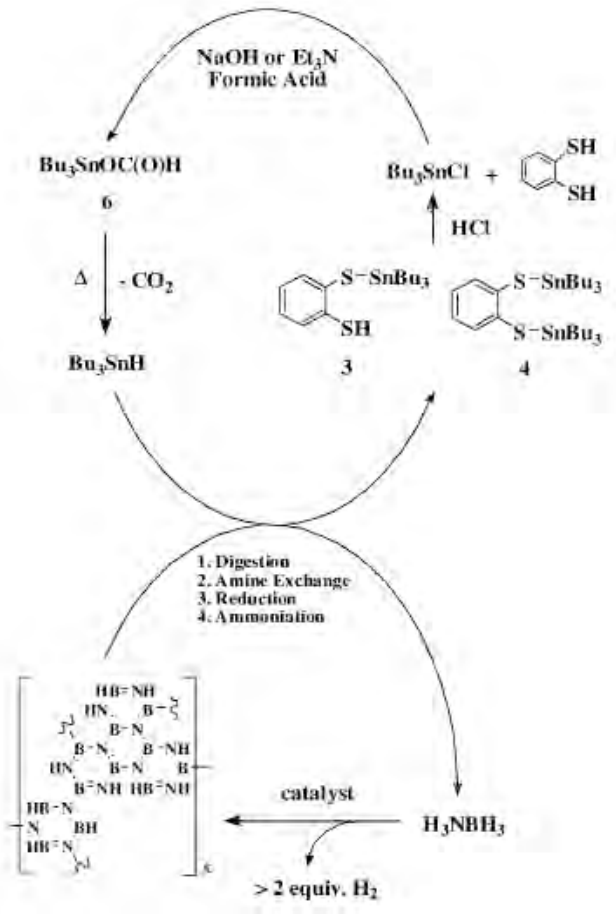

Scheme 9. Regeneration of AB with tin recycle and ortho-benzenedithiol recovery.

References:

1. “A Donor-Stabilization Strategy for The Preparation of Compounds Featuring P=B and As=B Double Bonds”, E. Rivard, W. A. Merrill, J. C. Fettinger and P. P. Power. Chemical Communications, 2006, 3800-3802.

2. “Boron-Pnictogen Multiple Bonds: Donor-stabilized P=B and As=B Double Bonds and a Hindered Iminoborane with a B-N Triple Bond”, E. Rivard, A. Merrill, J. C. Fettinger, R. Wolf, G. H. Spikes and P. P. Power. Inorganic Chemistry, 2007**,** ***46***, 2971-2978.

3. “Synthesis and Thermolytic Behavior of Tin(IV) Formates: In Search of Recyclable Metal-Hydride Systems”, B. D. Ellis, T. M. Atkins, Y. Peng, A. D. Sutton, J. C. Gordon and P. P. Power. Dalton Transactions, in press.

VI. PUBLICATIONS

1. “A Donor-Stabilization Strategy for The Preparation of Compounds Featuring P=B and As=B Double Bonds”, E. Rivard, W. A. Merrill, J. C. Fettinger and P. P. Power. Chemical Communications, 2006, 3800-3802.

2. “Boron-Pnictogen Multiple Bonds: Donor-stabilized P=B and As=B Double Bonds and a Hindered Iminoborane with a B-N Triple Bond”, E. Rivard, A. Merrill, J. C. Fettinger, R. Wolf, G. H. Spikes and P. P. Power. Inorganic Chemistry, 2007, 46, 2971-2978.

3. “Synthesis and Thermolytic Behavior of Tin(IV) Formates: In Search of Recyclable Metal-Hydride Systems”, B. D. Ellis, T. M. Atkins, Y. Peng, A. D. Sutton, J. C. Gordon and P. P. Power. Dalton Transactions, in press

4. "Room Temperature Synthesis of Surface-Functionalised Boron Nanoparticles", Pickering, Alexandra L., Mitterbauer, Christoph, Browning, Nigel D., Kauzlarich, Susan M., Philip, Philip P., Chemical Communications, 2007, 580.

5. "Synthesis and Characterization of $K_{8-x}(H_2)ySi_{46}$" D. Neiner, N. L. Okamoto, P. Yu, et al., Inorg. Chem., 49 (3), 815-822, 2010.

6. “Decomposition Pathway of Ammonia Borane on the Surface of Nano-BN”, Doinita Neiner, Avery Luedtke, Abhijeet Karkamkar, Wendy Shaw, Jialing Wang, Nigel D. Browning, Tom Autrey and Susan M. Kauzlarich, J. Phys. Chem. C, 2010, 114 (32), pp 13935–13941

7. "Hydrogen-Capped Silicon Nanoparticles as a Potential Hydrogen Storage Material: Synthesis, Characterization, and Hydrogen Release", D. Neiner, S. M. Kauzlarich, Chem. Mater., 22(2), 487-493, 2010.

8. “A Versatile Low Temperature Synthetic Route to the Zintl Phase Precursors: Na_4Si_4, Na_4Ge_4 and K_4Ge_4 as Examples”, M. Xuchu, X. Fen, T. Atkins, A. Goforth, D. Neiner, A. Navrotsky, and S. M. Kauzlarich, Dalton. Trans., 46, 10250, 2009.

9. “Promotion of Hydrogen Release from Ammonia Borane with Mechanically Activated Hexagonal Boron Nitride”, D. Neiner, A. Karkamkar, J. C. Linehan, B. Arey, T. Autrey, and S. M. Kauzlarich, J. Phys. Chem. C, 113 (3), 1098–1103, 2009.

10. “Hydrogen Encapsulation in a Silicon Clathrate Type-I Structure: $Na_{5.5}(H_{2.})_{2.15}Si_{46}$: Synthesis and Characterization”, D. Neiner, N. L. Okamoto, C. L. Condron, Q. M. Ramasse, P. Yu, N. D. Browning and S. M. Kauzlarich, J. Am. Chem. Soc., 129 (45), 13857 -13862, 2007.

11. “Characterization of hydrogen encapsulated type I silicon clathrate”, N. L. Okamoto, D. Neiner, C. L. Condron, Q. M. Ramasse, P. Yu, N. D. Browning and S. M. Kauzlarich, Microsc. Microanal. 13 (Suppl. 2), 2007.

12. "A new solution route to hydrogen-terminated silicon nanoparticles: synthesis, functionalization and water stability", X. Zhang, D. Neiner, S. Wang, A. Y. Louie, S. M. Kauzlarich, Nanotechnology , 2007, 18(9), 095601/1-095601/6.

13. "Fabrication of silicon-based nanoparticles for biological imaging" Proceedings of SPIE-The International Society for Optical Engineering, X. Zhang, D. Neiner, S. Wang, A. Y. Louie, S. M. Kauzlarich, 2007, 6448, Colloidal Quantum Dots for Biomedical Applications II, 644804/1-644804/8.

14. "Low-Temperature Solution Route to Macroscopic Amounts of Hydrogen Terminated Silicon Nanoparticles", D. Neiner, H. W. Chiu, S. M. Kauzlarich, J. Am. Chem. Soc., 2006, 128(34), 11016-11017.

15. "Investigation of nanocrystalline silicon as a possible hydrogen storage material", D. Neiner, H. W. Chiu, M. Blessent, S. M. Kauzlarich, 2006, Preprints of Symposia - American Chemical Society, Division of Fuel Chemistry, 51(2), 451.

16. "A Donor-Stabilization Strategy for The Preparation of Compounds Featuring P=B and As=B Double Bonds", E. Rivard, W. A. Merrill, J. C. Fettinger and P. P. Power. Chemical Communications, 2006, 3800-3802.

17. "Boron-Pnictogen Multiple Bonds: Donor-stabilized P=B and As=B Double Bonds and a Hindered Iminoborane with a B-N Triple Bond", E. Rivard, A. Merrill, J. C. Fettinger, R. Wolf, G. H. Spikes and P. P. Power. Inorganic Chemistry, 2007, 46, 2971-2978.

18. "Synthesis and Thermolytic Behavior of Tin(IV) Formates: In Search of Recyclable Metal-Hydride Systems", B. D. Ellis, T. M. Atkins, Y. Peng, A. D. Sutton, J. C. Gordon and P. P. Power. Dalton Transactions, in press.

VII. POSTERS AND PRESENTATIONS

1. "Promotion of Hydrogen Release from Ammonia Borane with nanostructured hexagonal boron nitride", D. Neiner, A. Karkamkar, J. C. Linehan, B. Arey, T. Autrey, and S. M. Kauzlarich, oral presentation at the 237th National ACS meeting Salt Lake City, Utah, March 22-26, 2009.

2. "Promotion of Hydrogen Release from Ammonia Borane with Mechanically Activated Hexagonal Boron Nitride", D. Neiner, A. Karkamkar, J. C. Linehan, B. Arey, T. Autrey, and S. M. Kauzlarich, oral presentation at the DOE Center of Excellence Meeting on Hydrogen Storage, November 8th, 2008, Denver, Colorado.

3. "Mechanically Activated Materials for Hydrogen Release from Ammonia Borane", D. Neiner , S.M. Kauzlarich A. Karkamkar, J. C. Linehan, B. Arey, T. Autrey, NEDO Workshop, San Diego, CA, September 9-11, 2008.

4. "Synthesis and Characterization of Silicon Framework Compounds for Hydrogen Storage", S. M. Kauzlarich, D. Neiner, N. L. Okamoto, C. L. Condron, Q. M. Ramasse, P. Yu, N. D. Browning presented at the Southeastern Regional American Chemical Society Meeting, October 24 – 27, 2007, in Greenville, SC.

5. "Characterization of Hydrogen Encapsulated in a Type-I Silicon Clathrate", D. Neiner, N. L. Okamoto, C. L. Condron, Q. M. Ramasse, P. Yu, N. D. Browning, and S. M. Kauzlarich, oral presentation at 234th ACS meeting, Boston, MA, USA, August 19-23, 2007.

6. "Characterization of Hydrogen Encapsulated in a Type-I Silicon Clathrate", D. Neiner, N. L. Okamoto, C. L. Condron, Q. M. Ramasse, P. Yu, N. D. Browning, and S. M. Kauzlarich, oral presentation at North American Solid State Chemistry Conference, Texas A&M University, May 17, 2007.

7. "Silicon nanoparticles: A new hydrogen storage material", D. Neiner and S. M. Kauzlarich" oral presentation at the 233rd ACS National Meeting, Energy Research in Inorganic Chemistry, Chicago, IL, March 25-29, 2007.

8. "Hydrogen in silicon clathrates" D. Neiner, C. L. Condron , S. M. Kauzlarich poster presentation at the International Symposium on Metal- Hydrogen System Fundamentals and Applications, October 1-6th, 2006, Lahaina, Maui, Hawaii.

9. "Nanocrystalline silicon for hydrogen storage" D. Neiner, C. Chervin, H. W. Chiu, M. Blessent, S. M. Kauzlarich, poster presentation at the International Symposium on Metal- Hydrogen System Fundamentals and Applications, October 1-6th, 2006, Lahaina, Maui, Hawaii.

10. "Synthesis and functionalization of luminescent silicon nanoparticles for biological applications" X. Zhang, D. Neiner, S. Wang, A. Y. Louie, S. M. Kauzlarich, poster presentation at The 232nd ACS National Meeting, San Francisco, CA, September 10-14, 2006.

.

11. "Type I silicon clathrates: Synthesis and NMR characterization" D. Neiner, C. L. Condron , S. M. Kauzlarich, poster presentation at The 232nd ACS National Meeting, San Francisco, CA, September 10-14, 2006.

12. "Exploration of discrete and nanocrystalline aggregates of elemental silicon using solid state Zintl precursors", A. M. Goforth, A. Courtis, X. Zhang, D. Neiner, S. M. Kauzlarich, poster presentation at The 232nd ACS National Meeting, San Francisco, CA, September 10-14, 2006.

13. "Investigation of nanocrystalline silicon as a possible hydrogen storage material", D. Neiner, H. W. Chiu, M. Blessent, S. M. Kauzlarich, poster presentation at The 232nd ACS National Meeting, San Francisco, CA, September 10-14, 2006.

14. "Nanocrystalline silicon for hydrogen storage", D. Neiner and S. M. Kauzlarich, Poster presentation at International Symposium on materials Issues on Hydrogen Production and Storage, August 20-25th, 2006, Santa Barbara, CA, USA.

15. "Nanocrystalline silicon for hydrogen storage" D. Neiner, C. Chervin, H. W. Chiu, M. Blessent, S. M. Kauzlarich, poster presentation at the Materials Research Society Meeting, April 17-21st, 2006, Moscone West, San Francisco, CA, USA.

16. "Chemical Hydrogen Storage using Ultra-High Surface Area Main Group Elements", D. Neiner, A. Pickering, M. Blessent, S. Kauzlarich and P. Power, Oral Presentation for the DOE Meeting on Hydrogen Storage, October 26th, 2005, Salt Lake City, Utah.